Cosmic Ray Propagation in Turbulent Magnetic Fields

Kenji Shibamura

Supervisors: Dr. Raymond Protheroe, Prof. Roger Clay

Thesis submitted for the degree of

Master of Science

in

The University of Adelaide

(Faculty of Science)

November 30, 2005

This thesis contains no material which has been accepted for the award of any other degree or diploma in any university and that, to the best of the my knowledge and belief, the thesis contains no material previously published or written by another person, except where due reference is made in the text of the thesis.

The author contents to the thesis being made available for photocopying and loan if accepted for the award of the degree.

signed:

Kenji Shibamura

Acknowledgements

I would like to thank my supervisors Raymond Protheroe and Roger Clay for their enormous amount of guidance and support. I would like to thank Bruce Dawson and Greg Thornton for useful advice about my computer skills, presentation skills and my research.

I would like to thank my office mates, Sarah Clay and Donna Riordan for their friendship and kind advice. I would like to thank David Swaby for his friendship and kind advice. I would like to thank all of astrophysics group members for their support and advice. I would also like to thank Ron Sidel, Lee Jurgs and Peter McMillan for useful advice to improve my English skills, such as writing and speaking. I would also like to thank my friends, Ian Marks, Reiko Shibata and Ikuko Iwasaki for their friendship and encouragement. Without their kind advice and support during my candidature, I would never be able to complete my Master Program in Australia.

Finally I would like to thank my parents and my brother and sister for their enormous amount of support including financial support and encouragement.

Abstract

How a high energy cosmic ray behaves in space is one of the major issues in astrophysics. Cosmic ray propagation in the astronomical environment can be explained as a diffusion phenomenon. My research used the Monte Carlo technique to calculate diffusion tensors and analysed the energy dependence of the diffusion tensor on the cosmic ray energy and magnetic field turbulence.

Turbulent magnetic fields exist in an astronomical environment. The power spectrum of the turbulence is proportional to $k^{-5/3}$, where k is the wavenumber. This turbulence is called the Kolmogorov-like magnetic field.

To understand cosmic ray propagation in the astronomical environment, it is useful to study cosmic ray diffusion in turbulent magnetic fields. Monte Carlo simulation is the most suitable technique for the study of the cosmic ray diffusion in turbulent magnetic fields. The aim of my research is to determine the diffusion tensors by using the Monte Carlo simulation and to study how the magnetic field turbulence scale affects the cosmic ray diffusion. My research is applied to simulation of an actual astronomical phenomena, known as shock acceleration.

Chapter 1 provides a brief introduction of high energy cosmic rays and Kolmogorov-like magnetic field. Chapter 2 introduces three different simulation methods for cosmic ray diffusion.

Chapter 3 describes the simulation technique by Honda [11]. He sampled vector potentials to produce Kolmogorov-like turbulent magnetic fields.

Chapter 4 describes the simulation technique by Giacalone and Jokipii [7] [8] [9]. They used a superposition of isotropic plane waves to produce Kolmogorov-like magnetic field.

Chapter 5 discusses the application of a cosmic ray diffusion simulation method to

cosmic ray shock acceleration. In this chapter, the simulation method by Giacalone and Jokipii was selected to investigate cosmic ray shock acceleration.

Chapter 6 presents a summary of whole work in my research and future work to extend this study.

Contents

Chapter 1

Introduction

1.1 Cosmic rays

Cosmic rays are atomic and subatomic particles from astronomical sources travelling in space at nearly the speed of light. It is known that the low energy cosmic rays consist mostly of protons. Cosmic rays are divided into two kinds, primary and secondary cosmic rays. As the primary cosmic rays encounter the Earth's atmosphere, they collide with molecules in the atmosphere. These collisions produce secondary cosmic rays. Figure 1.1 illustrates the energy spectrum of cosmic rays, and indicates the energy of cosmic ray reaches to the earth [4]. The energy spectrum of cosmic rays can be characterized by a power law, namely $\text{Flux}(E) \propto E^{\alpha}$. In Figure 1.1, the power law of the energy spectrum changes at around 3×10^{15}eV and again at around 3×10^{18}eV. These points are called "knee" and "ankle" respectively. Any kind of theory about cosmic ray origin and acceleration must explain this "knee" and "ankle". This implies that there may be different origins and acceleration mechanisms of cosmic rays in space. The study of cosmic ray propagation in space helps us to understand the origin and acceleration mechanism of cosmic rays.

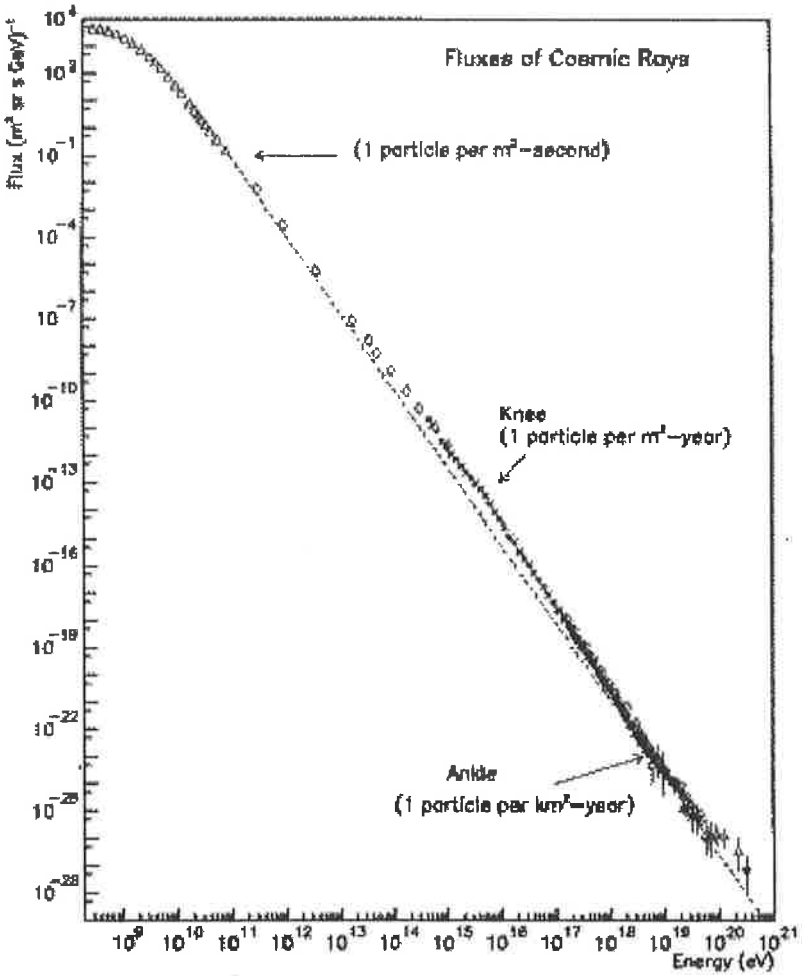

Figure 1.1: Energy spectrum of cosmic rays. The slope change of the spectrum at around 3×10^{15}eV is called "knee". The slope change of the spectrum at around 3×10^{18}eV is called "ankle". [4]

1.2 Observing magnetic field in space

To study cosmic ray propagation, it is necessary to know the environment of space. The magnetic fields in space have significant influence upon cosmic ray propagation. Precise information about the magnetic fields in space is very important for understanding propagation of cosmic rays. There are several techniques to determine the magnetic fields. Faraday Rotation and Zeeman Splitting are the frequently among the techniques used. The following sections introduce these two techniques commonly used to determine the magnetic fields in space.

1.2.1 Faraday Rotation

Magnetic fields pervade the ionised interstellar or inter-cluster gases. The angle of the plane of linearly polarised radio wave emission is rotated as the emission passes through a region containing free electrons and magnetic field. This phenomenon is called Faraday Rotation. Faraday Rotation provides us information about cosmic magnetic fields.

The rotation angle of linearly polarised emission is given by

$$\theta = 8.12 \times 10^3 \lambda^2 \int_0^l n_e B_{\parallel} dl \qquad \text{(radians)} \tag{1.2.1}$$

where $B_{\parallel}$ (tesla) is the magnetic field component parallel to the line of propagation, n_e (particles/m^3) is the number density of free electrons, and the quantity θ/λ^2 is called Rotation Measure and denoted as RM.

When $RM > 0$, the field lines are towards the observer, whereas $RM < 0$, the field lines are away from the observer. The strength of magnetic field can be estimated from following relation,

$$\langle B_{\parallel} \rangle \propto \frac{RM}{DM} \propto \frac{\int_0^l n_e B_{\parallel} dl}{\int_0^l n_e dl} \tag{1.2.2}$$

where DM is called Dispersion Measure and is obtained from the delay time of the arrival of radio signals, due to propagation through the interstellar medium, as a function of frequency. The dispersion Measure and rotation measure have been obtained from pulsar observation.

1.2.2 Zeeman Splitting

The Zeeman effect is the splitting of the spectral lines when an atom exists in an external magnetic field. The Zeeman effect is widely used for determining the magnetic fields in astronomical objects. However, the magnetic field strengths need to be large enough to actually observe line splitting, otherwise the line splitting appears as line broadening. The strengths of weak magnetic fields can be deduced by measuring two circular polarisation components from Zeeman splitting if the magnetic field lines are parallel to the line of sight.

1.3 Kolmogorov spectrum turbulent magnetic field

The Kolmogorov [15] [16] [17] turbulence model has been well accepted in fluid mechanics since 1941. The model states that turbulent energy injected into large eddies in turbulent fluid transfer or cascade to smaller eddies. The energy spectrum of turbulence $S(k)$ follows power low namely,

$$S(k) \propto k^{-\alpha}, \tag{1.3.1}$$

where k is wavenumber and defined as $\frac{2\pi}{\lambda}$ (λ: wavelength) or $\frac{2\pi}{L}$ (L: eddy size). In the Kolmogorov model, energy spectrum is proportional to $k^{-5/3}$. This is called the Kolmogorov 5/3 power law. For three-dimensional wavenumber space, α is 11/3. Magnetic fields in space have Kolmogorov-like turbulence character. The following sections describe

magnetic fields in space and also present the evidence that magnetic fields in space are Kolmogorov-type turbulence.

Following Equation 1.3.1, observational data in Section 1.3.1 to 1.3.3 show that energy spectrum $|B^2(k)|$ is proportional to $k^{-5/3}$, and $|B^2(\vec{k})|$ is proportional to $k^{-11/3}$ for a three-dimensional k-space.

1.3.1 Magnetic fields from solar wind

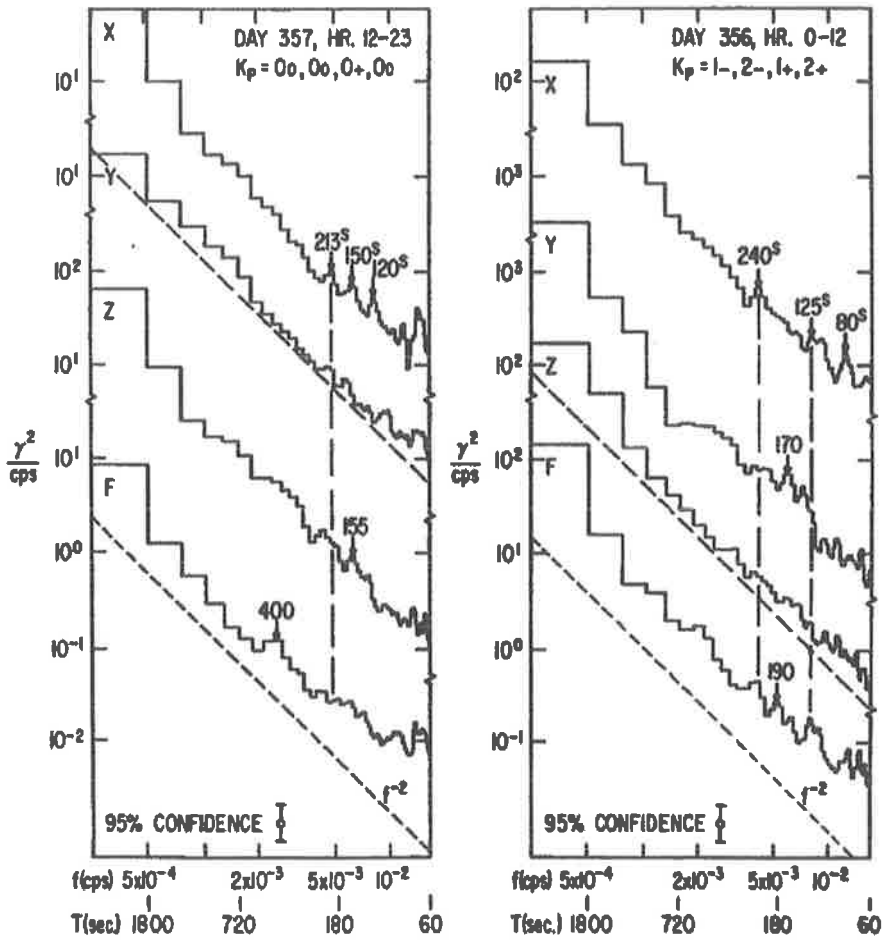

Figure 1.2: The x-, y- and z-component and magnitude F of the power spectrum of magnetic field energy density per unit frequency, $B^2(f)/f$. The data came from Pioneer 6 spacecraft and obtained from December 1965 to March 1966. $1\gamma = 10^{-5}$G. Dashed lines represent the power law index $\alpha = 2$. [22]

The sun is the most studied stellar object in space. It is known that magnetic fields exist in our solar system. The flow of plasma from the sun's corona is called the solar

wind and the solar wind creates magnetic fields in the solar system. The solar wind magnetic field strength is about 5×10^{-9}T or 50μG. Sari and Ness [22] studied the Pioneer 6 interplanetary magnetic field data and the calculated power spectra of magnetic fields. The data was collected from December 1965 to March 1966. Figure 1.2 shows x-, y- and z-component of power spectra of interplanetary magnetic field energy density per unit frequency. The dashed lines in Figure 1.2 represent the power law f^{-2} lines. The spectra are not as steep as f^{-2} lines, perhaps closer to the power law of $f^{-5/3}$.

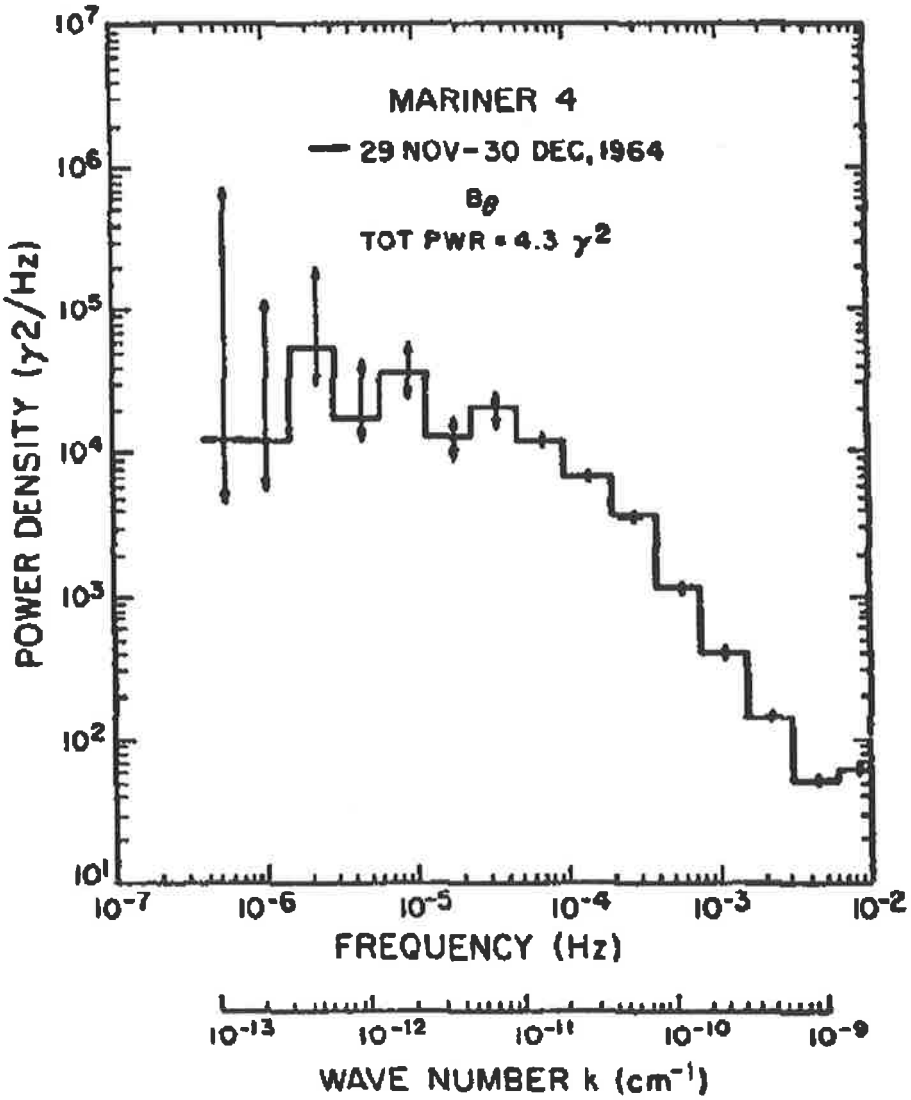

Figure 1.3: The power spectrum of magnetic field energy density, $B^2(\omega)$. The data came from Mariner 4 magnetometer data obtained from 29 November to 30 December 1964. [13]

Jokipii [13] presented observational data of solar wind magnetic fields obtained from

magnetometers of spacecraft Mariner 4. Figure 1.3 is power spectrum of the magnetic field from Mariner 4 magnetometer data obtained from 29 November to 30 December, 1964. Jokipii noted that the index α of power-law spectrum $k^{-\alpha}$ (k:wavenumber) had the range $1.5 < \alpha < 2.0$.

Goldstein et al. [10] presented in their review paper that the power spectrum of magnetic field fluctuations from Mariner 10 magnetometer data collected on March 10, 1974, and this also showed the spectral slope is close to $-5/3$.

These results suggest that the magnetic fields in the solar system follow a Kolmogorov power law.

1.3.2 Interstellar magnetic field

Interstellar matter consists of about 99% gas and 1% fine dust grains. About 70% of the gas is hydrogen, 28% is helium and 2% is heavier elements. Ionised interstellar gas creates magnetic fields in the galaxy, and the strength of the galactic magnetic field is estimated from 10^{-10}T to 10^{-9}T. Lee and Jokipii [18] analyzed data on interstellar scintillation of 3 pulsars (CP 0323, PSR 0833-45 and NP 0532) and concluded that interstellar magnetic fields follow a Kolmogorov power law. Furthermore, Armstrong and Rickett [1] used interstellar scintillation to observe 17 pulsars and study interstellar electron density. Figure 1.4 shows the electron density spectra of two pulsars (PSR 0329+54 and PSR 1642-03) among 17 pulsars for two different centre frequencies ((a) 408MHz and (b) 340MHz). The spectra are consistent with the solid lines, which are 11/3 power law lines appropriate to three-dimensional k-space. Armstrong and his colleagues [2] used the interstellar scintillation technique to observe the interstellar electron density at distances less than 1kpc. They concluded that the spectrum of electron density follows a Kolmogorov law. This provides

evidence supporting that interstellar magnetic fields are also Kolmogorov-like magnetic fields.

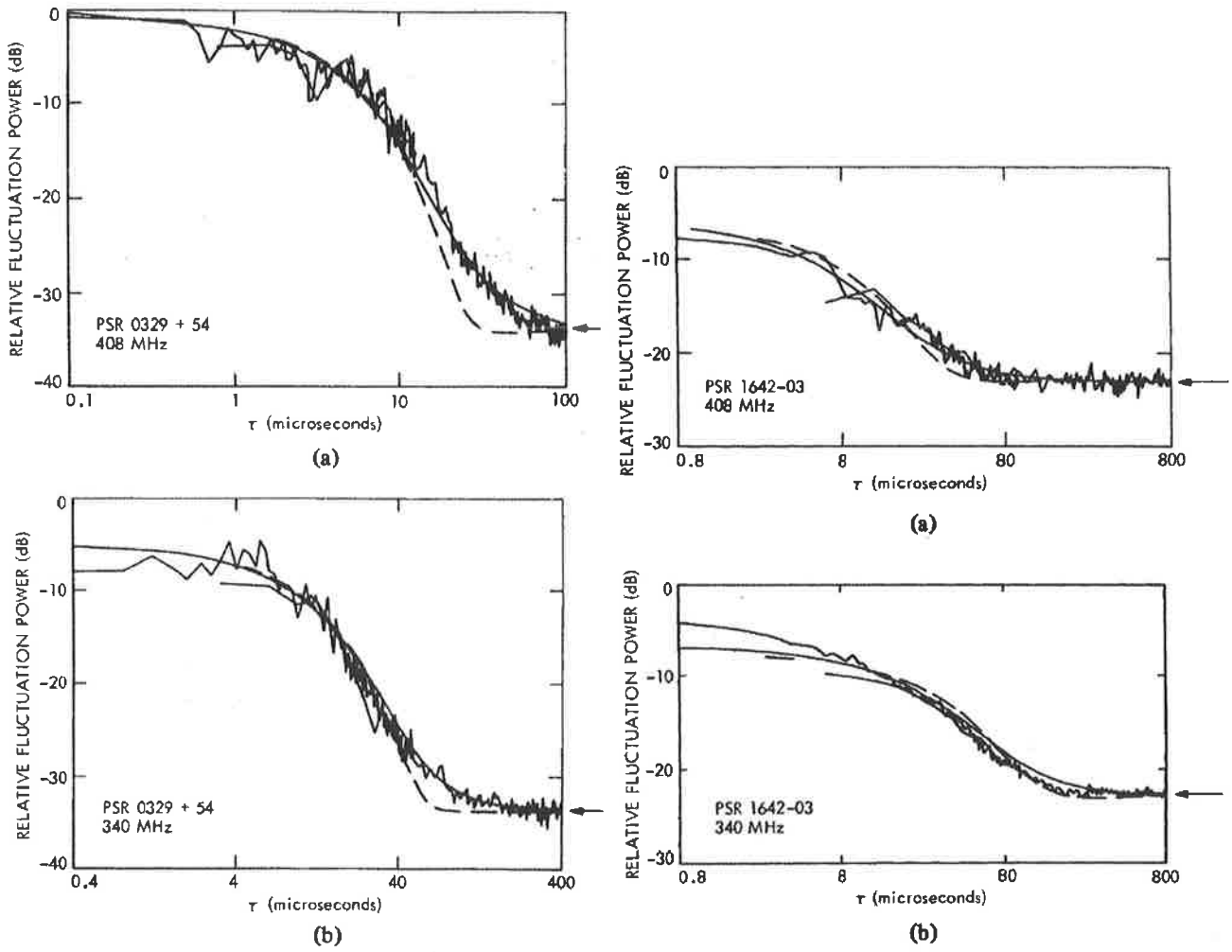

Figure 1.4: Fluctuation power spectra of electron density from interstellar scintillation data. (LEFT) Spectra of PSR 0329+54. (a) Centre frequency is 408MHz. (b) Centre frequency is 340MHz. (RIGHT) Spectra of PSR 1642-03. (a) Centre frequency is 408MHz. (b) Centre frequency is 340MHz. The solid line indicates $\alpha = \frac{11}{3} = 3.6$ power law appropriate to three-dimensional k-space. [1]

1.3.3 Inter-cluster magnetic field

Intergalactic magnetic fields have been studied by observing diffuse radio and X-ray emission coming from clusters of galaxies. Schlickeiser et al. [23] observed the diffuse halo from

the Coma cluster at a wavelength $\lambda = 11$ cm. Together from these two observations of the diffuse radio and hard X-ray emission from the Coma cluster of galaxies, the average strength of the magnetic field of intergalactic matter has been found to be between 4×10^{-12}T and 12×10^{-10}T.

Vogt and Ensslin [25] measured Faraday Rotation of 3 clusters (Abell 400, Abell 2634, Hydra A) and plotted the power spectrum of magnetic field shown in Figure 1.5. The spectral indices α of the power-law spectrum $k^{-\alpha}$ lie in the range from 1.6 to 2.0. The Kolmogorov spectrum index is $5/3 \approx 1.67$, so the Kolmogorov spectrum slope is within this range. Therefore, magnetic fields outside of the Galaxy may also have a Kolmogorov turbulence character.

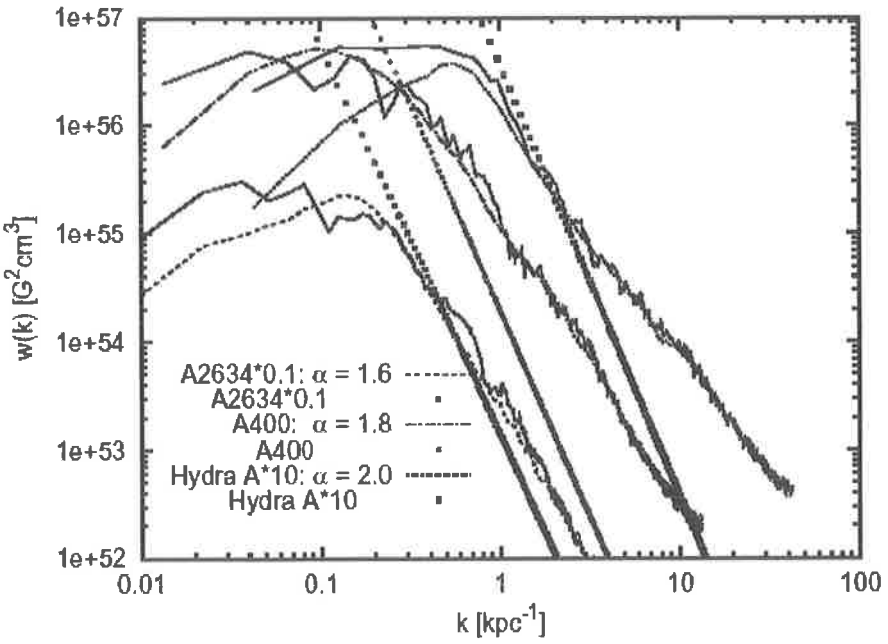

Figure 1.5: The power spectra of magnetic fields $w(k)$ of three clusters (Abell 2634, Abell 400 and Hydra A). The solid curves are calculated from p-spaced response functions, where p is scale of magnetic irregularity. [25]

It can be concluded that the magnetic fields in space are probably Kolmogorov-type turbulent magnetic fields.

1.4 Cosmic ray diffusion in turbulent magnetic fields

How cosmic rays behave in the space is one of the big issues in astrophysics. Cosmic rays created by astronomical sources interact with the interstellar or inter-cluster medium while traveling in space. It is already known that magnetic fields exist in space, and that charged cosmic rays diffuse in those magnetic fields. Equation 1.4.1 is the well established diffusion equation in three-dimensions, and describes how the cosmic ray diffuse in turbulent magnetic fields.

$$\frac{\partial n(\vec{r},t)}{\partial t} - K\nabla^2 n(\vec{r},t) = Q(\vec{r},t). \tag{1.4.1}$$

In Equation 1.4.1, n represents the number density of particles. The second term of the equation is expressed as the flux caused by diffusion and K represents the diffusion coefficient which dominates diffusion of the particles. The right hand side of the equation $Q(\vec{r},t)$ is source term.

When N_0 particles are injected at $(x,y,z) = (0,0,0)$ and at $t = 0$ (initial condition), and are free to diffuse in an infinite medium (boundary condition). The solution of the diffusion equation is

$$n(\vec{r},t) = \frac{1}{\sqrt{(4Kt)^3}} \exp\left(-\frac{r^2}{4Kt}\right). \tag{1.4.2}$$

If cosmic ray diffusion is occurs in a medium moving at velocity $\vec{v}$, such as in the solar wind, the diffusion equation can be expressed as this,

$$\frac{\partial n(\vec{r},t)}{\partial t} + \vec{v}\cdot\vec{\nabla} n(\vec{r},t) - K\nabla^2 n(\vec{r},t) = Q(\vec{r},t). \tag{1.4.3}$$

In the case of anisotropic diffusion the diffusion equation becomes

$$\frac{\partial n(\vec{r},t)}{\partial t} - \sum_{i=1}^{3}\sum_{j=1}^{3} \frac{\partial}{\partial x_i} K_{ij} \frac{\partial}{\partial x_j} n(\vec{r},t) = Q(\vec{r},t) \tag{1.4.4}$$

where K_{ij} is the diffusion tensor.

Jokipii [12] proposed that the diffusion tensor for the regular component of B_0 in the z-direction, is

$$K_{ij} = \begin{pmatrix} K_{xx} & K_{xy} & K_{xz} \\ K_{yx} & K_{yy} & K_{yz} \\ K_{zx} & K_{zy} & K_{zz} \end{pmatrix} = \begin{pmatrix} K_\perp & -K_\top & 0 \\ K_\top & K_\perp & 0 \\ 0 & 0 & K_\parallel \end{pmatrix}.$$

where $K_\perp$ is tensor component perpendicular to regular magnetic field. $K_\parallel$ is tensor component parallel to regular magnetic field. $K_\top$ is the component which causes a net flux in the x-direction if there is a gradient in the y-direction, or vice versa. The diffusion tensor is calculated from following relations.

$$\langle z^2 \rangle = 2K_\parallel t, \tag{1.4.5}$$

$$\langle x^2 + y^2 \rangle = 4K_\perp t, \tag{1.4.6}$$

These equations come from the solution for diffusion equation 1.4.2.

Cosmic ray diffusion in turbulent magnetic fields depends on the scale of irregularity in the magnetic fields compared to the gyroradius as well as the momentum and charge. If the gyroradius is much smaller than the irregularity, the particle will follow the magnetic field line and will not be scattered by the magnetic field. If the gyroradius is much larger than irregularity, the magnetic field does not affect particle motion much, so little diffusion results. However, if the gyroradius is close to irregularity, the particle will be scattered by the magnetic field. Therefore, determining the effective range of the irregularities is an important issue in cosmic ray diffusion. The next section will discuss numerical simulations of cosmic ray diffusion

Chapter 2

Cosmic ray diffusion simulation

This chapter discusses the numerical simulation of cosmic ray diffusion. Section 2.1 discusses the limitations of numerical simulation. Section 2.2 discusses three different methods of simulation of cosmic ray diffusion using the Monte Carlo method, which have been used previously.

2.1 Numerical error and computational time

Numerical simulations are often used in astrophysics to model astrophysical phenomena, or to check observational data. However, in implementing a numerical simulation, it is important to consider the limitations of numerical method.

While computers are now a universal computational tool with a wide range of applications, there are several factors that need to be considered when used in situations involving extensive and complex calculations of the type used in this research. The main two factors to be considered are numerical error and computational efficiency.

2.1.1 Numerical error

Generally speaking, there are two kinds of essential errors in numerical calculation; Truncation Error and Round-Off Error.

1. Truncation Error:

   The truncation error may occur when an iterative method is implemented in the computer. The concept of infinity is common in mathematics but cannot be implemented in a computer. Consider, for example, the Fourier Transform given by

   $$f(k) = \int_{-\infty}^{\infty} F(x) \exp(-i2\pi kx) dx. \tag{2.1.1}$$

   However the Fourier transform is more often evaluated using the discrete Fourier transform, namely

   $$f_k = \frac{1}{N} \sum_{x=0}^{N-1} F_x \exp\left(\frac{-i2\pi kx}{N}\right). \tag{2.1.2}$$

   The Fourier transform, Equation 2.1.1 involves integration from $-\infty$ to $+\infty$ but a computer can only evaluate the function between two finite limits and therefore any result must be less accurate. In addition, a computer uses discrete mathematics and the above function must be implemented by the summation over a number of finite rather than an infinite number of intervals. As a result the evaluation of the Fourier transform in Equation 2.1.1 by using that of Equation 2.1.2 is improved by having very large limits of integration function and having a very large number of intervals.

2. Round-Off Error:

   Numbers, other than integer, presented by any computing devices have some imprecision. Computers usually use floating-point numbers of fixed storage length, so they can not precisely represent any irrational numbers and some rational numbers. This error is called round-off error.

3. Statistical errors associated with Monte Carlo methods:

   Statistical errors associated with Monte Carlo methods should be taken into account. Occurrence of statistical errors is inevitable in Monte Carlo simulation because an infinite number of samples can not be obtained in the simulation. This type of error can be reduced by increasing the number of the samples.

2.1.2 Computational Efficiency

Computational efficiency is also a main issue in numerical simulation. Computational time depends on the number of equations in the algorithm and the nature of the statements and the implementation of in-built functions. Computational efficiency sometimes conflicts with precision of numbers. For example, if double precision is used rather than single precision, then a more accurate calculations result. However using double precision is more time consuming than using single precision and so the time taken for the simulation increases. In order to avoid numerical errors and excessive simulation times, the simulation should

1. use as simple a routine as possible.

2. reduce the number of time consuming calculations.

The study will attempt to simplify algorithms to reduce computational time. If the simpler algorithm gives results as accurate as for a more complicated algorithm, then the study will adopt the simpler algorithm in the simulation.

2.2 Three cosmic ray diffusion simulations

Cosmic ray diffusion in turbulent magnetic fields have been studied both analytically and numerically. Among the studies of cosmic ray diffusion, three different diffusion simulations have been selected for investigation into cosmic ray propagation in space.

1. The simulation proposed by Honda (1987, [11]).

2. The simulation proposed by Giacalone and Jokipii (1999 [9]).

3. The simulation proposed by Casse, Lemoine and Pelletier (2001, [5]).

These researchers applied a Monte Carlo method to the calculation of the diffusion tensor. Monte Carlo simulation is a useful stochastic method, which randomly generates values for uncertain variables many times to estimate the behaviour of the model.

Figure 2.1 indicates the flow chart of the cosmic ray diffusion simulations. In general, the cosmic ray diffusion simulations follow this flow chart. The three simulations are similar to each other except for the procedure of creating magnetic fields.

1. The first step is creating turbulent magnetic fields. The observational data indicate that magnetic fields in space are Kolmogorov-type magnetic fields. So the turbulent magnetic fields used in the diffusion simulation should show a Kolmogorov spectrum.

2. The next step is the injection of relativistic charged particles into the magnetic fields. The typical relativistic cosmic ray is proton. The number of particles injected should be sufficiently large to obtain a reliable statistical outcome. The initial velocity vector of the cosmic ray should be isotropic.

3. The third step is to calculate the positions of the particles at various times. A small number of cosmic ray trajectories are plotted for checking purposes, e.g. the size

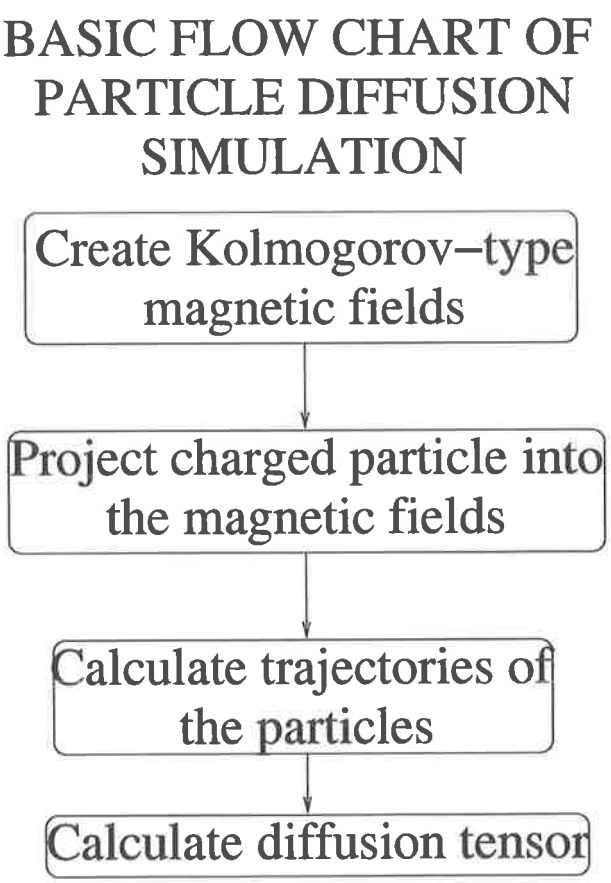

Figure 2.1: Basic flow chart of simulation of cosmic ray diffusion in turbulent magnetic field. The diffusion simulation can be divided into 4 steps.

of time step used in the simulation which is a compromise between accuracy and simulation time.

4. The last step is to calculate the diffusion tensor by using Equations 1.4.5 and 1.4.6.

In the three simulations, the total magnetic field consists of a regular part and an irregular part. The regular magnetic field lines are straight lines directed toward one direction, for example the z-direction. The irregular magnetic fields has isotropy and are generated using the Monte Carlo method, namely

$$\vec{B}_{total} = B_0\hat{e}_z + \delta\vec{B}. \tag{2.2.1}$$

The three simulations do not consider electric fields because the interstellar plasma has high conductivity, and so static electric fields hardly exist in space. The simulations assumed that the turbulent magnetic fields are static. Therefore, cosmic rays change its direction but do not change energy.

Using a mesh or grid space to simulate turbulent phenomena is common in fluid dynamics. The simulations by Honda [11] and Casse et al. [5] used a grid space to express the turbulent magnetic fields, whereas Giacalone and Jokipii [9] used a different way to create the turbulent magnetic fields. Section 2.2.1 to 2.2.3 will review the three different simulations of cosmic ray diffusion.

2.2.1 Simulation by Honda (1987)

Honda [11] simulated cosmic ray propagation in the turbulent galactic magnetic fields, and calculated diffusion tensors. The cosmic rays he simulated were relativistic particles, so the energy range was 10^{16}eV$< E < 10^{18}$eV. The corresponding gyroradius for a 3×10^{-10}T magnetic field is from 3 to 300pc. Honda assumed that the total magnetic fields $\vec{B}_{total}$ in

a galaxy consists of two parts, a regular part $\vec{B}_0$ and an irregular part $\delta\vec{B}$, such that

$$\vec{B}_{total} = \vec{B}_0 + \delta\vec{B}. \tag{2.2.2}$$

The direction of the regular magnetic field B_0 was the z-direction and the irregular magnetic field δB was isotropic. He assumed that the regular magnetic field strength was about 3×10^{-10}T$(= 3\mu$G) and the irregular magnetic field strength was about 1.5×10^{-10}T$(= 1.5\mu$G). Since he assumed the magnetic fields in his simulation to be static, there was no effect of convection and Fermi type of acceleration. He also neglected any electric fields.

In order to duplicate the galactic magnetic field, Honda developed three-dimensional lattices. Magnetic fields on each grid point were calculated by using vector potentials. Honda calculated random vector potentials from Monte Carlo simulations, and these potentials obeyed an exponential distribution. The vector potential was sampled at each grid points of the lattice. Calculating the curl of vector potential,

$$\delta\vec{B} = \vec{\nabla} \times \delta\vec{A} \tag{2.2.3}$$

produced the magnetic fields at each grid point.

Honda made several lattices with a different grid spacings to create a Kolmogorov-type turbulent magnetic field. The magnetic field placed on each grid point had a magnitude dependent upon the grid spacing. Honda proposed the magnetic fields for different grid spacing with the lattice constant L_i, was

$$L_i = 10^{-i/2} L_0, \qquad (i = 1, 2, 3, \cdots) \tag{2.2.4}$$

where L_0 is the largest scale of irregularities and corresponds to the maximum grid spacc length. After the contributions to the magnetic fields, magnitudes corresponding to different grid scales are placed on the grid points, the magnetic fields at the grid points are vectorially added to create the irregular part of the magnetic field. For a Kolmogorov

spectrum, the weight of the field energy density of the superimposed magnetic fields is proportional to $L_i^{5/3}$.

Honda injected a number of charged particles into the lattice. The charged particles were propagated in the magnetic fields according to the equation of motion for charged particle in the magnetic fields.

$$\frac{d\vec{p}}{dt} = q(\vec{v} \times \vec{B}) \tag{2.2.5}$$

Each component of momentum $\vec{p}$ after a time increment $\triangle t$ is

$$p'_{\perp} = p_{\perp} \cos(\omega \triangle t) - p_{\top} \sin(\omega \triangle t), \tag{2.2.6}$$

$$p'_{\top} = p_{\perp} \sin(\omega \triangle t) + p_{\top} \cos(\omega \triangle t), \tag{2.2.7}$$

$$p'_{\parallel} = p_{\parallel}, \tag{2.2.8}$$

where $p_{\perp}$ and $p_{\parallel}$ are components perpendicular and parallel to the mean magnetic field $\vec{B}_{total}$, respectively. The component $p_{\top}$ is perpendicular to both $p_{\perp}$ and $p_{\parallel}$. ω is the gyrofrequency and is defined as

$$\omega = \frac{eB}{E} = \frac{c}{R_g} \text{ (Hz rad)} \tag{2.2.9}$$

where e (coulomb) and E (eV) are the charge and the energy of the cosmic ray, respectively. R_g (m) is the gyroradius. Since the computer needed to be operated efficiently and avoid numerical errors, Honda had to choose an appropriate time increment for the simulation, a compromise between computational time and error. He found $\triangle t = \frac{1}{10\omega} = \frac{R_g}{10c}$ was best as the time increment. Positions of the particle for each time can be obtained from Equation 2.2.5.

Since Honda supposed that the regular magnetic fields lines are parallel to the z-

direction, the elements of the diffusion tensor become,

$$K_{ij} = \begin{pmatrix} K_{xx} & K_{xy} & K_{xz} \\ K_{yx} & K_{yy} & K_{yz} \\ K_{zx} & K_{zy} & K_{zz} \end{pmatrix} = \begin{pmatrix} K_{\perp} & -K_{\top} & 0 \\ K_{\top} & K_{\perp} & 0 \\ 0 & 0 & K_{\parallel} \end{pmatrix}.$$

$K_{\parallel}$ is a diffusion tensor component parallel to $\vec{B}_0$, $K_{\perp}$ is perpendicular to $\vec{B}_0$. $K_{\top}$ is the component which causes a net flux in the x-direction if there is a gradient in the y-direction, or vice versa. In order to calculate the diffusion tensor K_{ij}, he carried out a number of simulations and took averages of distances for each time, $t_1 = \triangle t$, $t_2 = 2 \triangle t$, and so on. After calculating the average distance for each time increment, the plots of squared average distance versus time could be created by using the following relations,

$$\begin{aligned} \langle x^2 + y^2 \rangle &= 4K_{\perp}t, \\ \langle z^2 \rangle &= 2K_{\parallel}t. \end{aligned} \tag{2.2.10}$$

Each component of the diffusion tensor will be the slope in the average squared distance versus time plot is illustrated in Figure 2.2.

Honda calculated the diffusion tensor perpendicular to z-direction $K_{\perp}$ and parallel to z-direction $K_{\parallel}$ for different energies ranging from 10^{16}eV to 10^{18}eV. Figure 2.3 shows diffusion tensors K/cL_0 versus gyroradius R_g/L_0 (L_0: turbulence scale) for various values of the ratio,

$$\frac{\langle \delta B \rangle}{B_0} = \frac{2^n}{4}, \qquad (n = 0, 1, 2, 3). \tag{2.2.11}$$

The ratio $\frac{\langle \delta B \rangle}{B_0}$ expresses the degree of turbulence. If $\frac{\langle \delta B \rangle}{B_0} \ll 1$, the regular magnetic field dominates the total magnetic field and the magnetic fluctuations are very small. On the other hand if $\frac{\langle \delta B \rangle}{B_0} \gg 1$, the irregular magnetic field dominates the total magnetic field and the magnetic fields become more isotropic. Figure 2.3 (LEFT) shows the parallel diffusion tensor $K_{\parallel}/cL_0$ versus gyroradius R_g/L_0 and (RIGHT) shows the perpendicular

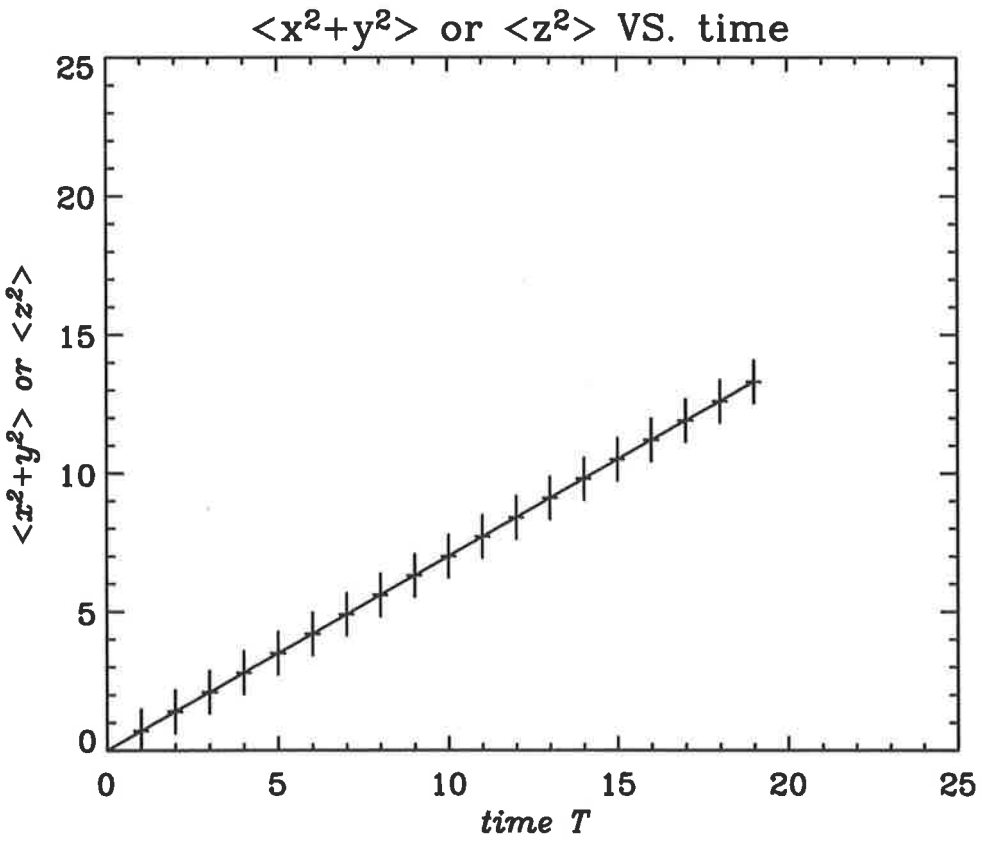

Figure 2.2: Schematic diagram of squared average distance $\langle x^2 + y^2 \rangle$ or $\langle z^2 \rangle$ vs. time T. The slope of line becomes diffusion tensor component.

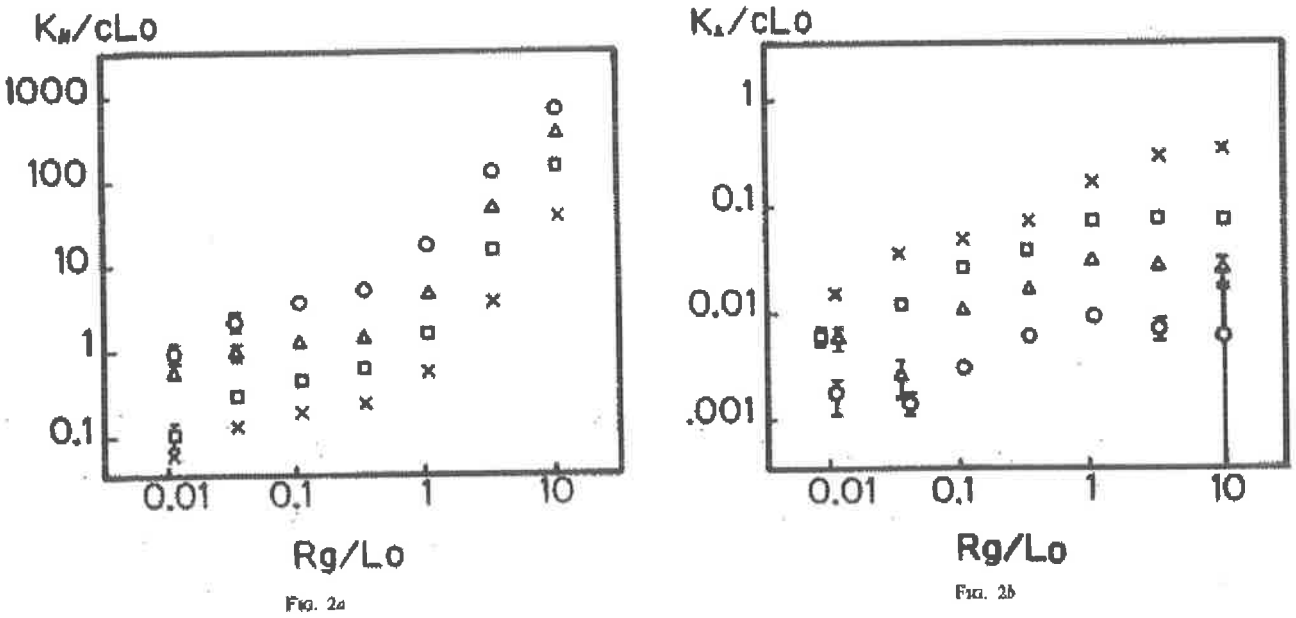

Figure 2.3: Diffusion tensors $\frac{K_\parallel}{cL_0}$ and $\frac{K_\perp}{cL_0}$ vs. gyroradius $\frac{R_g}{L_0}$ for various values of $\frac{\langle \delta B \rangle}{B_0}$. (LEFT) $\frac{K_\parallel}{cL_0}$ vs. $\frac{R_g}{L_0}$. (RIGHT) $\frac{K_\perp}{cL_0}$ vs. $\frac{R_g}{L_0}$. "o" for $\frac{\langle \delta B \rangle}{B_0} = \frac{1}{4}$, "△" for $\frac{\langle \delta B \rangle}{B_0} = \frac{1}{2}$, "□" for $\frac{\langle \delta B \rangle}{B_0} = 1$ and "×" for $\frac{\langle \delta B \rangle}{B_0} = 2$. [11]

diffusion tensor $K_\perp/cL_0$ versus gyroradius R_g/L_0 obtained by Honda. Honda noted that the behavior of the diffusion tensors changed suddenly at $\frac{R_g}{L_0} = 1$. This implies that this feature of the diffusion tensors is dependent on the ratio $\frac{R_g}{L_0}$ and two regime, which are $(\frac{R_g}{L_0} < 1)$ regime and $(\frac{R_g}{L_0} > 1)$ regime, exist. Honda introduced the fitting function for the perpendicular and parallel diffusion tensors.

$$\left(\frac{K_i}{cL_0}\right) = \left(\frac{K_i}{cL_0}\right)\left(\frac{R_g}{L_0}\right)^{\alpha}\left(\frac{\langle \delta B \rangle}{B_0}\right)^{\beta}, \tag{2.2.12}$$

where i represents $\parallel$ and $\perp$. He pointed out that the value of the index α in Equation 2.2.12 is different for the $(\frac{R_g}{L_0} < 1)$ regime and the $(\frac{R_g}{L_0} > 1)$ regime.

2.2.2 Simulation by Giacalone and Jokipii (1999)

Giacalone and Jokipii [9] simulated the collisionless scattering motion of cosmic rays in turbulent magnetic fields. The procedures are also explained in their earlier papers [7] and [8]. This section summarizes how they implemented this simulation.

Cosmic rays which Giacalone and Jokipii were interested in had an energy range from 10^6eV to 10^9eV and the range of the corresponding gyroradii for $B_0 = 5$nT was $4.46 \times 10^{-6}\text{AU} < r_g < 4.46 \times 10^{-3}\text{AU}$. The turbulent magnetic fields were interplanetary magnetic fields produced by the sun. The total magnetic field B_{total} consisted of a mean magnetic field B_0 and irregular magnetic field δB. The mean magnetic field B_0 was parallel to the z-direction and has the magnitude of 5.0nT. Giacalone and Jokipii proposed that the irregular part $\delta\vec{B}(x, y, z)$ be a superposition of isotropic plane waves with random polarisations and phases. They defined the irregular part $\delta\vec{B}(x, y, z)$ of the total magnetic field as

$$\delta\vec{B}(x, y, z) = \sum_{n=1}^{N_m} A(k_n)(\cos\alpha_n \hat{e}'_{xn} + i \sin\alpha_n \hat{e}'_{yn}) \exp(ik_n z'_n + i\beta_n) \tag{2.2.13}$$

where

$$\begin{pmatrix} x' \\ y' \\ z' \end{pmatrix} = \begin{pmatrix} \cos\theta_n \cos\phi_n & \cos\theta_n \sin\phi_n & -\sin\theta_n \\ -\sin\phi_n & \cos\phi_n & 0 \\ \sin\theta_n \cos\phi_n & \sin\theta_n \sin\phi_n & \cos\theta_n \end{pmatrix} \begin{pmatrix} x \\ y \\ z \end{pmatrix}$$

In Equation 2.2.12, α_n and β_n are the n-th random polarisation and phase, respectively, and α_n makes $\delta\vec{B}$ isotropic. The matrix is the combination of the rotations along the x-axis and the y-axis. Due to this matrix, Equation 2.2.13 automatically satisfies $\vec{\nabla} \cdot \vec{B} = 0$. N_m is the upper limit of the summation. If N_m becomes large, then $\delta\vec{B}$ will be isotropic. Giacalone and Jokipii sampled irregular magnetic fields by collecting four different values

of $\cos\theta_n$, ϕ, α_n and β_n randomly from each range,

$$\begin{cases} -1 < \cos\theta_n < 1 \quad (n = 1, 2, \cdots) \\ 0 < \phi_n < 2\pi \quad (n = 1, 2, \cdots) \\ 0 < \alpha_n < 2\pi \quad (n = 1, 2, \cdots) \\ 0 < \beta_n < 2\pi \quad (n = 1, 2, \cdots) \end{cases} \tag{2.2.14}$$

$A(k_n)$ in Equation 2.2.13 is expressed as the amplitude of the n-th wave mode with wave number k_n, and $A(k_n)$ determines the power spectrum of magnetic fields. As a Kolmogorov envelope to the power spectrum,

$$A^2(k_n) = \sigma^2 G(k_n) \left[\sum_{n=1}^{N_m} G(k_n) \right]^{-1}, \tag{2.2.15}$$

where

$$G(k_n) = \frac{\triangle V_n}{1 + (k_n L_c)^\gamma}. \tag{2.2.16}$$

In Equations 2.2.15 and 2.2.16, σ^2 and L_c are the wave variance and the correlation length, respectively. The correlation length corresponds to the maximum scale of magnetic irregularity. $\triangle V_n$ is a normalization factor. For a three-dimensional turbulence, $\triangle V_n = 4\pi k_n^2 \triangle k_n$. Giacalone and Jokipii noted that the index γ also depends on the dimension of the turbulence. The index γ is $\frac{11}{3}$ for a three-dimensional Kolmogorov spectrum. This irregular magnetic field $\delta\vec{B}$ is classified as an "isotropic" turbulent magnetic field.

Giacalone and Jokipii introduced another irregular magnetic field, which was called "composite" turbulent magnetic field to represent the interplanetary magnetic field. The composite magnetic field was a superposition of a slab component representing Alfven wave propagation. The composite turbulence consists of one-dimensional component $\delta\vec{B}_{1D}(z)$

	$\delta\vec{B}_{1D}(z)$	$\delta\vec{B}_{2D}(x,y)$
Equation 2.2.14	$\theta_n = 0$	$\theta_n = \frac{\pi}{2}$ and $\alpha_n = \frac{\pi}{2}$
Equation 2.2.16	$\Delta V_n = \Delta k_n$ and $\gamma = \frac{5}{3}$	$\Delta V_n = 2\pi k_n \Delta k_n$ and $\gamma = \frac{8}{3}$

Table 2.1: Conditions to obtain one-dimensional component $\delta\vec{B}_{1D}(z)$ and two-dimensional component $\delta\vec{B}_{2D}(x,y)$.

and two-dimensional component $\delta\vec{B}_{2D}(x,y)$ and is given by

$$\delta\vec{B}(\vec{r}) = \delta\vec{B}_{1D}(z) + \delta\vec{B}_{2D}(x,y). \tag{2.2.17}$$

Table 2.1 shows the conditions to obtain $\delta\vec{B}_{1D}(z)$ and $\delta\vec{B}_{2D}(x,y)$. In table 2.1, Equation 2.2.14 expresses the phases and polarisations of plane waves and Equation 2.2.16 is associated with the amplitudes of the plane waves.

Giacalone and Jokipii applied two kinds of magnetic fields, isotropic and composite magnetic field, to the propagation of cosmic rays. The motion of the charged particles along the total magnetic field is described by equation of motion,

$$\frac{d\vec{p}}{dt} = q(\vec{v} \times \vec{B}), \tag{2.2.18}$$

where q is the charge of the particle. Giacalone and Jokipii calculated the magnetic fields from Equation 2.2.13 for the particle's current position at each time step as it changes its position, and so this method does not need magnetic field interpolation, whereas Honda [11] sets magnetic fields at each lattice point initially, before following the trajectory of a particle, and therefore in Honda's method magnetic field interpolation was necessary.

Figure 2.4 shows the trajectories of two protons with different energy (1MeV=10^6eV and 100MeV=10^8eV) in turbulent magnetic fields. The magnetic fields are isotropic turbulence in Figure 2.4. If the particle energy is higher, then the gyroradius will become larger and the particles are more scattered compared to lower energy protons.

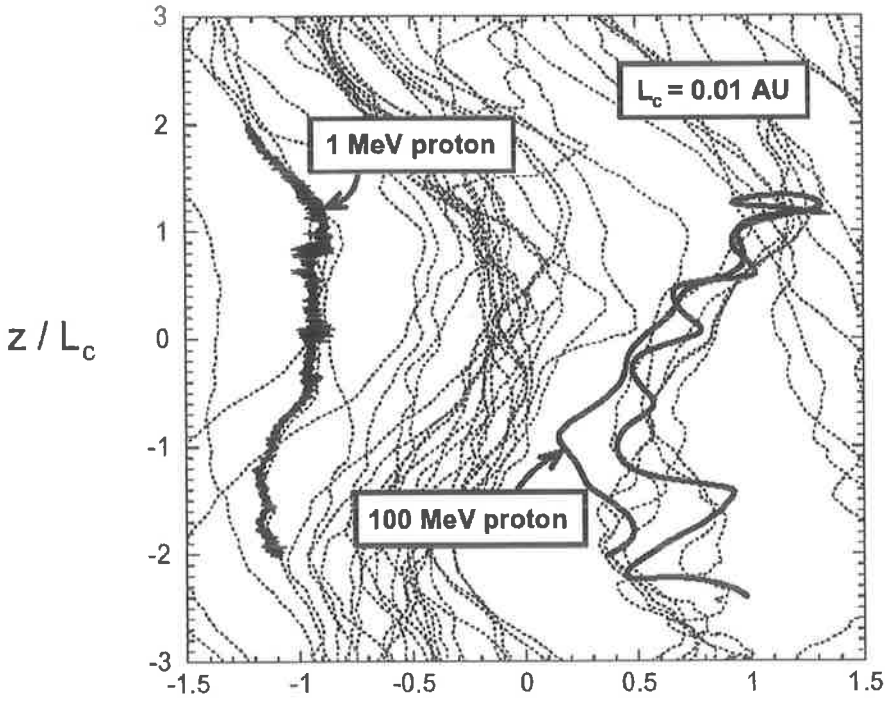

Figure 2.4: Trajectories of two protons (1MeV=10^6eV and 100MeV=10^9eV) in turbulent magnetic fields [9]. The dotted lines are magnetic field lines.

Giacalone and Jokipii were interested in how the diffusion tensors change with respect to various parameters. Figure 2.5 shows the behaviors of the diffusion tensor with respect to particle energy from 1MeV$< E <$ 100MeV. Figure 2.5 (UP) shows perpendicular component $\kappa_\perp$ versus particle energy E and Figure 2.5 (DOWN) shows the ratio $\frac{\kappa_\perp}{\kappa_\parallel}$ versus particle energy E. They applied the simulation data to the least square method and obtained $\kappa_\perp \propto E^{0.68}$. Figure 2.5 also indicates that the ratio $\frac{\kappa_\perp}{\kappa_\parallel}$ does not change much with particle energy E.

Figure 2.6 shows the behaviors of the diffusion tensor with respect to the correlation length L_c. The correlation length L_c corresponds to $0.01 \times \lambda_{max}$ (λ_{max}: maximum wavelength) and $100 \times \lambda_{mim}$ (λ_{min}: minimum wavelength). In Figure 2.6, the correlation length is

$$L_c = 10^{(n-3)/2}, \qquad n = 1, 2, 3, 4 \tag{2.2.19}$$

Figure 2.6 (UP) shows $\kappa_\perp$ versus and correlation length L_c and Figure 2.6 (DOWN) shows

the ratio $\frac{\kappa_\perp}{\kappa_\parallel}$ versus correlation length L_c. Giacalone and Jokipii used the least square method and obtained $\kappa_\perp \propto L_c^{0.46}$. They also noted that the ratio is slightly dependent upon the scale of the correlation length.

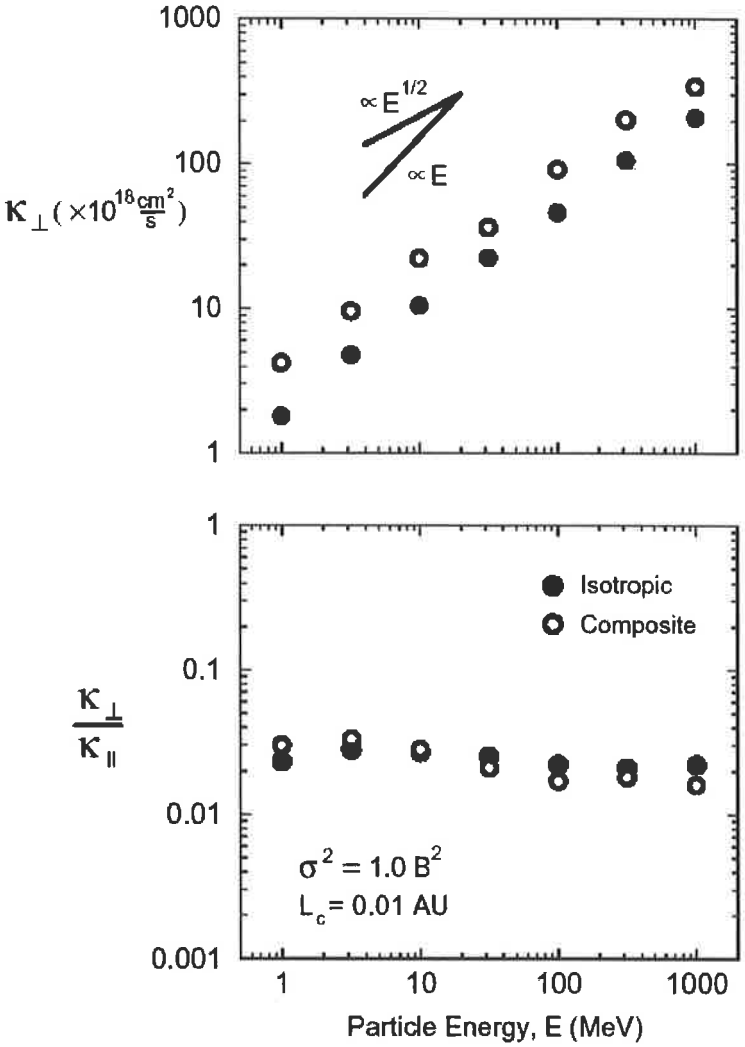

Figure 2.5: (UP) Perpendicular diffusion component $\kappa_\perp$ vs. particle energy E. (DOWN) The ratio $\frac{\kappa_\perp}{\kappa_\parallel}$ vs. E. "o" represents isotropic magnetic field and "•" represents composite magnetic field. [9].

2.2.3 Simulation by Casse, Lemoine and Pelletier (2001)

Casse, Lemoine and Pelletier [5] simulated cosmic rays diffusion in turbulent magnetic fields. This section summarizes how they simulated the propagation of charged particles. They set the three-dimensional grid space and placed magnetic fields on each grid point.

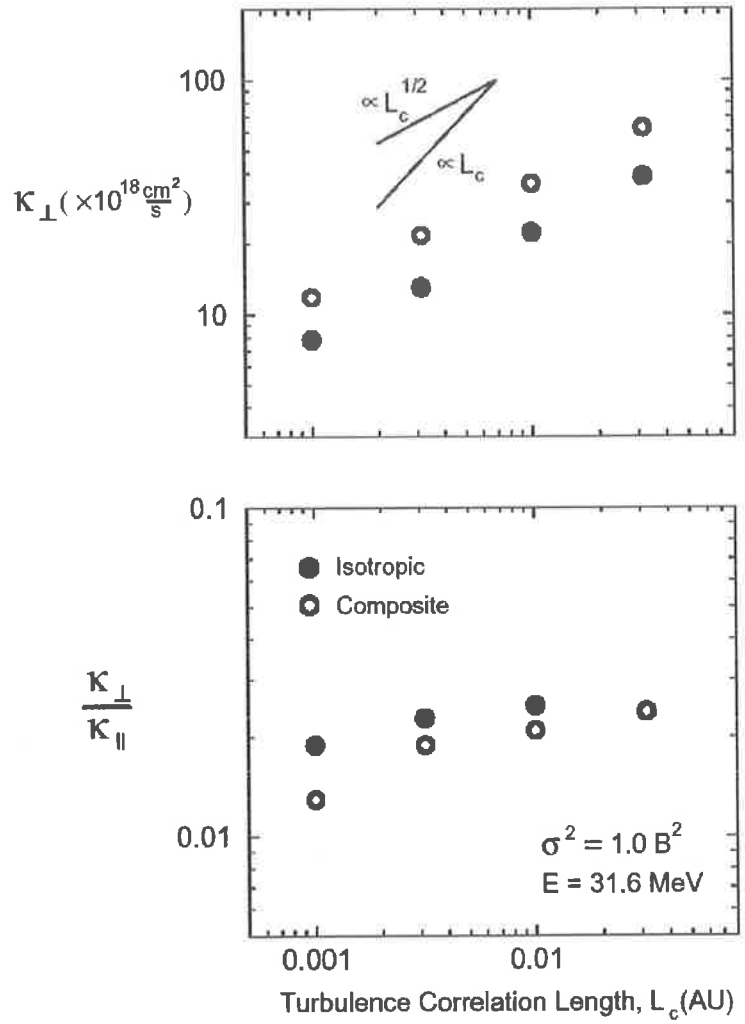

Figure 2.6: (UP) Perpendicular diffusion component$\kappa_\perp$ vs. turbulent correlation length L_c. (DOWN) The ratio $\frac{\kappa_\perp}{\kappa_\parallel}$ vs. L_c. "o" represents isotropic magnetic field and "•" represents composite magnetic field. [9].

The total magnetic fields $\vec{B}(\vec{r})$ consisted of a mean homogeneous field $\vec{B}_0$ toward z-direction and an irregular part $\delta\vec{B}(\vec{r})$, as in the simulations by Honda [11], and Giacalone and Jokipii [7] [8] [9],

$$\vec{B}(\vec{r}) = \vec{B}_0 + \delta\vec{B}(\vec{r}). \tag{2.2.20}$$

The method of Casse et al. to create the irregular magnetic fields is similar to that of Giacalone and Jokipii [9] except that they used a three-dimensional lattice. The irregular part $\delta\vec{B}(\vec{r})$ of the magnetic field was a superposition of isotropic plane waves, and was defined as,

$$\delta\vec{B}(\vec{r}) \equiv \kappa \sum_{\vec{k}} \hat{e}(\vec{k}) A(\vec{k}) \exp\left[\frac{2i\pi\vec{k}\cdot\vec{r}}{L_{max}}\right]. \tag{2.2.21}$$

In Equation 2.2.21, $\vec{k}$ is a three-dimensional wavevector, κ is a normalization factor, and $\hat{e}(\vec{k})$ is a unit vector perpendicular to $\vec{k}$. This ensures that $\delta\vec{B}(\vec{r})$ is perpendicular to the wavevector $\vec{k}$, so $\vec{\nabla}\cdot\delta\vec{B} = 0$ is automatically satisfied. $A(\vec{k})$ is the amplitude of the field component and is related to the spectrum of turbulence. For a three-dimensional Kolmogorov spectrum, $\langle A^2(\vec{k})\rangle$ is proportional to $k^{-11/3}$, so that the spectrum of turbulence follows a Kolmogorov power law. The simulation of Casse et al. used periodic boundary conditions, and set the period as L_{max}. The length between any two closest grid points is $L_{min} = \frac{L_{max}}{N_g}$, where N_g expresses the number of wavenumber modes along one direction. The typical N_g for their simulation was 256.

Casse et al. defined the turbulence level given by

$$\eta \equiv \frac{\langle\delta\vec{B}^2\rangle}{\vec{B}^2} = \frac{\langle\delta\vec{B}^2\rangle}{B_0^2 + \langle\delta\vec{B}^2\rangle} \tag{2.2.22}$$

Thus, when $\eta \ll 1$ and $\delta B(\vec{r}) \ll B_0$, B_0 dominates the total magnetic field $\vec{B}(\vec{r})$ and the turbulence was weak. On the other hand, when $\eta \gg 1$, $\delta B(\vec{r})$ dominated the total magnetic field $\vec{B}(\vec{r})$, so $\vec{B}(\vec{r})$ became more isotropic. They calculated the diffusion tensors for various turbulence levels.

Casse et al. applied a Fast Fourier Transform (FFT) algorithm to Equation 2.2.21 to reduce the number of calculations and to save computational time. FFT is more efficient than Discrete Fourier Transform (DFT) algorithms, the difference between FFT and DFT being the number of multiplications. If the number of data values in DFT is N, the number of multiplications is N^2, whereas with the FFT, the number of multiplications is reduced to $N \log_2 N$. For example, the number of data is $2^{10} = 1024$, the number of multiplications in DFT is $\sim 1.05 \times 10^6$, whereas in FFT, it is reduced to $\sim 1.02 \times 10^4$. However, the number of data values in FFT must be a power of 2.

The irregular part $\delta\vec{B}$ of the magnetic fields for both the FFT method (Equation 2.2.21) and the method of Giacalone and Jokipii (Equation 2.2.13) [9] look very similar. However, there are several differences. The method does not calculate the magnetic field on a discrete grid beforehand; rather, the magnetic fields are calculated during particle propagation from the sum of plane waves, as mentioned in Section 4.2.2

The spatial diffusion coefficient parallel to the mean magnetic field B_0 is

$$D_{\parallel} \equiv \frac{\langle \triangle x_{\parallel}^2 \rangle}{2 \triangle t} = \frac{1}{3} v^2 \tau_s \tag{2.2.23}$$

where τ_s is the scattering time. The transverse diffusion coefficient perpendicular to the mean magnetic field is

$$D_{\perp} \equiv \frac{\langle \triangle x_{\perp}^2 \rangle}{2 \triangle t} = \frac{1}{3} v^2 \frac{\tau_s}{1 + (\omega_L \tau_s)^2} \tag{2.2.24}$$

where ω_L is the Larmor frequency. Casse et al. plotted both parallel and perpendicular components of the diffusion tensor versus a dimensionless rigidity ρ (Figures 2.7 and 2.8), written in terms of gyroradius r_g and the largest scale of irregularity L_{max},

$$\rho = \frac{2\pi r_g}{L_{max}}. \tag{2.2.25}$$

They also plotted the ratio of two diffusion components $D_{\perp}/D_{\parallel}$ versus rigidity ρ (Figure 2.9). In Figures 2.7 and 2.8, they noticed that the FFT method and the method proposed

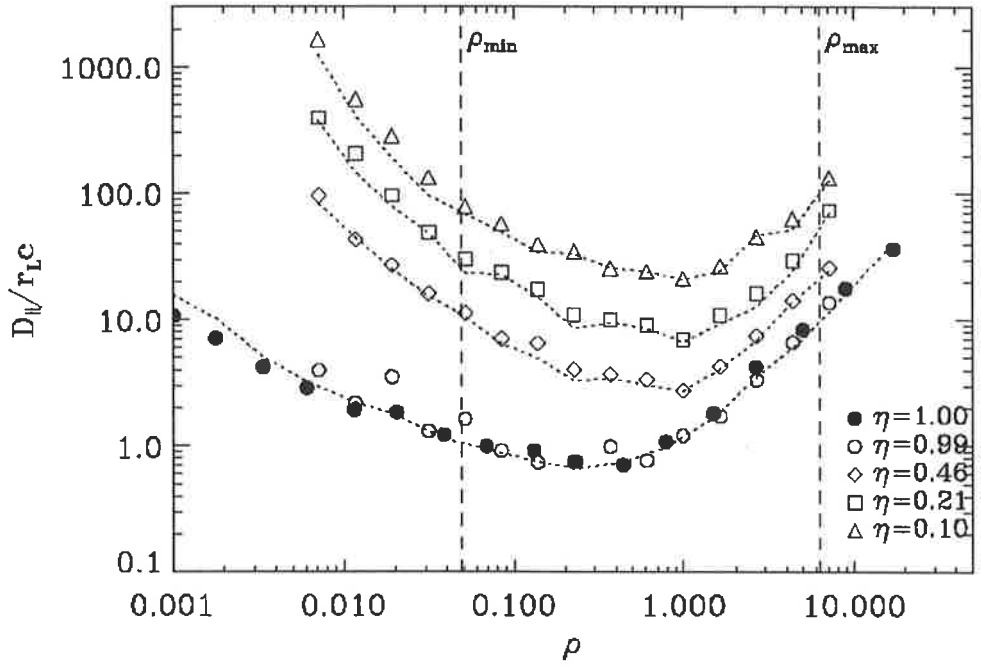

Figure 2.7: Parallel diffusion tensor $D_\parallel$ versus dimensionless rigidity ρ with various turbulence levels η. [5].

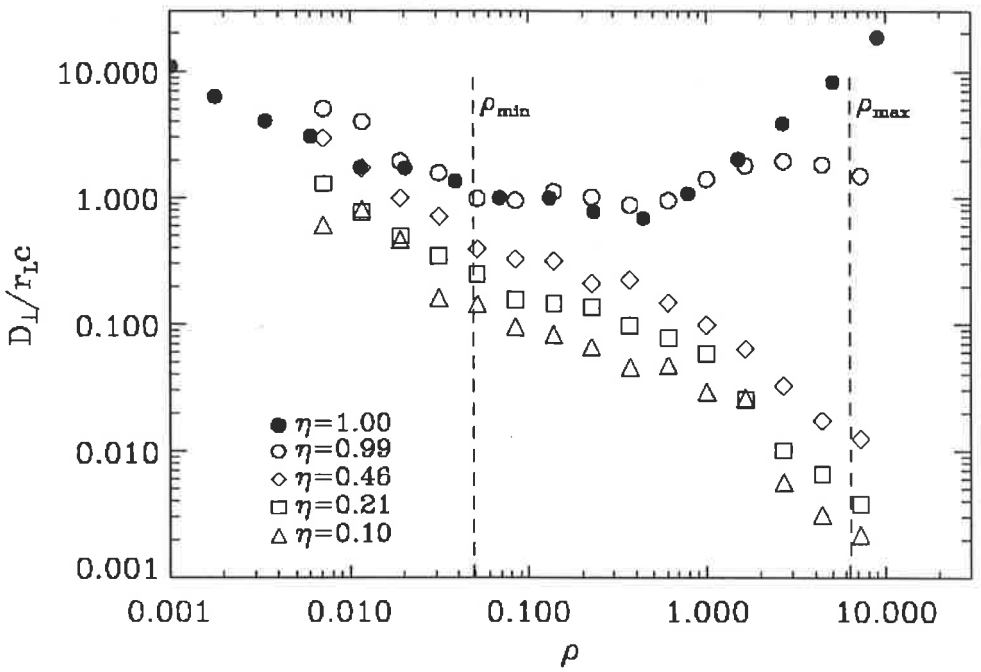

Figure 2.8: Perpendicular diffusion tensor $D_\perp$ versus dimensionless rigidity ρ with various turbulence levels η. [5].

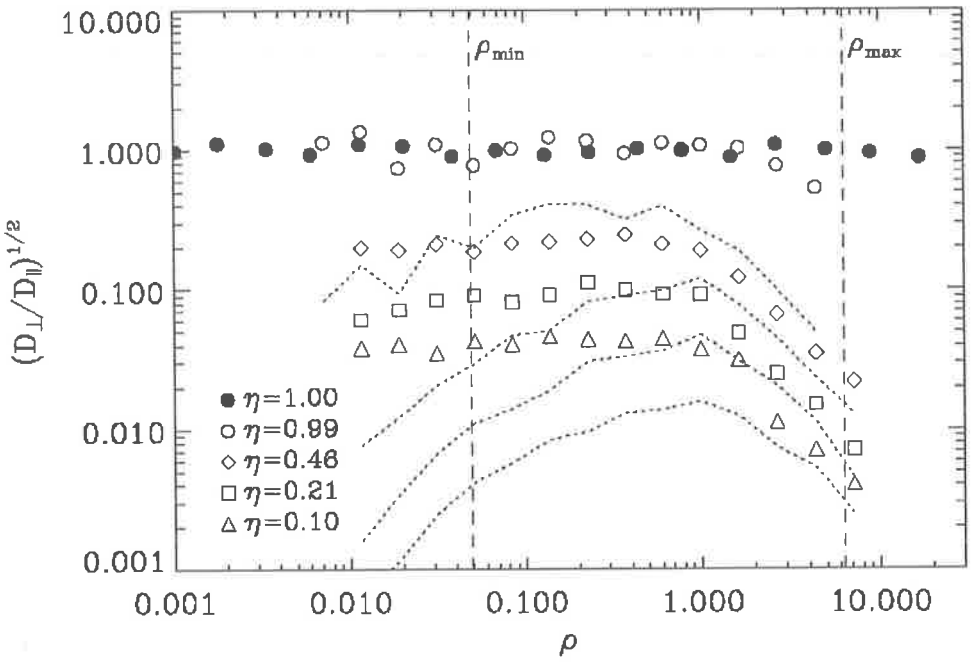

Figure 2.9: The ratio $\frac{D_\parallel}{D_\perp}$ versus dimensionless rigidity ρ with various turbulence levels η. [5].

by Giacalone and Jokipii are in agreement for the rigidity range $\rho_{min} < \rho < \rho_{max}$, where $\rho_{min} = \frac{k_{min}}{k_{max}}$ and $\rho_{max} = 2\pi$. They noticed that the ratio $D_\perp/D_\parallel$ is independent of ρ for $\rho < 1$, which is consistent with the simulation by Giacalone and Jokipii [9] (Figure 2.9).

Casse et al. applied this cosmic ray diffusion simulation to various astrophysical phenomena, such as supernovas, superbubbles and jets from active galactic nuclei. They firstly applied the simulation to supernova remnant (SNR) shocks. Kirk and Dendy [14] reviewed cosmic ray production in supernova remnants, and according to their review, Galactic supernovas produce cosmic rays with an energy range up to about 10^{14}eV to 10^{17}eV. Casse et al. found that the maximum energy for acceleration is

$$\epsilon_{SNR} \sim 1.8 \times 10^{14} Zg \left(\frac{\beta_s}{10^{-2}}\right)^2 \left(\frac{t}{300\text{yr}}\right)^2 \left(\frac{B}{1\mu\text{G}}\right) \text{eV}. \tag{2.2.26}$$

where β_s is the shock velocity over the speed of light. In Equation 2.2.26, g is a scattering function defined as $\frac{t_L}{\tau_s}$, where t_L is Larmor time or gyro-time and τ_s is scattering time.

Superbubbles are huge cavities produced by about 100×SNR shock waves created

around massive star (OB stars) associations in the interstellar medium. Parizot and Drury [20] estimated the typical superbubble radius as

$$R_{SB}(t) \cong 66\text{pc}\left(\frac{L}{10^{38}\text{erg}\cdot\text{s}^{-1}}\right)^{\frac{1}{5}}\left(\frac{n_0}{1\text{cm}^{-3}}\right)^{\frac{-1}{8}} t_{\text{Myr}}^{\frac{3}{5}}. \tag{2.2.27}$$

The maximum energy for acceleration in superbubbles is

$$\epsilon_{SB} \simeq 4\times 10^{12} Zg\left(\frac{B}{1\mu\text{G}}\right) t_{\text{Myr}}^{\frac{32}{35}}\text{eV}. \tag{2.2.28}$$

In this equation, t_{Myr} is the superbubble life time in mega year units and g is the scattering function, i.e. $\frac{t_L}{\tau_s}$, where t_L is Larmor time and τ_s is scattering time.

Extra-galactic jets from quasars are thought to be the a possible source of ultra-high energy cosmic rays, which have energy above 10^{18}eV. Casse et al. applied their simulation to Cygnus A and Centaurus A. In the Cygnus A case, inside the jet radius $R_j = 1$pc, the strength of the magnetic field B is about 10^{-5}T. The maximum energy for acceleration is

$$\epsilon_{max} \simeq 10^{21}\beta_s^3 Z\Gamma\left(\frac{B}{1\text{G}}\right)\left(\frac{R_j}{1\text{pc}}\right)\text{eV}. \tag{2.2.29}$$

In this equation, Γ is the jet's Lorentz factor, and in this case $\Gamma \simeq 10$ is needed for a cosmic ray energy larger than 10^{20}eV.

2.3 Summary and Conclusion

Section 2.2.1 to 2.2.3 review three simulations of cosmic ray diffusion in turbulent magnetic fields. The following is a summary of three simulations.

1. Simulation proposed by Honda (1987)

   (a) The total magnetic field consists of regular and irregular magnetic fields, namely $\vec{B}_{total} = \vec{B}_0 + \delta\vec{B}$.

(b) Three-dimensional grid space is used in the simulation, so the interpolation between the grid points is necessary.

(c) $\vec{\nabla} \times \vec{A}$ is applied to create irregular magnetic fields $\delta\vec{B}(\vec{r})$.

2. Simulation proposed by Giacalone and Jokipii (1999)

(a) The total magnetic field consists of regular and irregular magnetic fields, namely $\vec{B}_{total} = \vec{B}_0 + \delta\vec{B}$.

(b) The simulation does not use three-dimensional grid space. Instead they calculated magnetic fields for every step.

(c) The superposition of plane waves is used to create irregular magnetic fields $\delta\vec{B}(\vec{r})$.

3. Simulation proposed by Casse, Lemoine and Pelletier (2001)

(a) The total magnetic field consists of regular and irregular magnetic fields, namely $\vec{B}_{total} = \vec{B}_0 + \delta\vec{B}$.

(b) Three-dimensional grid in k-space (k: wavenumber) is used in the simulation, generated by FFT methods, so the interpolation between the grid points is necessary.

(c) The superposition of plane waves is used to create irregular magnetic fields $\delta\vec{B}(\vec{r})$.

The method Honda used to create irregular magnetic field is different from the two other simulations as he used $\vec{\nabla} \times \vec{A}$ to create $\delta\vec{B}$. The simulation by Giacalone and Jokipii and the simulation by Casse et al are very similar to each other because both simulations applied the superposition of isotropic plane waves to create irregular magnetic fields $\delta\vec{B}(\vec{r})$.

However, Giacalone and Jokipii did not use three-dimensional lattice, whereas Casse et al. used the k-space lattice (k: wavenumber). Therefore, even though Casse et al. used a Fast Fourier Transform algorithm to reduce computational time, the Giacalone and Jokipii simulation may be faster than the Casse et al. simulation. For this reason, this research selected two simulations, namely the simulation proposed by Honda and the simulation proposed by Giacalone and Jokipii. These two simulations were repeated and results analysed.

Chapter 3

Honda's Simulation

3.1 Summary of Honda's simulation

This section summarizes Honda's simulation [11] of cosmic ray propagation in turbulent galactic magnetic fields. He calculated diffusion tensors based on the positions of the cosmic rays in the turbulent galactic magnetic fields.

The turbulent magnetic field $\vec{B}_{total}(\vec{r})$ is composed of the mean magnetic field $B_o\hat{e}_z$ and the irregular magnetic field $\delta\vec{B}(\vec{r})$. To create an irregular magnetic field, Honda used a three-dimensional lattice and placed random vector potentials $\vec{A}(\vec{r})$ at each lattice point. The vector potentials are sampled from Monte Carlo simulation. The vector potentials are isotropic and the potentials obey exponential distribution. Then he took the curl of the vector potentials to create the irregular part of thc magnetic fields, namely

$$\delta\vec{B}(\vec{r}) = \vec{\nabla} \times \vec{A}(\vec{r}). \tag{3.1.1}$$

The curl of the vector potential ensures $\vec{\nabla} \cdot \vec{B}$ equals to 0.

To create Kolmogorov-like magnetic fields, Honda set the lattice space to have grid spacings. The magnetic fields placed on each grid point had a magnitude which depended

upon the grid spacing, the smaller magnitude for a smaller grid spacing, and the larger magnitude for the larger grid spacing. The magnetic field on the i-th smaller grid spacing was proportional to $L_i = 10^{-i/2}L_0$, where L_0 is the scale of turbulence and corresponds to the maximum grid spacing. Then the next smallest grid spacings were $L_0/10^{1/2}$, $L_0/10^1$ and so on. After the magnetic fields with corresponding magnitudes on different grid scales were placed on the grid points, the magnetic fields at each grid point was vectorially added to create the irregular part of the magnetic field. For a Kolmogorov spectrum, the weighting of the field energy density of the superimposed magnetic fields is proportional to $L_i^{5/3}$.

Honda calculated the positions of particles according to the equation of motion. To draw smooth trajectories in the simulation, setting an appropriate time step $\triangle t$ was important. He found that $\triangle t = \frac{R_g}{10c}$ was best for the time step, where R_g is the gyroradius of the particle and c is the speed of light.

In order to calculate the diffusion tensor K_{ij} ($i = x,\ y,\ z$ and $j = x,\ y,\ z$), Honda projected a number of particles into the magnetic fields and took the averages of distances for each time step. Then the diffusion tensor components were calculated from the plots of squared average distance versus time.

$$\langle z^2 \rangle = 2K_{\parallel}t, \tag{3.1.2}$$

$$\langle x^2 + y^2 \rangle = 4K_{\perp}t, \tag{3.1.3}$$

where $K_{\parallel}$ is the diffusion tensor component parallel to the z-direction and $K_{\perp}$ is the diffusion tensor component perpendicular to the z-direction. Each component of the diffusion tensor was the slope in the average squared distance versus time plot.

3.2 Repeating Honda's Method (The case of single grid space)

Section 3.2 describes how Honda's simulation was reproduced for the case of a single grid spacing for the magnetic field, and discusses the results of the simulation.

3.2.1 Producing and Sampling Magnetic Fields

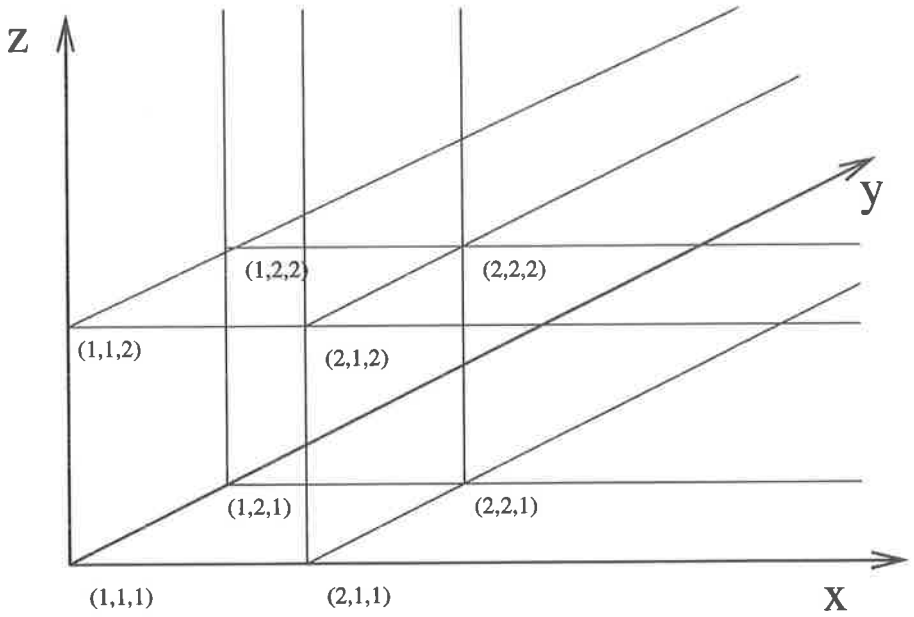

Figure 3.1: Single grid spacing three-dimensional lattice space. Magnetic fields $\vec{B}_{total}(\vec{r})$ are placed on each lattice point. In order to create Kolmogorov-type magnetic fields, lattice spaces which have different scale of grid spacing are used.

This section describes how the magnetic fields on the grid points are set. Firstly, the three-dimensional lattice was set to place magnetic fields (Figure 3.1). Periodic boundary conditions were used to repeat the lattice. Honda sampled the vector potentials randomly to calculate irregular magnetic field $\delta\vec{B}$. Honda sampled from an exponential distribution. However, since the directions of magnetic field lines are isotropic, it would be better to sample both positive and negative vector potentials. Hence the normal distribution was used in this study to allow for both positive and negative values of vector potentials. After

sampling the vector potentials $\vec{A}$,

$$\delta\vec{B} = \vec{\nabla} \times \vec{A}, \tag{3.2.1}$$

was calculated. The algorithm of Equation 3.2.1 is as follows. Firstly the vector potentials $\vec{A}_{ijk} = (A^x_{ijk}, A^y_{ijk}, A^z_{ijk})$ were sampled from the Monte Carlo simulation. The index number i, j, k represents the grid point where the vector potential is located. According to the definition of $\vec{\nabla} \times \vec{A} = (B^x_{ijk}, B^y_{ijk}, B^z_{ijk})$, x-, y- and z-components are

$$\begin{aligned} B^x_{ijk} &= \left(\frac{dA^z_{ijk}}{dy} - \frac{dA^y_{ijk}}{dz}\right) \\ B^y_{ijk} &= \left(\frac{dA^x_{ijk}}{dz} - \frac{dA^z_{ijk}}{dx}\right) \\ B^z_{ijk} &= \left(\frac{dA^y_{ijk}}{dx} - \frac{dA^x_{ijk}}{dy}\right) \end{aligned} \tag{3.2.2}$$

The root mean square (r.m.s.) value of $\vec{B}$ was set to be 1.0×10^{-10} T(=1.0μG) and of $\vec{A}$ was set to be 1.0×10^{-10}T·pc. The intervals $\triangle x$, $\triangle y$, $\triangle z$, which correspond to grid spacing, were 1.0 pc. The infinitesimal vector potential $\triangle\vec{A}_{ijk}(\vec{r})$ along the $\vec{r} = (x, y, z)$ direction was calculated as

$$\begin{aligned} \frac{\triangle A^x_{ijk}}{\triangle x} &= \frac{A_{i+1jk} - A_{ijk}}{(1.0\text{ pc})} \\ \frac{\triangle A^y_{ijk}}{\triangle y} &= \frac{A_{ij+1k} - A_{ijk}}{(1.0\text{ pc})} \\ \frac{\triangle A^z_{ijk}}{\triangle z} &= \frac{A_{ijk+1} - A_{ijk}}{(1.0\text{ pc})} \end{aligned}. \tag{3.2.3}$$

The periodic boundary condition was applied in the simulation so that the index number repeated after the end of grid points, and so the calculation of $\vec{B}_{ijk}(\vec{r}) = (B^x_{ijk}, B^y_{ijk}, B^z_{ijk})$ was

$$\begin{aligned} B^x_{ijk} &= \frac{\triangle A^z_{ijk}}{\triangle y} - \frac{\triangle A^y_{ijk}}{\triangle z} = \frac{A^z_{ij+1k} - A^z_{ijk}}{(1.0\text{ pc})} - \frac{A^y_{ijk+1} - A^y_{ijk}}{(1.0\text{ pc})} \\ B^y_{ijk} &= \frac{\triangle A^x_{ijk}}{\triangle z} - \frac{\triangle A^z_{ijk}}{\triangle x} = \frac{A^x_{ijk+1} - A^x_{ijk}}{(1.0\text{ pc})} - \frac{A^z_{i+1jk} - A^z_{ijk}}{(1.0\text{ pc})} \\ B^z_{ijk} &= \frac{\triangle A^y_{ijk}}{\triangle x} - \frac{\triangle A^x_{ijk}}{\triangle y} = \frac{A^y_{i+1jk} - A^y_{ijk}}{(1.0\text{ pc})} - \frac{A^x_{ij+1k} - A^x_{ijk}}{(1.0\text{ pc})} \end{aligned} \tag{3.2.4}$$

The following two cases were compared.

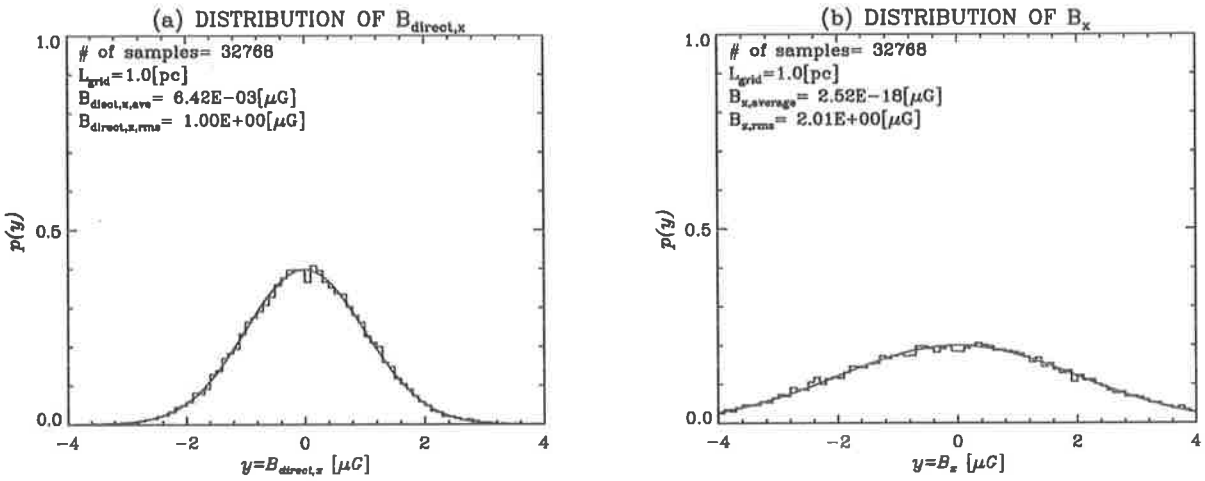

Figure 3.2: Distributions of x-component of magnetic fields. (a) Distribution of $B_{direct,x}$. $\vec{B}_{direct}$ are sampled directly from Monte Carlo simulation. (b) Distribution of B_x. Vector potentials are initially sampled from Monte Carlo simulation and $\vec{B}$ is calculated from $\vec{\nabla} \times \vec{A}$. The solid curves were calculated from Equation 3.2.5

1. The magnetic fields are sampled directly (CASE 1).

2. Vector potentials are sampled, and the magnetic fields are calculated from $\vec{\nabla} \times \vec{A}$ (CASE 2).

The calculation of CASE 1 simulation is faster than that of CASE 2 simulation. Therefore if the magnetic fields sampled directly from the Monte Carlo simulation CASE 1 agree with the magnetic fields from CASE 2 simulation, it would be better to choose CASE 1 for simulation, to reduce computational time. Figure 3.2 shows the distribution of the x-component of the irregular magnetic fields by using a Monte Carlo simulation. The smooth solid curves in Figure 3.2 were calculated from normal distribution function defined as

$$f(B_x) = \frac{1}{B_{x,rms}\sqrt{2\pi}} \exp\left[\frac{1}{2}\left(\frac{B_x}{B_{x,rms}}\right)^2\right] \tag{3.2.5}$$

Figure 3.2 (a) shows the distribution of $B_{direct,x}$ sampled directly from the Monte Carlo simulation (CASE 1), and Figure 3.2 (b) shows the distribution of B_x, which was calculated by $\vec{\nabla} \times \vec{A}$ (CASE 2). Figure 3.2 (a) shows that the distribution of $B_{direct,x}$ is consistent with the normal distribution curve (Equation 3.2.5) with $B_{x,rms} = 1.0\mu$G, whereas in Figure 3.2 (b), the B_x distribution from CASE 2 simulation has a different distribution pattern. The B_x distribution spreads more widely than $B_{direct,x}$ distribution and B_x distribution agrees to the normal distribution curve (Equation 3.2.5) with the r.m.s. value, $B_{direct,x,rms} = 2.0\mu$G. The calculation of $\vec{\nabla} \times \vec{A}$ may affect the B_x distribution and $B_{x,rms}$. Therefore, the normalisation of B_x by $B_{x,rms} = 2.0\mu$G was implemented and the B_x histogram which agreed to the normal distribution curve with $B_{x,rms} = 1.0\mu$G was obtained.

3.2.2 Verifying the magnetic fields

It is important to check whether the sampled magnetic fields are valid before they are used as the irregular magnetic fields $\delta\vec{B}$. This section examines the magnetic fields sampled in the Monte Carlo simulation. Two tests were implemented. The first one is to test whether the calculation of $\vec{\nabla} \times \vec{A}$ produces an appropriate magnetic field $\vec{B}$. Generally speaking, any magnetic field $\vec{B}$ must satisfy the relationships explained in the following paragraphs.

Suppose an initial field line is directed in the z-direction in a cylindrical coordinate system,

$$\vec{B}_i = |\vec{B}_i|\hat{e}_z. \tag{3.2.6}$$

One representation of the vector potential from the initial magnetic field is

$$\vec{A} = -\frac{|\vec{B}_i|}{2}\rho\hat{e}_\varphi, \tag{3.2.7}$$

where (ρ, φ, z) are cylindrical coordinates. The magnetic field finally created from this

vector potential is

$$\vec{B}_f = \vec{\nabla} \times \vec{A}. \tag{3.2.8}$$

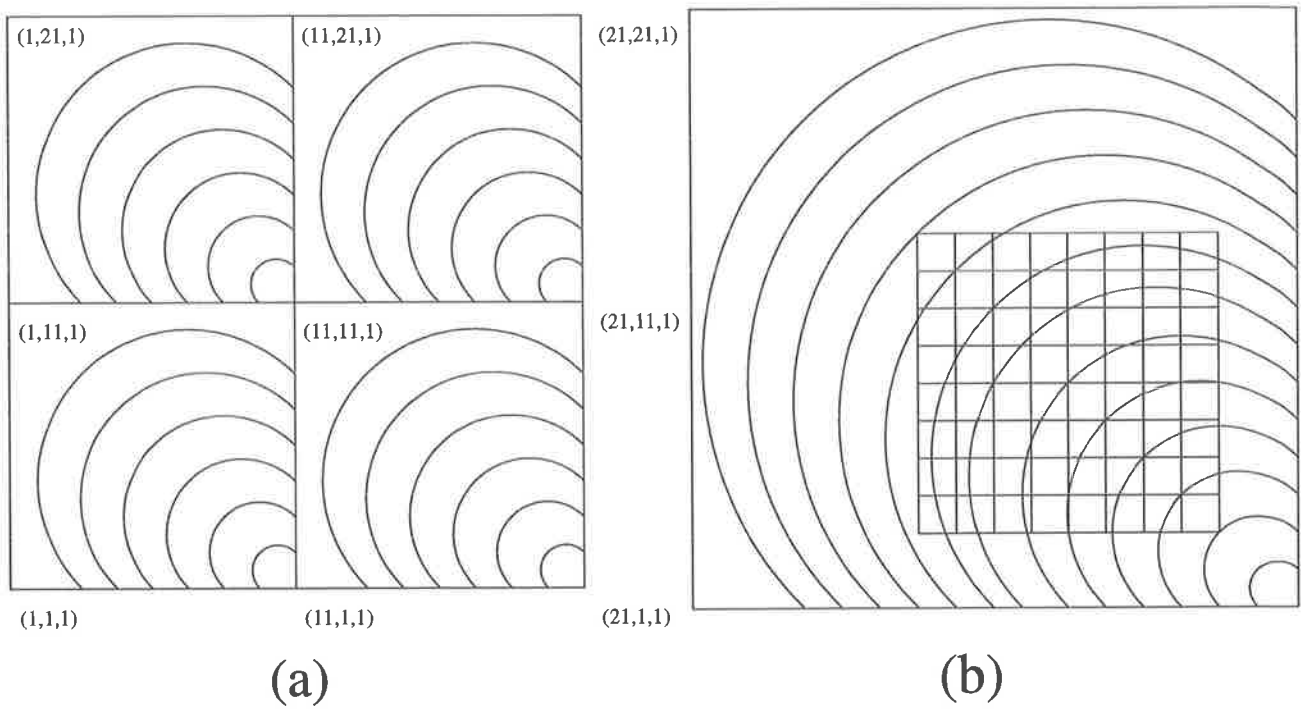

Figure 3.3: (a) two-dimensional schematic diagram of vector potential lines in each cube. (b) Testing magnetic fields inside the cube to avoid "edge problem".

If the magnetic field is electro-magnetically correct, the initial magnetic field must be consistent with the final magnetic field, ie, $|\vec{B}_i| = |\vec{B}_f|$. To test the magnetic fields produced by $\vec{\nabla} \times \vec{A}$, the edge of the lattice must be considered. Since the simulation uses periodic boundary condition for the lattice, the vector potential lines at the boundary do not fit to those of the next lattice cube. Figure 3.3 (a) is a two-dimensional schematic picture of this problem involving the implementation of the first magnetic field test. The box in Figure 3.3 (b) represents part of the lattice of $10 \times 10 \times 10$ grid points. Figure 3.3 (a) shows that the vector potential lines in a box are inconsistent with those of neighbouring boxes. Therefore, the test was implemented only inside the initial cube to avoid this

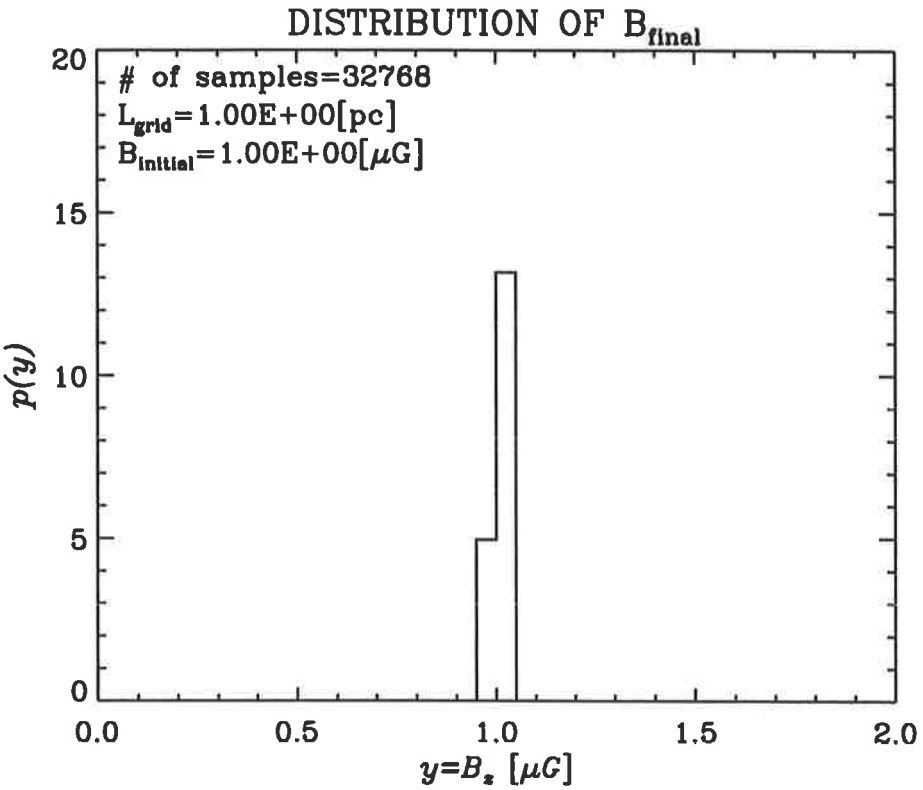

Figure 3.4: Distribution of B_f. Input value $B_i = 1.0\mu$G

"edge problem", as shown in Figure 3.3 (b). Figure 3.4 shows that the distribution of final magnetic fields B_f in the first magnetic field test. Input value was 1.0×10^{-10} T$(= 1.0\mu$G), and the total grid points were $32 \times 32 \times 32 = 32768$ points. The distribution of the B_f was consistent with the initial value $|\vec{B}_i|$, namely 1.0μG. Therefore, the first test concludes that the procedure of producing magnetic fields by $\vec{\nabla} \times \vec{A}$ is valid.

The second test comes from Maxwell's equations (Faraday's law). According to the Maxwell's equations and because magnetic fields have no point source to flow from, all magnetic fields must satisfy this condition,

$$\vec{\nabla} \cdot \vec{B} = 0. \tag{3.2.9}$$

Testing the magnetic fields produced by the Monte Carlo simulation for the condition 3.2.9 was implemented. Numerical calculation of $\vec{\nabla} \cdot \vec{B}$ is explained as follows. By definition,

$\vec{\nabla} \cdot \vec{B}$ is

$$\vec{\nabla} \cdot \vec{B}_{ijk} = \frac{\partial B^x_{ijk}}{\partial x} + \frac{\partial B^y_{ijk}}{\partial y} + \frac{\partial B^z_{ijk}}{\partial z}. \tag{3.2.10}$$

The intervals $\triangle x$, $\triangle y$, $\triangle z$ were set to be 1.0pc in this test. The infinitesimal magnetic field $\triangle B^x_{ijk}$ along the $\vec{r} = (x,\ y,\ z)$ direction is calculated as

$$\begin{aligned} \frac{\triangle B^x_{ijk}}{\triangle x} &= \frac{B^x_{i+1jk} - B^x_{ijk}}{(1.0\text{ pc})} \\ \frac{\triangle B^y_{ijk}}{\triangle y} &= \frac{B^y_{ij+1k} - B^y_{ijk}}{(1.0\text{ pc})} \\ \frac{\triangle B^z_{ijk}}{\triangle z} &= \frac{B^z_{ijk+1} - B^z_{ijk}}{(1.0\text{ pc})} \end{aligned} \tag{3.2.11}$$

Finally the numerical result of the $\vec{\nabla} \cdot \vec{B}$ is obtained,

$$\begin{aligned} \vec{\nabla} \cdot \vec{B}_{ijk} =& \frac{\triangle B^x_{ijk}}{\triangle x} + \frac{\triangle B^y_{ijk}}{\triangle y} + \frac{\triangle B^z_{ijk}}{\triangle z}. \\ =& \frac{B^x_{i+1jk} - B^x_{ijk}}{(1.0\text{ pc})} + \frac{B^y_{ij+1k} - B^y_{ijk}}{(1.0\text{ pc})} + \frac{B^z_{ijk+1} - B^z_{ijk}}{(1.0\text{ pc})} \end{aligned} \tag{3.2.12}$$

The test made a comparison among following three simulation cases:

1. The magnetic fields are sampled directly (CASE 1).

2. Vector potentials are sampled, and the magnetic fields are calculated from $\vec{\nabla} \times \vec{A}$ (CASE 2).

3. Vector potentials are sampled, and the magnetic fields are calculated from $\vec{\nabla} \times \vec{A}$, and then all magnetic fields are normalized by the root mean square (r.m.s.) value of $\vec{B}$ (CASE 3).

The r.m.s. value of the magnetic fields was set to be 1.0×10^{-10}T$(= 1.0\mu$G) for this test. The number of the magnetic fields was $n = 32 \times 32 \times 32 = 32768$ and the mean values of the $\vec{\nabla} \cdot \vec{B}$ were calculated for each case. If the mean value of the $\vec{\nabla} \cdot \vec{B}$ was close to 0, the set of the magnetic fields will be realistic for the simulation.

	(CASE 1)	(CASE 2)	(CASE 3)
	$\vec{\nabla} \cdot \vec{B}_{direct}$	$\vec{\nabla} \cdot \vec{B} = \vec{\nabla} \cdot (\vec{\nabla} \times \vec{A})$	$\vec{\nabla} \cdot \vec{B} = \vec{\nabla} \cdot (\vec{\nabla} \times \vec{A})$(normalized)
mean	-1.738×10^{-28} T/m	-1.942×10^{-43} T/m	-5.259×10^{-44} T/m
σ	7.799×10^{-27} T/m	1.344×10^{-26} T/m	6.694×10^{-27} T/m
$\sigma/\sqrt{n}$	4.308×10^{-29} T/m	7.425×10^{-29} T/m	3.698×10^{-29} T/m

Table 3.1: Mean, standard deviation and standard error of $\vec{\nabla} \cdot \vec{B}$ for 3 cases. σ is standard deviation and $\sigma/\sqrt{n}$ is standard error.

Table 3.1 shows the mean value, the standard deviation and standard error of $\vec{\nabla} \cdot \vec{B}$ in three cases. Compared to the mean value, standard deviation and standard error of CASE 1 $\vec{\nabla} \times \vec{B}$, those values of $\vec{\nabla} \times \vec{B}$ calculated from CASE 2 and CASE 3 simulations are small. CASE 2 and CASE 3 have $\langle \vec{\nabla} \cdot \vec{B} \rangle \ll \sigma$, i.e. $\langle \vec{\nabla} \cdot \vec{B} \rangle$ is close to 0. Even though sampling the magnetic fields directly from the Monte Carlo simulation can reduce the number of calculations and save computational time, the magnetic fields from the $\vec{B} = \vec{\nabla} \times \vec{A}$ calculation are more valid than CASE 1 magnetic fields from the the electromagnetic point of view.

3.2.3 Trajectories of charged particles in the magnetic fields

After testing the magnetic fields, the position of a charged particle in the turbulent magnetic field was calculated by using the equation of motion. When the particle moves inside the cube, the magnetic field at the position of the particle was interpolated. When the motion of the charged particle is considered, it is important to set the time increment for the numerical integration in the simulation.

A charged particle entering a uniform magnetic fields moves helically along the magnetic field lines as shown in Figure 3.5 (a). The gyroradius of a charged particle whose

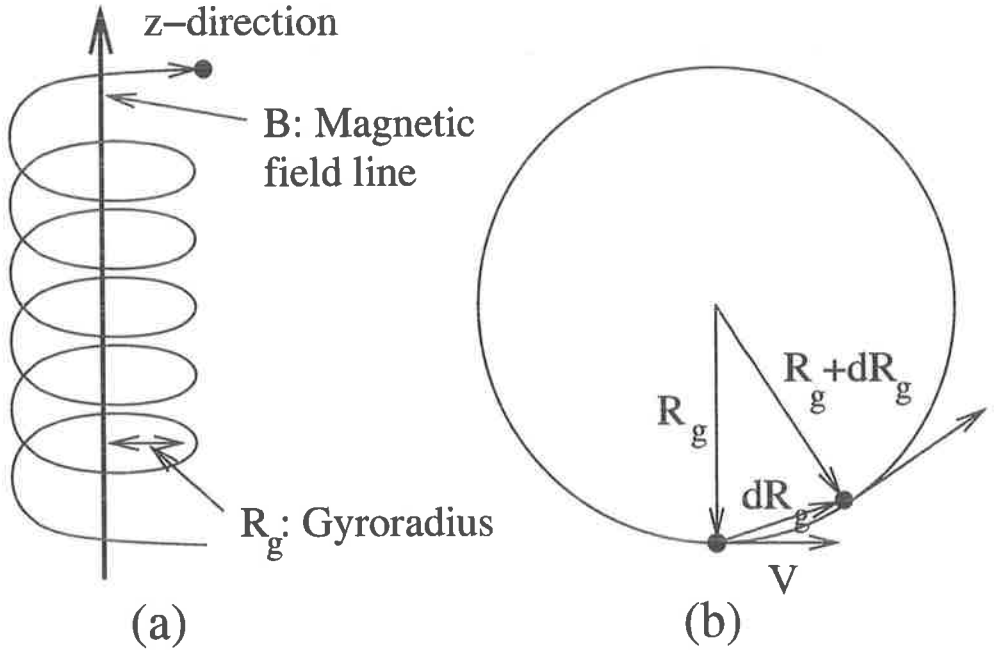

Figure 3.5: (a) Schematic diagram of the motion of a charged particle along uniform magnetic field directing z-direction. (b) Two-dimensional view of the motion from z-direction.

mass is m is given by,

$$R_g = \frac{\gamma m v \sin\theta}{e|\vec{B}|} \tag{3.2.13}$$

where γ is Lorenz factor and v is a speed of the particle. $|\vec{B}|$ is the magnitude of the magnetic field and θ is the pitch angle. The position of the particle after time $t' = t + \triangle t$ is given by

$$\begin{aligned} \vec{r}(t+\triangle t) &= \vec{r}(t) + \triangle\vec{r} \\ &= \vec{r}(t) + \vec{v}(t)\triangle t \end{aligned} \tag{3.2.14}$$

To describe the particle trajectory, two things must be considered, the first is setting the step size $\triangle t$ for the simulation and the second is to physically correct for the artificial increase of radial velocity when the trajectory is calculated. Supposing that a particle moves in a circular orbit with the radius R_g, shown in Figure 3.5 (b). $|\triangle\vec{r}|$ is given by $\triangle\theta R_g$, then the step size $\triangle t$ is given by

$$\triangle t = \frac{|\triangle\vec{r}|}{|\vec{v}|} = \frac{\triangle\theta R_g}{|\vec{v}|} \tag{3.2.15}$$

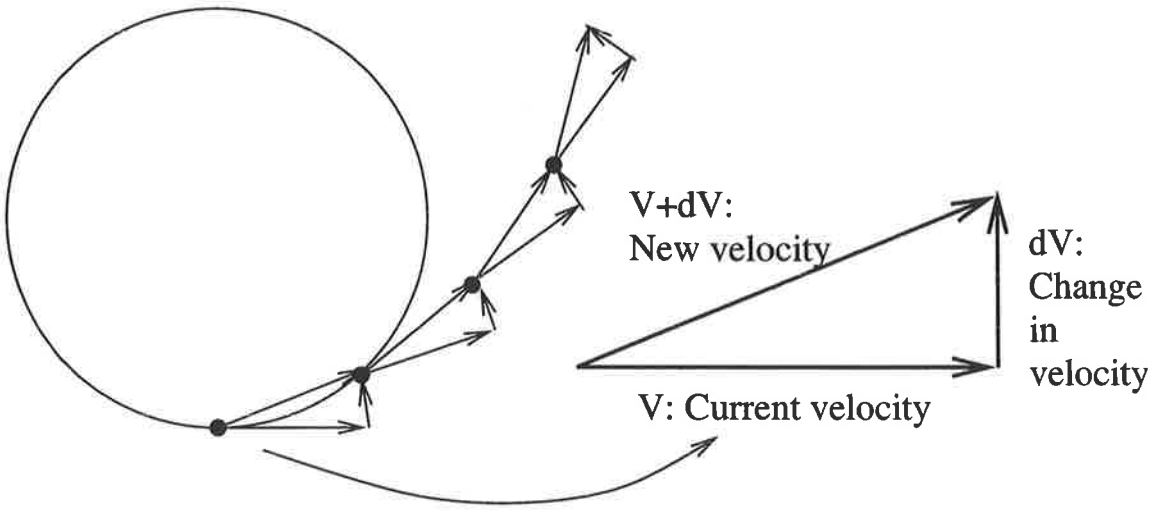

Figure 3.6: Unphysical increase of radial velocity in circular motion. A charged particle does not circulate but it deviates from the circular orbit and moves spirally.

In order to save computational time and to draw a smooth trajectory, it is necessary to set an appropriate $\triangle\theta$. Honda found that $\triangle\theta$ should be as small as $\pi/1800 = 1.745 \times 10^{-3}$ rad or 0.1°.

The second thing to be considered is the physical problem that the trajectory of a particle deviates from a circular orbit when it moves. Figure 3.6 shows how the direction of velocity vector changes and the particle deviates from circular orbit. The static magnetic fields should change only cosmic ray direction and but not its speed. However as shown in Equation 3.2.16, the change in particle velocity $\triangle\vec{v}$ is added to current velocity $\vec{v}_{curr}$, the magnitude of the new velocity increase.

$$\vec{v}_{new} = \vec{v}_{curr} + \triangle\vec{v}, \qquad |\vec{v}_{new}| > |\vec{v}_{curr}| \tag{3.2.16}$$

This causes a change in the speed of the cosmic ray and its deviation from a circular orbit, as shown in Figure 3.6. To avoid this problem, the following treatment should be implemented. Supposing the initial velocity is $\vec{v}_1$, and the Lorentz force produces the change in velocity $\triangle\vec{v}$, the new velocity $\vec{v}_2$ will be produced by adding $\triangle\vec{v}$ to $\vec{v}_1$. After the new velocity $\vec{v}_2$ is created, $\vec{v}_2$ is normalised such that its magnitude, $|\vec{v}_2|$, is equal to that

of the old velocity $|\vec{v}_1|$ since in this simulation we are only interested in ultra relativistic particles ($|\vec{v}| = c$). This normalisation of new velocities is repeated every time step, namely

$$\begin{cases} \vec{v}_1 \ : \quad \text{Initial velocity} \\ \vec{v}_2 = \vec{v}_1 + \triangle\vec{v}, \qquad \vec{v}_2 = (\vec{v}_2 c)/|\vec{v}_2| \\ \vec{v}_3 = \vec{v}_2 + \triangle\vec{v}, \qquad \vec{v}_3 = (\vec{v}_3 c)/|\vec{v}_3| \\ \vec{v}_4 = \vec{v}_3 + \triangle\vec{v}, \qquad \vec{v}_4 = (\vec{v}_4 c)/|\vec{v}_4| \\ \cdots \end{cases} \tag{3.2.17}$$

After these two treatments were done, the simulation was carried out to draw the trajectory of a charged particle in the turbulent magnetic field. In the simulation, each particle starts from the origin (0, 0, 0), but the direction of particle's velocity is arbitrary.

Table 3.2 shows the initial values of the cosmic ray energy and the magnetic field in the simulation. In Table 3.2, a proton is chosen as the particle injected into the magnetic field lattice. The range of the proton energy E is 10^{13}eV$< E < 10^{17}$eV and the corresponding gyroradius range for $B_0 = 10^{-10}$T is 0.01pc$< R_g <$ 100pc. The root mean square (r.m.s.) value of the irregular magnetic field, $|\delta\vec{B}_{rms}|$, adopted in these simulations is 10^{-10} T. The Lorentz factor γ for $E = 10^{15}$ eV is calculated as

$$E = \gamma m_p c^2 \tag{3.2.18}$$

$$\therefore \gamma = \frac{E}{m_p c^2} = \frac{10^{15}\ \text{eV}}{938\ \text{MeV}} = 1.066 \times 10^6 \tag{3.2.19}$$

From Equations 3.2.13 and 3.2.19, the gyroradius R_g for $E = 10^{15}$eV is

$$\begin{aligned} R_g = \frac{\gamma m_p v \sin\theta}{eB} &= 3.339 \times 10^{16}\ \text{m} \\ &= 1.082\ \text{pc} \end{aligned} \tag{3.2.20}$$

The angle $\theta = 90°$ was chosen so that R_g is the maximum gyroradius for this energy.

Particle	proton ($m_p = 938$ MeV/c^2)
Energy, E	10^{13}eV$< E < 10^{17}$eV
$\lvert\delta\vec{B}_{rms}\rvert$	10^{-10} T
R_g	0.01pc$< R_g <$ 100pc
Grid space, L_{min}	1.0pc
Step size, $\triangle t$	$1,9 \times 10^3$sec$< \triangle t < 1.9 \times 10^7$sec
Number of grid points	$32 \times 32 \times 32 = 32768$

Table 3.2: Some important values of the cosmic ray and the magnetic fields in the simulation

The step size $\triangle t$ is calculated by Equation 3.2.15 and the corresponding range of step size for the energy range is 1.9×10^3sec$< \triangle t < 1.9 \times 10^7$sec. The number of steps in the simulation is 5×10^6 and trajectory of cosmic ray is displayed at every 100 steps. The number of grid points is $32 \times 32 \times 32$ and the periodic boundary condition is used, so that the magnetic fields repeat every 32-grid.

I consider four possibilities:

1. Vector potentials $\vec{A}$ are sampled at grid points, and magnetic fields $\vec{B}$ are calculated from $\vec{\nabla} \times \vec{A}$, and interpolated between grid points (CASE 1).

2. Magnetic fields are sampled directly at grid points, and interpolated between grid points (CASE 2).

3. Vector potentials $\vec{A}$ are sampled at grid points, and magnetic fields $\vec{B}$ are calculated from $\vec{\nabla} \times \vec{A}$, but are not interpolated between grid points (CASE 3).

4. Magnetic fields are sampled directly at grid points, but are not interpolated between grid points (CASE 4).

	$\vec{\nabla} \times \vec{A}$	Interpolation
CASE 1	○	○
CASE 2	×	○
CASE 3	○	×
CASE 4	×	×

Table 3.3: The four cases of the simulation. ○ represents the calculation is implemented. × represents the calculation is not implemented.

Table 3.3 shows which of the four cases have been interpolated. In CASE 1 the magnetic field is potentially the most realistic turbulent magnetic field among the four cases, but CASE 1 takes much more computational time. In CASE 2 the simulation may not produce a realistic magnetic field because field $\delta\vec{B}$ is directly sampled, and so the magnetic fields do not exactly satisfy the condition, $\vec{\nabla} \cdot \vec{B} = 0$. In CASE 3 and CASE 4, the turbulent magnetic fields are uniform inside each cube because the magnetic field inside a cube is not interpolated but is set to that at the nearest grid point. However calculations using CASE 3 or CASE 4 for simulation are much faster than CASE 1 or CASE 2 because no interpolation subroutines are included. In practice, if any of the results from CASE 2, CASE 3 and CASE 4 are similar to those at CASE 1, any one of the three methods could be used to simulate cosmic ray diffusion in turbulent magnetic fields.

Figures 3.7 to 3.12 show the examples of trajectories. In the simulation, the total magnetic field B_{total} consists of mean and irregular magnetic field, and the mean part B_0 is 10^{-10}T and the r.m.s. value of the irregular part $|\delta\vec{B}_{rms}|$ is 0.5×10^{-10}T.

Figure 3.7 (a) shows an example of the trajectory of a low energy proton ($E = 10^{13}$eV) in CASE 1 and Figure 3.7 (b) shows a trajectory of a low energy proton in CASE 2. In Figure 3.7 (a) and (b), the proton moves helically along the magnetic field lines due to

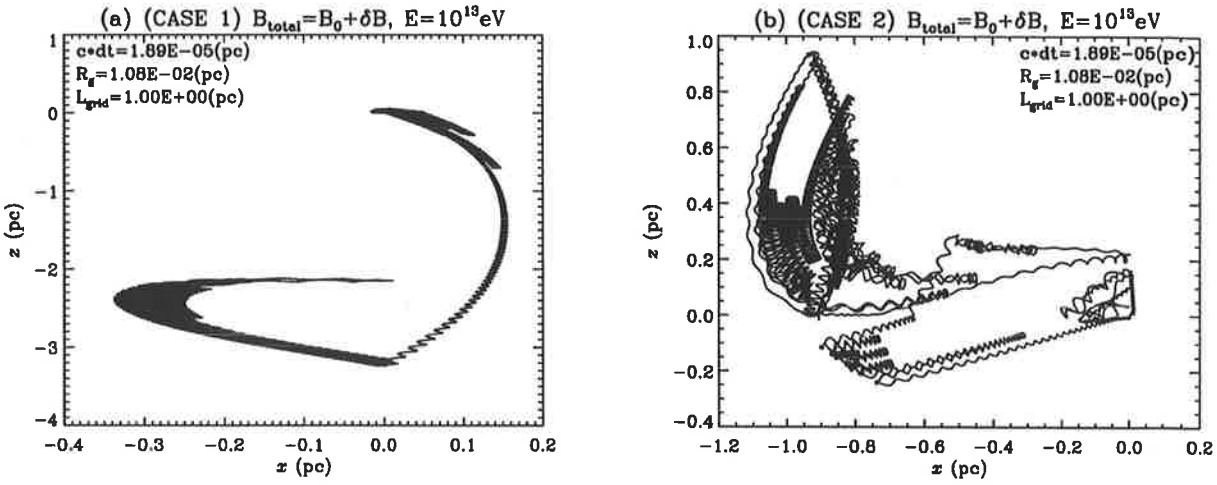

Figure 3.7: (a) (CASE 1) Trajectory of 10^{13}eV proton. (b) (CASE 2) Trajectory of 10^{13}eV proton. The mean magnetic field B_0 is 10^{-10}T and the r.m.s. value of $\delta\vec{B}$ is 10^{-10}T. The grid spacing (=turbulence scale) L_{grid} is 1.0pc.

the small gyroradius ($R_g \approx 0.01 L_{grid}$).

Figure 3.8 (a) shows the trajectory of a low energy proton ($E = 10^{13}$eV) in CASE 3 magnetic field and Figure 3.8 (b) shows the trajectory of a low energy proton in CASE 4 magnetic field. In CASE 3 and CASE 4, the magnetic fields inside the cell are not interpolated, so the magnetic fields inside the cell are uniform. In Figure 3.8, the low energy protons follow the magnetic field with $\approx 0.01 L_{grid}$ of gyroradius. However, the trajectories are not smooth in Figure 3.8, because of the magnetic fields inside the cell not being interpolated.

Figures 3.9 and 3.10 show examples of trajectories of higher energy protons ($E = 10^{15}$eV). The gyroradius of 10^{15}eV proton for $B_0 = 10^{-10}$T is $\sim$ 1.0pc, and is comparable to grid spacing L_{grid}.

Figures 3.11 and 3.12 show examples of trajectories of higher energy protons ($E = 10^{17}$eV). In Figures 3.11 and 3.12, the proton energy is sufficiently high that it is less

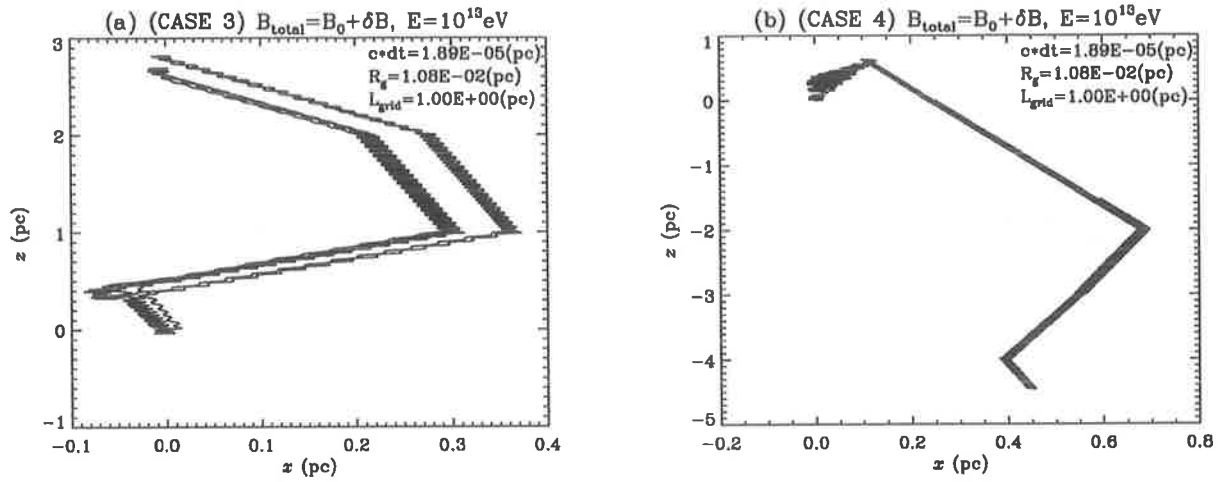

Figure 3.8: (a) (CASE 3) Trajectory of 10^{13}eV proton. (b) (CASE 4) Trajectory of 10^{13}eV proton. The mean magnetic field B_0 is 10^{-10}T and the r.m.s. value of $\delta\vec{B}$ is 10^{-10}T. The grid spacing (=turbulence scale) L_{grid} is 1.0pc.

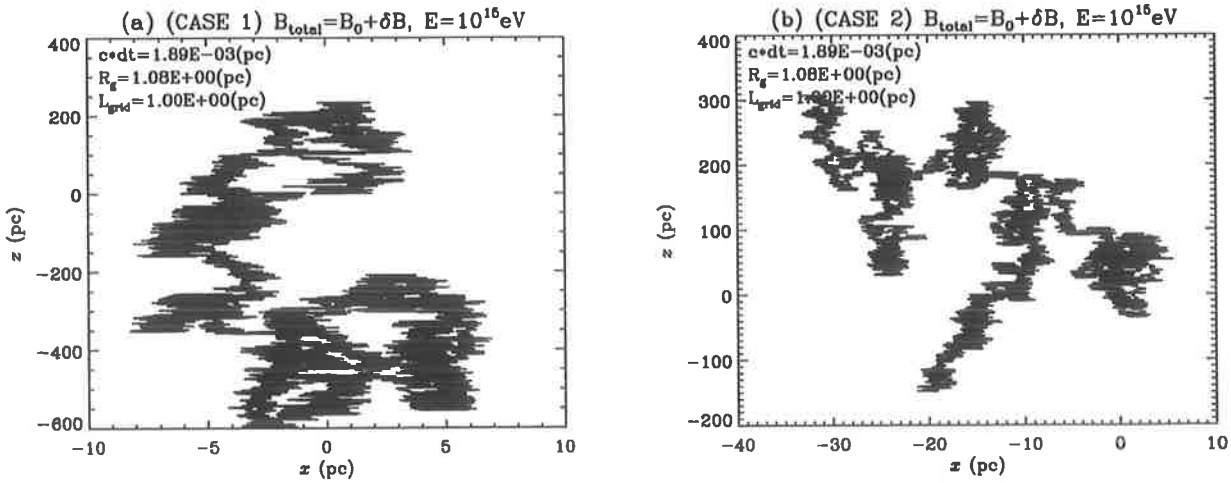

Figure 3.9: (a) (CASE 1) Trajectory of 10^{15}eV proton. (b) (CASE 2) Trajectory of 10^{15}eV proton. The mean magnetic field B_0 is 10^{-10}T and the r.m.s. value of $\delta\vec{B}$ is 10^{-10}T. The grid spacing (=turbulence scale) L_{grid} is 1.0pc.

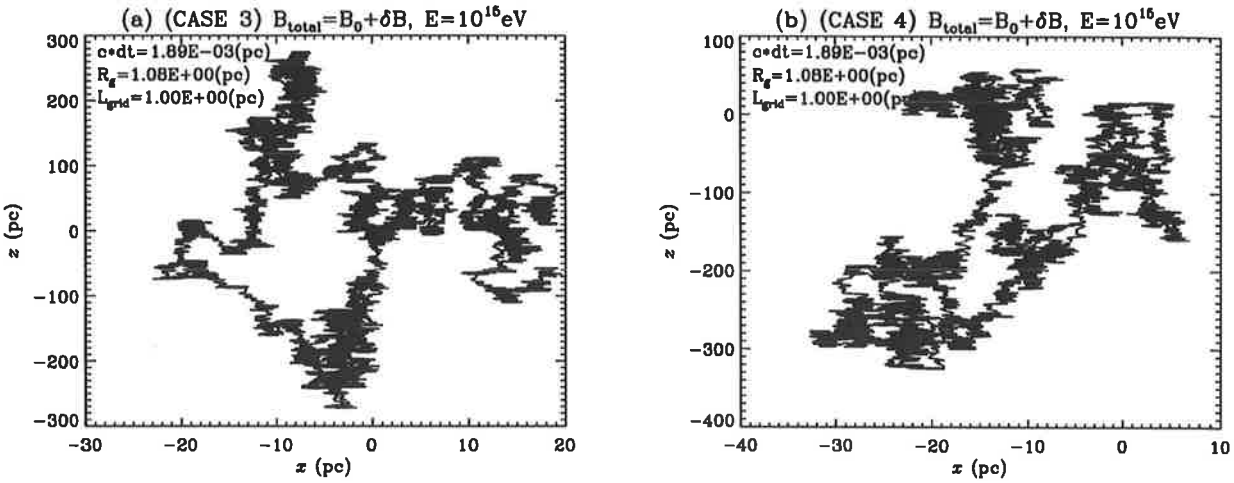

Figure 3.10: (a) (CASE 3) Trajectory of 10^{15}eV proton. (b) (CASE 4) Trajectory of 10^{15}eV proton. The mean magnetic field B_0 is 10^{-10}T and the r.m.s. value of $\delta\vec{B}$ is 10^{-10}T. The grid spacing (=turbulence scale) L_{grid} is 1.0pc.

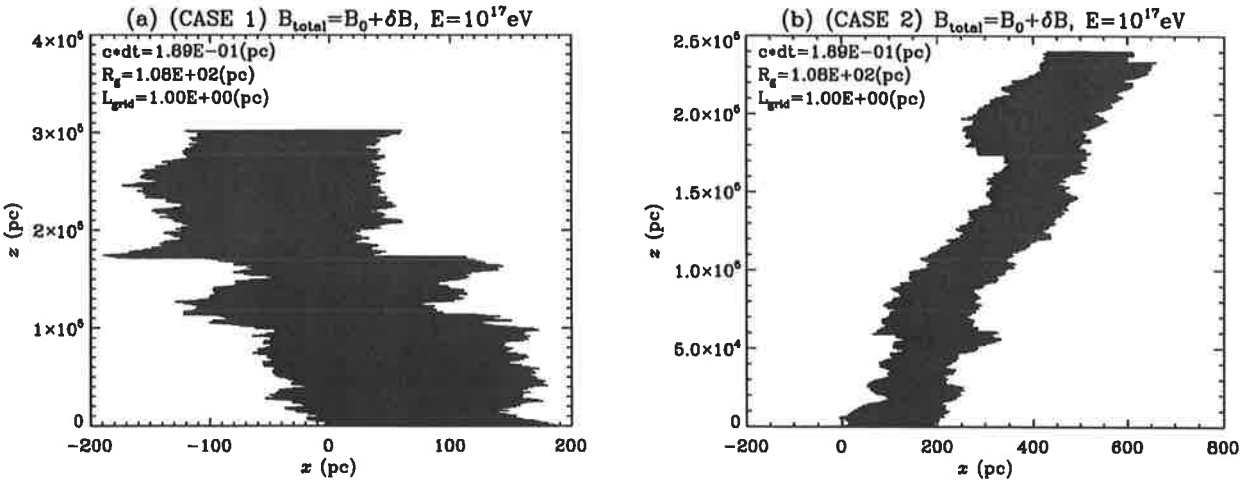

Figure 3.11: (a) (CASE 1) Trajectory of 10^{17}eV proton. (b) (CASE 2) Trajectory of 10^{17}eV proton. The mean magnetic field B_0 is 10^{-10}T and the r.m.s. value of $\delta\vec{B}$ is 10^{-10}T. The grid spacing (=turbulence scale) L_{grid} is 1.0pc.

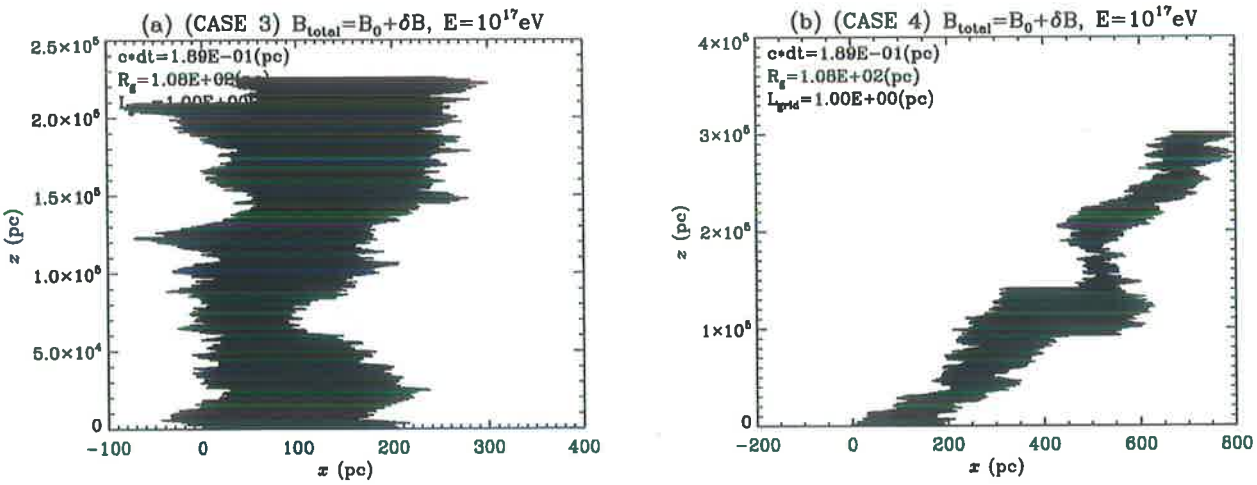

Figure 3.12: (a) (CASE 3) Trajectory of 10^{17}eV proton. (b) (CASE 4) Trajectory of 10^{17}eV proton. The mean magnetic field B_0 is 10^{-10}T and the r.m.s. value of $\delta\vec{B}$ is 10^{-10}T. The grid spacing (=turbulence scale) L_{grid} is 1.0pc.

influenced by structure on small scales magnetic field, whereas in the low energy cases the protons tended to follow the magnetic field lines. Moreover, there seems to be no apparent difference among four cases in Figures 3.11 and 3.12 due to the smaller influence from the magnetic fields (note different scales of x- and z-axis), whereas in the low energy case shown in Figures 3.7 and 3.8, the appearance of the trajectory depends on how the magnetic field is sampled.

3.2.4 Calculation of diffusion tensor ($\vec{B}_{tot} = \delta\vec{B}$)

Section 1.4 explains that the propagation of cosmic rays in turbulent magnetic fields can be described by Equations 1.4.1 and 1.4.3. K_{ij} in Equation 1.4.1 and 1.4.3 is the diffusion tensor, which describes the particle motion in a turbulent flow. Diffusion tensors for cosmic ray proton propagation in turbulent magnetic fields were investigated. First for magnetic fields which consisted only of an irregular magnetic field. The diffusion tensor

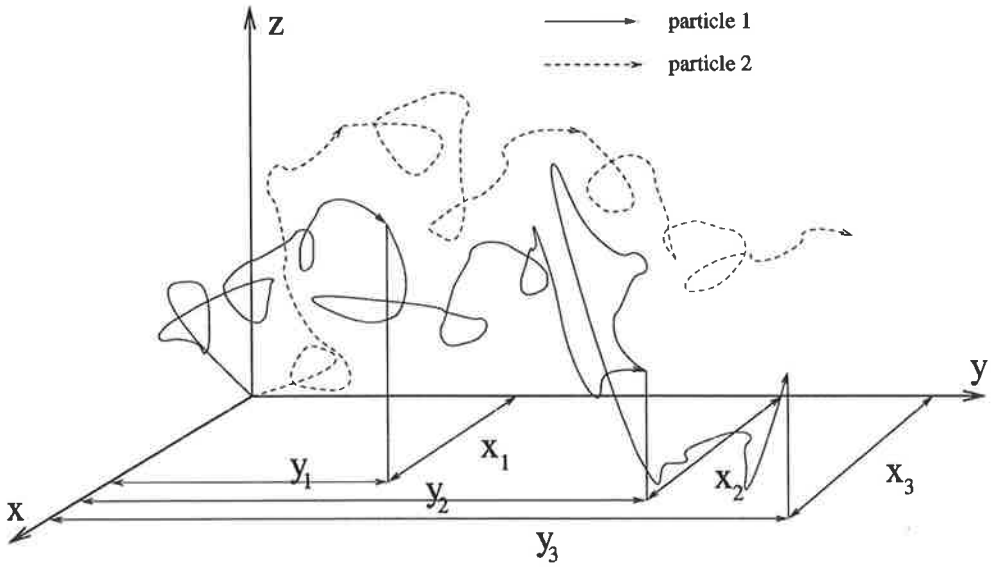

Figure 3.13: Schematic diagram of trajectories and displacements of the particle in the first three steps.

was calculated from the positions of protons at various times. The method of calculation of the diffusion tensors is explained as follows. Figure 3.13 is a schematic diagram of particle trajectories and displacement for the first three time steps. The first particle's displacements for each pre-determined time interval $\triangle t_{\text{interval}}$ are

$$x_1^1,\ x_2^1,\ x_3^1,\ x_4^1,\ \cdots,\ x_{\text{n-intervals}}^1, \tag{3.2.21}$$

where the superscript refers to the particle number and the subscript refers to step number. Then the average squared displacement for each time interval was calculated. The example of the average displacement for each time interval is

$$\langle x_1^2\rangle = \sum_{i=1}^{N} \frac{(x_1^i)^2}{N},\ \langle x_2^2\rangle,\ \langle x_3^2\rangle,\ \cdots,\ \langle x_{\text{n-intervals}}^2\rangle \tag{3.2.22}$$

where N is the number of the particles injected, and N was set to be 1000 in the simulation. The number of steps in the trajectory of each particle was 5×10^6, and the calculation of the average squared displacement was implemented after every $\triangle t_{\text{interval}} = 2 \times 10^4$ time steps. Therefore n-intervals in Equations 3.2.21 and 3.2.22 is $\frac{5\times10^6}{2\times10^4} = 250$.

When the simulation was implemented, the four different cases were compared. The

summary of the four cases is shown in Table 3.3.

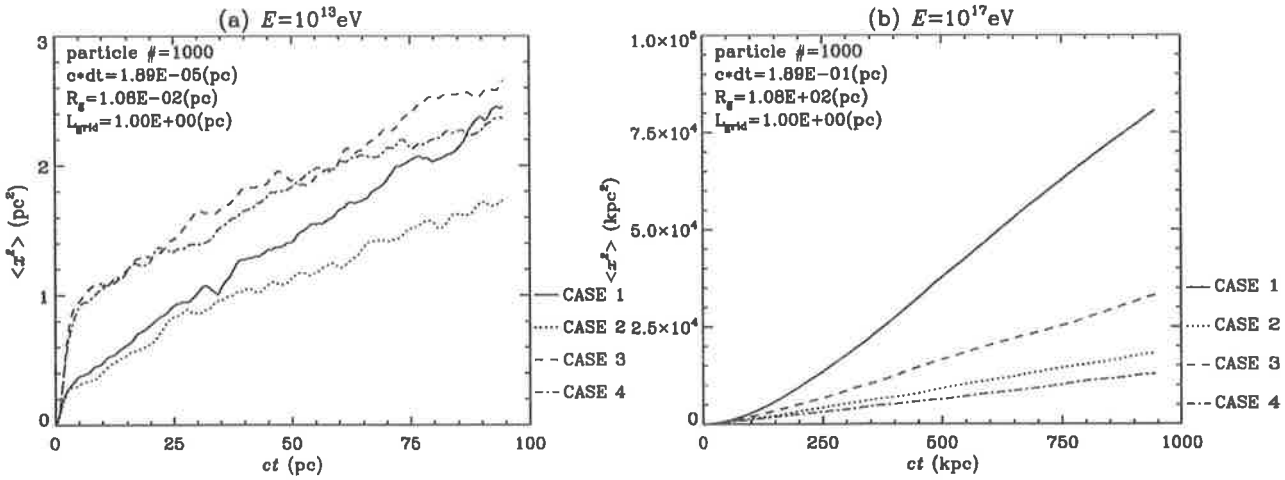

Figure 3.14: $\langle x^2 \rangle$ as a function of time. (a) $E = 10^{13}$eV. (b) $E = 10^{17}$eV. The four cases corresponding to the lines are explained in Table 3.3.

Figure 3.14 shows the x-component of average squared distance $\langle x^2 \rangle$ as a function of time. Figure 3.14 (a) is for 10^{13}eV protons and Figure 3.14 (b) is for 10^{17}eV protons. In Figure 3.14 CASE 1 and CASE 2 plots are steeper than CASE 3 and CASE 4 plots. The difference between CASE 1, 2 and CASE 3, 4 is in the interpolation. In CASE 1 and CASE 2, the magnetic fields inside the cell are interpolated, whereas in CASE 3 and CASE 4, the magnetic fields are not interpolated and the magnetic fields inside the cell are uniform. The difference in the results between interpolation and non-interpolation cases in Figures 3.14 (a) are clearly caused by differences in the interpolation method. At low energies, in the non-interpolation case particles quickly travel across a cell having uniform field, while for non-uniform $\vec{B}$ it takes longer to cross a cell.

Figure 3.15 is the schematic diagram of the magnetic field distribution in x-direction for an extreme case. The dots in the upper diagrams of Figure 3.15 indicate the magnetic field in the x-direction at grid points and the solid lines in the upper diagrams of Figure

3.15 show the magnetic field that would be used in a simulation. The lower diagrams of Figure 3.15 show $|\delta\vec{B}^2|$. If magnetic field interpolation is not implemented inside the cell, the value of the magnetic field is the same everywhere inside the cell as shown in the upper diagrams of Figure 3.15 (a). As a result, in this extreme example the mean square value of the magnetic field $\langle\delta\vec{B}^2\rangle$ becomes 1 as shown in lower diagram of Figure 3.15 (a). On the other hand, if magnetic field interpolation is implemented inside the cell, as shown in the upper diagram of Figure 3.15 (b), the mean square value of the magnetic field $\langle\delta\vec{B}^2\rangle$ becomes 1/3. Even though the fields were sampled such that they should have the same $\langle\delta B^2\rangle$, in practice, differences in $\langle\delta B^2\rangle$ between the interpolation and non-interpolation cases arise. This r.m.s. value difference may cause the difference between CASE 1, 2 and CASE 3, 4 in Figure 3.14. Therefore, it might make sense for the magnetic fields in CASE 1 and CASE 2 to be normalized by the root mean square value of the magnetic fields $|\delta\vec{B}_{rms}|$, so that the average values of the magnetic fields will become 1, and then hopefully the plots in CASE 1 and CASE 2 could become consistent with those of CASE 3 and CASE 4.

Figure 3.16 is the plots of $\langle x^2\rangle$ as a function of time where CASE 1 and CASE 2 magnetic fields in Figure 3.16 are normalised by the r.m.s. value $|\delta\vec{B}_{rms}|$. The normalized CASE 1 and CASE 2 curves in Figure 3.16 become lower than the CASE 1 and CASE 2 curves in Figure 3.14. As a result, the normalized CASE 1 and CASE 2 curves in Figure 3.16 (a) become lower than CASE 3 and CASE 4. On the other hand, the CASE 1 and CASE 2 curves in Figure 3.16 (b) become close to the CASE 3 and CASE 4 curves, but the CASE 1 and CASE 2 curves are still not consistent with the CASE 3 and CASE 4 curves. Therefore, normalization after implementing interpolation was not used in the simulation.

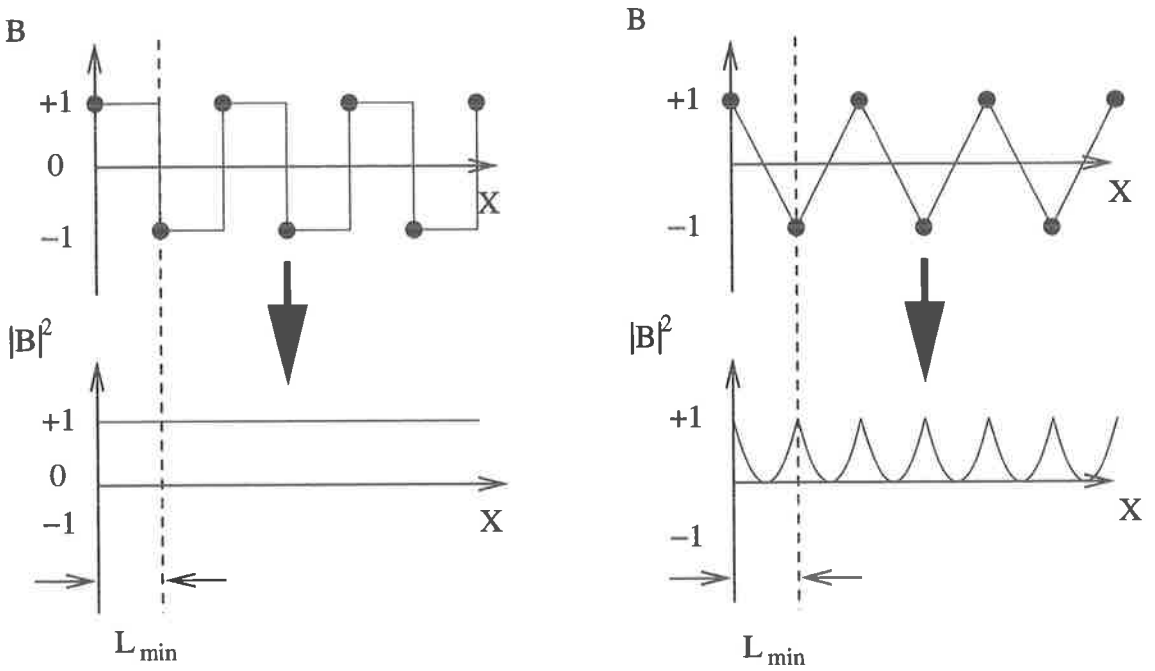

Figure 3.15: The schematic diagram of the magnetic field distribution (upper diagrams) and the squared magnetic field distribution (lower diagrams). (a) No interpolation case. (b) Interpolation case.

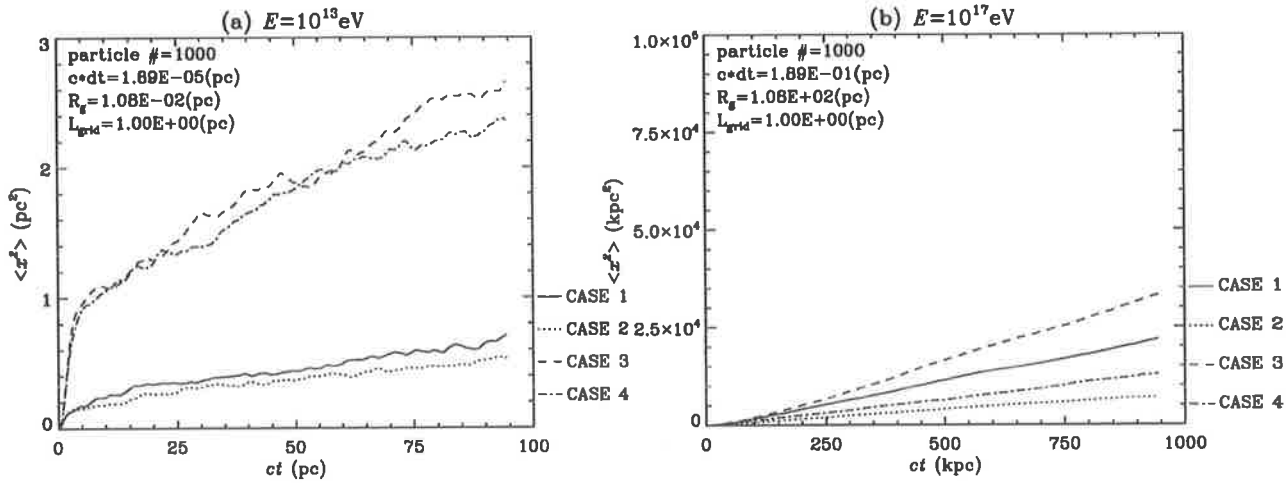

Figure 3.16: $\langle x^2 \rangle$ as a function of time. (a)$E = 10^{13}$eV. (b) $E = 10^{17}$eV. The magnetic fields in CASE 1 and CASE 2 are normalised by the r.m.s. value $|\delta \vec{B}_{rms}|$.

The diffusion coefficient K_x was calculated from Equation 3.2.23,

$$K_x = \frac{1}{2}\frac{\langle x^2 \rangle}{t}. \tag{3.2.23}$$

The least squares fitting method was applied to the calculation of $\frac{\langle x^2 \rangle}{t}$ in the simulation. The values of the diffusion coefficients can be estimated from the appearance of the proton's trajectory using Random Walk Theory. For higher energy, the gyroradius becomes larger than the grid spacing ($R_g \gg L$).

Figure 3.17 shows the schematic diagram of the trajectory of a proton with a high energy inside the cell. In Figure 3.17 (a), the change in angle $\delta\theta$ is approximately

$$\delta\theta \approx \frac{L}{R_g} \tag{3.2.24}$$

where R_g is proton's gyroradius and L is the minimum grid spacing of the lattice. After the proton propagates through N cells, the final scattering angle in Figure 3.17 (b) is

$$\theta_N^2 \approx N(\delta\theta)^2 \tag{3.2.25}$$

For one scattering mean free path, the final angle needs to be $\theta_N \approx \pi$. From Equations 3.2.24 and 3.2.25,

$$\begin{aligned} N(\delta\theta)^2 &\approx \pi^2 \\ N\Big(\frac{L}{R_g}\Big)^2 &\approx \pi^2 \\ \therefore N &\approx \pi^2\Big(\frac{R_g}{L}\Big)^2 \end{aligned} \tag{3.2.26}$$

Therefore, the proton's mean free path λ_{scatt} becomes approximately,

$$\lambda_{scatt} \approx NL \approx \frac{(\pi R_g)^2}{L}. \tag{3.2.27}$$

Using Equation 3.2.27 and Quasi-linear approximation $K \approx \frac{1}{3}\lambda_{scatt} v$, the diffusion coefficient for higher energy protons K_{high} becomes

$$K_{high} \approx \frac{1}{3}\lambda_{scatt} v \sim \Big(\frac{R_g^2}{L}\Big)v. \tag{3.2.28}$$

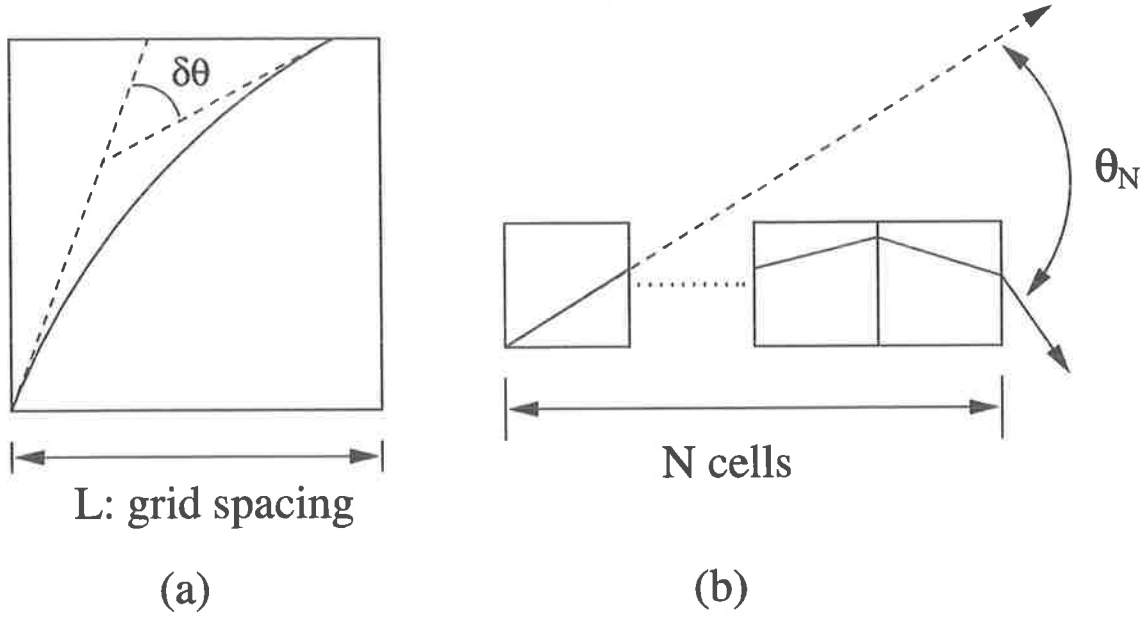

Figure 3.17: Schematic diagram of trajectory of a high energy proton. (a) Trajectory in one cell. $\delta\theta$ is a change in angle per one cell scattering. (b) Trajectory in N cells. θ_N is the final angle with respect to the initial proton direction after N-cell scattering.

We shall next consider the case of low energies where the gyroradius becomes smaller than the grid spacing ($R_g \ll L$). Figure 3.18 shows the schematic diagram of trajectory of a proton with low energy inside the cell. The mean squared distance of proton after it propagates through N cells is

$$\langle z^2 \rangle \approx NL^2 \tag{3.2.29}$$

$$\therefore \sqrt{\langle z^2 \rangle} \approx \sqrt{N}L \tag{3.2.30}$$

From Equation 3.1.2,

$$\langle z^2 \rangle \approx Kt. \tag{3.2.31}$$

The time for crossing N cells t is

$$t \approx \frac{NL}{v} \qquad \therefore N \approx \frac{vt}{L}. \tag{3.2.32}$$

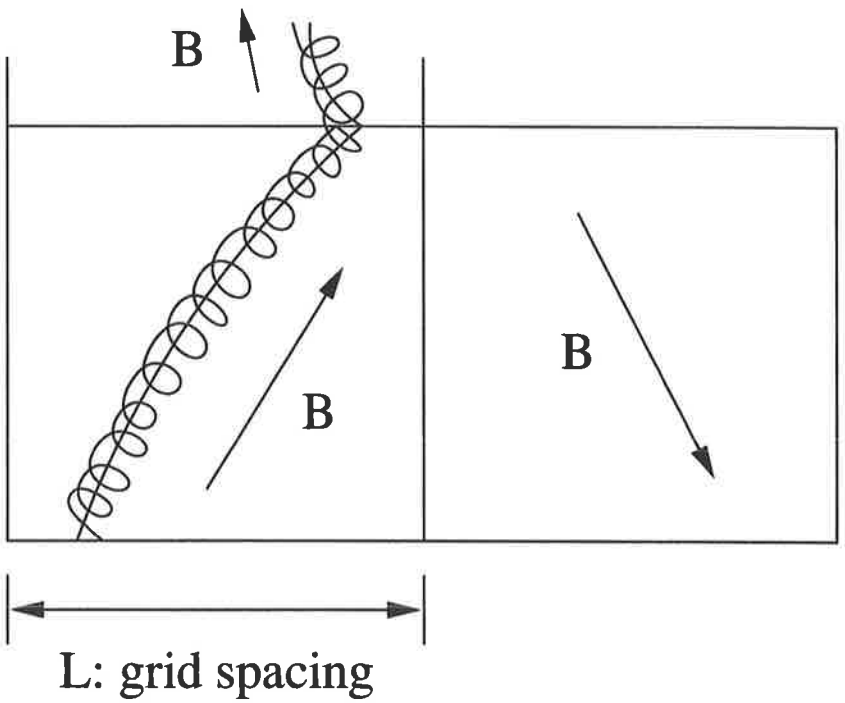

Figure 3.18: Schematic diagram of trajectory of a low energy proton. The gyroradius for a low energy proton is smaller than a grid spacing.

From Equations 3.2.29, 3.2.31 and 3.2.32, the diffusion coefficient for low energy protons K_{low} approximately becomes

$$\begin{aligned} \langle z^2 \rangle &\approx NL^2 \approx \frac{vtL^2}{L} \sim vtL \\ &\therefore K_{low} \approx Lv \end{aligned} \tag{3.2.33}$$

In the simulation, the grid spacing is $\frac{1\text{pc}}{32} \approx 0.03\text{pc}$ and $v \approx c = 10^{-8}\text{pc/s}$. For protons with $E = 10^{17}\text{eV}$, the gyroradius is $\sim$ 100pc, and using Equation 3.2.28, the diffusion coefficient would be

$$\begin{aligned} K_{high} &\approx \left(\frac{R_g^2}{L}\right) v = \frac{100^2}{0.03} \times 10^{-8} \\ &\approx 10^{-3}\ \text{pc}^2/\text{s}. \end{aligned} \tag{3.2.34}$$

For a proton with $E = 10^{13}\text{eV}$, the gyroradius is $\sim$ 0.01pc, and using Equation 3.2.33, the

diffusion coefficient would be

$$\begin{aligned} K_{low} &\approx Lv = 0.03 \times 10^{-8} \\ &\approx 10^{-10}\ \mathrm{pc}^2/\mathrm{s}. \end{aligned} \tag{3.2.35}$$

	$E = 10^{13}$eV	$E = 10^{17}$eV
	K_x [pc^2/sec]	K_x [pc^2/sec]
(CASE 1)	1.11×10^{-10}	4.51×10^{-4}
(CASE 2)	7.64×10^{-11}	9.72×10^{-5}
(CASE 3)	9.71×10^{-11}	1.78×10^{-4}
(CASE 4)	8.49×10^{-11}	6.78×10^{-5}

Table 3.4: The diffusion tensor components for four cases of the simulation. K_x represents x-component of diffusion tensor. The total magnetic field is $\vec{B}_{total} = \delta\vec{B}$ and is isotropic.

Table 3.4 describes the values of 10^{13}eV and 10^{17}eV diffusion coefficient in four cases. The diffusion tensors of 10^{13}eV protons are approximately 10^{-10} pc^2/s, which is reasonably close to the approximation expressed by Equation 3.2.35. However the diffusion coefficients of 10^{17}eV protons are smaller than the approximation 3.2.34. The diffusion coefficient value of CASE 1 is the closest value of the four cases. Therefore the CASE 1 simulation will be better to use to obtain precise values of diffusion coefficient.

3.2.5 Calculation of diffusion tensor ($\vec{B}_{tot} = B_0\hat{e}_z + \delta\vec{B}$)

In Honda's simulation, the turbulent magnetic fields were composed of irregular plus uniform magnetic fields. In this section the diffusion tensors in the magnetic field composed of the two kinds of magnetic fields are investigated. Figures 3.19 to 3.21 are the plots of $\langle z^2 \rangle$ and $\langle x^2 + y^2 \rangle$ as a function of time. Honda introduced the turbulence level f^H_{turb} to

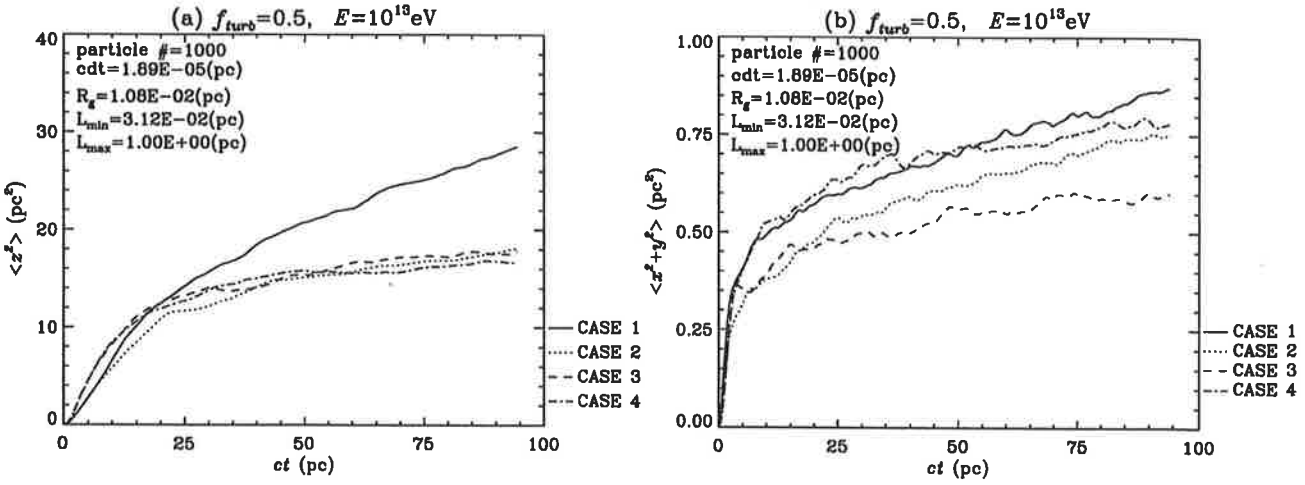

Figure 3.19: (a) $\langle z^2 \rangle$ as a function of time. (b) $\langle x^2 + y^2 \rangle$ as a function of time. The turbulence level is $f^H_{turb} = 0.5$ and the proton's energy is $E = 10^{13}$eV. The four cases corresponding to the lines are explained in Table 3.3.

explain how the diffusion tensor depends on the magnetic turbulence. The turbulence level f^H_{turb} is

$$f^H_{turb} = \frac{|\delta B_{rms}|}{B_0}. \tag{3.2.36}$$

Equation 3.2.36 describes how much the irregular magnetic field $\delta\vec{B}$ is related to the total magnetic field $\vec{B}_{total}$. If $f^H_{turb} \ll 1$, $\delta\vec{B}$ dominates the total magnetic field $\vec{B}_{total}$ and $\vec{B}_{total}$ becomes more isotropic.

In Figure 3.19 the turbulence level is $f^H_{turb} = 0.5$ and the proton's energy is $E = 10^{13}$eV. In Figure 3.20 $f^H_{turb} = 0.5$ and $E = 10^{15}$eV, and in Figure 3.21 $f^H_{turb} = 0.5$ and $E = 10^{17}$eV. The four cases corresponding to the lines are explained in Table 3.3.

Figure 3.19 suggests that two regimes exit in 10^{13}eV proton diffusion; the linear regime and the diffusive regime. Figure 3.19 (a) shows the slopes of plots changes at about $ct = 20$pc and the slopes at $ct < 20$pc are steeper than those at $ct > 20$pc. This may imply that the low energy protons ($E = 10^{13}$eV) tend to propagate linearly in the turbulent

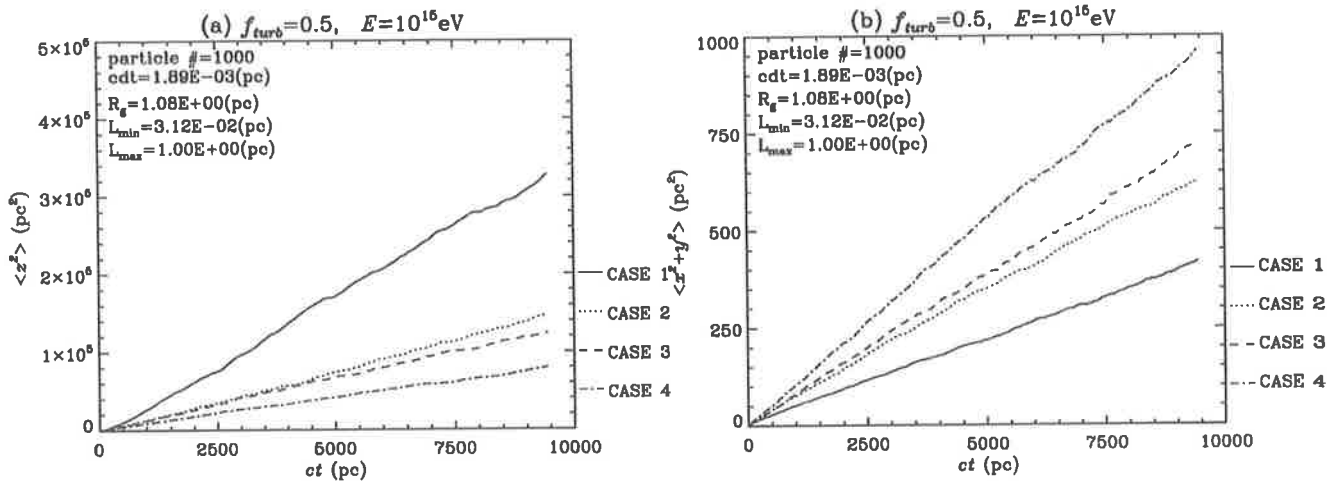

Figure 3.20: (a) $\langle z^2 \rangle$ as a function of time. (b) $\langle x^2 + y^2 \rangle$ as a function of time. The turbulence level is $f_{turb}^{H} = 0.5$ and the proton's energy is $E = 10^{15}$eV. The four cases corresponding to the lines are explained in Table 3.3.

magnetic fields, but do not have enough energy to overcome the influence of the magnetic fields at $ct > 20$pc. Figure 3.19 (b) shows that the slope changes at about $ct = 5$pc, and that the slopes at $ct < 5$pc are steeper than those at $ct > 5$pc. The plots are very close to the straight lines at $ct < 5$pc, whereas the plots are wobbling at $ct > 5$pc, possibly be due to circular motion in the xy-plane. Therefore, it may be concluded that the turbulent magnetic field has less effect on the propagation of low energy protons in the linear regime, but that the influence of the turbulent magnetic fields become larger and so the magnetic fields dominate the propagation in the diffusion regime.

On the other hand, two distinctive regimes, such as the linear regime and the diffusion regime in Figure 3.19 (10^{13}eV), are not observed in the curves in Figures 3.20 and 3.21. The gyroradius of a 10^{15}eV proton for $B_0 = 10^{-10}$T is $\sim$ 1.0pc, and is comparable to L_{grid}. The gyroradius of a 10^{17}eV proton for $B_0 = 10^{-10}$T is $\sim$ 100pc. In Figure 3.21 (a), for diffusion parallel to $\vec{B}_0$ all four curves are close each other, whereas the four curves in

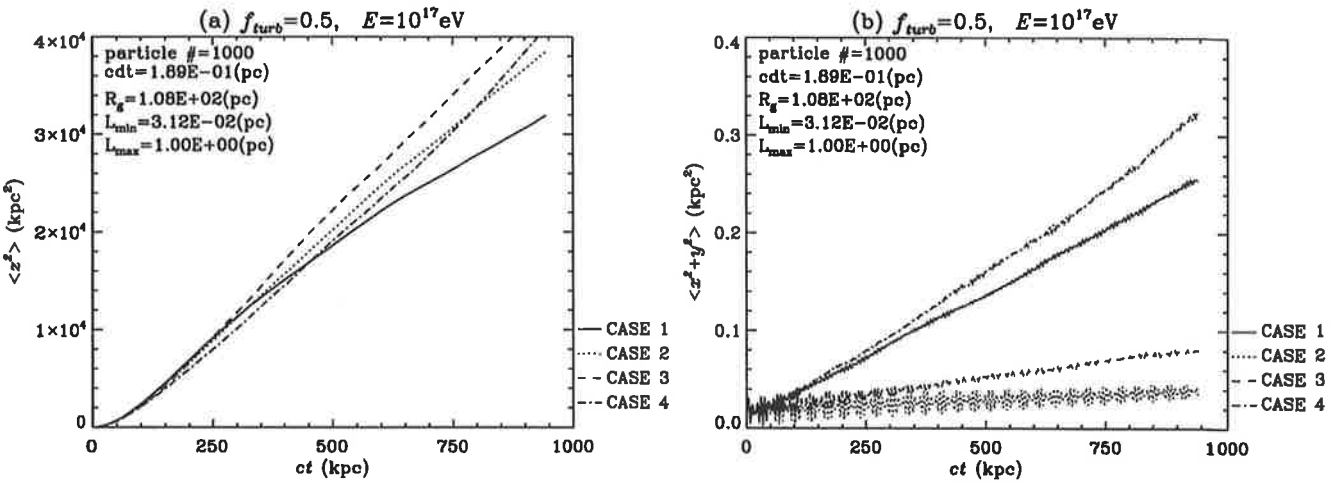

Figure 3.21: (a) $\langle z^2 \rangle$ as a function of time. (b) $\langle x^2 + y^2 \rangle$ as a function of time. The turbulence level is $f_{turb}^{H} = 0.5$ and the proton's energy is $E = 10^{17}$eV. The four cases corresponding to the lines are explained in Table 3.3.

Figure 3.21 (b) for diffusion perpendicular to $\vec{B}_0$ are not consonant with each other.

The parallel and perpendicular diffusion coefficients were calculated from the plots of average displacements $\langle z^2 \rangle$ and $\langle x^2 + y^2 \rangle$ as a function of time shown in Figures 3.19 and 3.21. To calculate the slope for $\langle z^2 \rangle$ vs. time and $\langle x^2 + y^2 \rangle$ vs. time curves, the least squares method was used. Then using Equations 3.1.2 and 3.1.3, the parallel component of the diffusion tensor $K_{\parallel}$ and the perpendicular component of the diffusion tensor $K_{\perp}$ were calculated. Note that these are the relations for the case where the mean magnetic fields exist in z-direction, and so $K_{\parallel}$ and $K_{\perp}$ are referred to the diffusion parallel and perpendicular to z-direction, respectively.

Table 3.5 shows the values of $K_{\parallel}$ and $K_{\perp}$ for four different methods of creating magnetic fields. The values of $K_{\parallel}$ is larger than $K_{\perp}$ because f_{turb}^{H} is 0.5, which means the mean magnetic field B_0 dominates the total magnetic field B_{total}. Therefore the values of $K_{\parallel}$ is close to the approximation expressed in Equations 3.2.34 and 3.2.35.

	$E = 10^{13}$eV		$E = 10^{17}$eV	
	$K_{\parallel}$ [pc^2/sec]	$K_{\perp}$ [pc^2/sec]	$K_{\parallel}$ [pc^2/sec]	$K_{\perp}$ [pc^2/sec]
(CASE 1)	1.30×10^{-9}	1.18×10^{-11}	1.72×10^{-4}	5.43×10^{-11}
(CASE 2)	7.26×10^{-10}	1.22×10^{-11}	2.09×10^{-4}	6.33×10^{-10}
(CASE 3)	6.25×10^{-10}	6.97×10^{-12}	2.36×10^{-4}	1.67×10^{-10}
(CASE 4)	5.53×10^{-10}	9.70×10^{-12}	2.15×10^{-4}	7.97×10^{-10}

Table 3.5: The diffusion tensor components for four cases of the simulation. $K_{\parallel}$ represents diffusion coefficient parallel to the mean magnetic field. $K_{\perp}$ represents diffusion coefficient perpendicular to the mean magnetic field.

The analysis and discussion of diffusion tensors were carried out for Kolmogorov-type turbulent magnetic field.

3.3 Repeating Honda's method with a Kolmogorov spectrum

Section 3.2 describes how to calculate the trajectories of protons and the diffusion tensors in a single grid space magnetic field model. In this section I explain how to produce a Kolmogorov-type turbulent magnetic field, and discusses cosmic ray diffusion simulation in this field.

3.3.1 Repeating Kolmogorov magnetic fields

This section presents the method to create a Kolmogorov-like magnetic field. Firstly, the lattice space is set with different grid spacing. The largest is L_{max}, and the next largest is

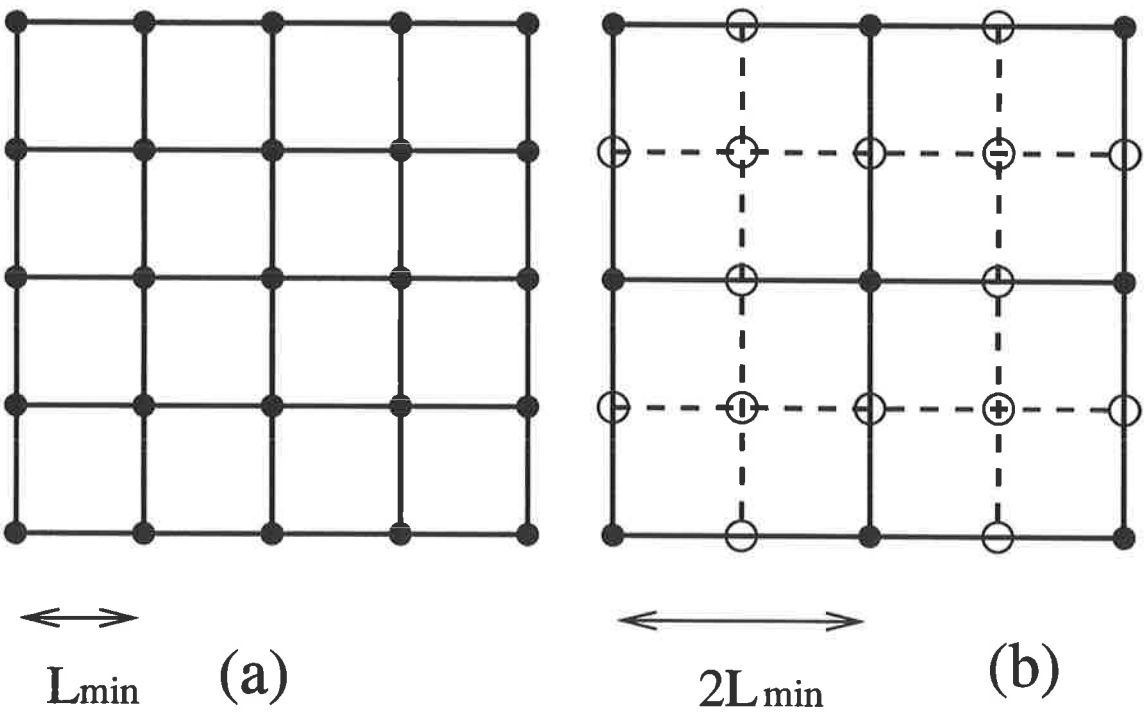

Figure 3.22: Two-dimensional diagram showing two different lattice spacings. The filled circles in the diagram are calculated magnetic fields. (a) The smallest grid spacing. (b) The next larger grid spacing. The open circles indicate where no magnetic fields are initially calculated. but will be interpolated from the magnetic fields at surrounding points.

$L_{max}/2$. This routine is repeated n times until grid space becomes L_{min}, ie,

$$L_{max} = \frac{L_{max}}{2^0}, \frac{L_{max}}{2^1}, \frac{L_{max}}{2^2}, \frac{L_{max}}{2^3}, \cdots, \frac{L_{max}}{2^n} = L_{min} \tag{3.3.1}$$

Figure 3.22 shows the two-dimensional diagram for just two different lattice spaces. The magnetic fields are placed at each grid point for each of the different lattice spacings. Figure 3.22 also shows how the magnetic fields among the grid points are interpolated. The root mean square (r.m.s.) value of magnetic fields for larger grid spacing should be larger than that of the smaller grid spacing. Honda [11] introduced a Lattice Constant to determine the r.m.s. value of magnetic fields for different grid spacings. The magnetic fields for different grid spacings were then added vectorially to create a Kolmogorov type turbulent magnetic field. According to Honda's simulation [11], the lattice constant which governs the magnitude of the irregular magnetic field for different grid spacings is

$$L_i^{5/3} = \left(\frac{L_0}{10^{i/2}}\right)^{5/3}, \qquad (i = 1, 2, 3, \cdots) \tag{3.3.2}$$

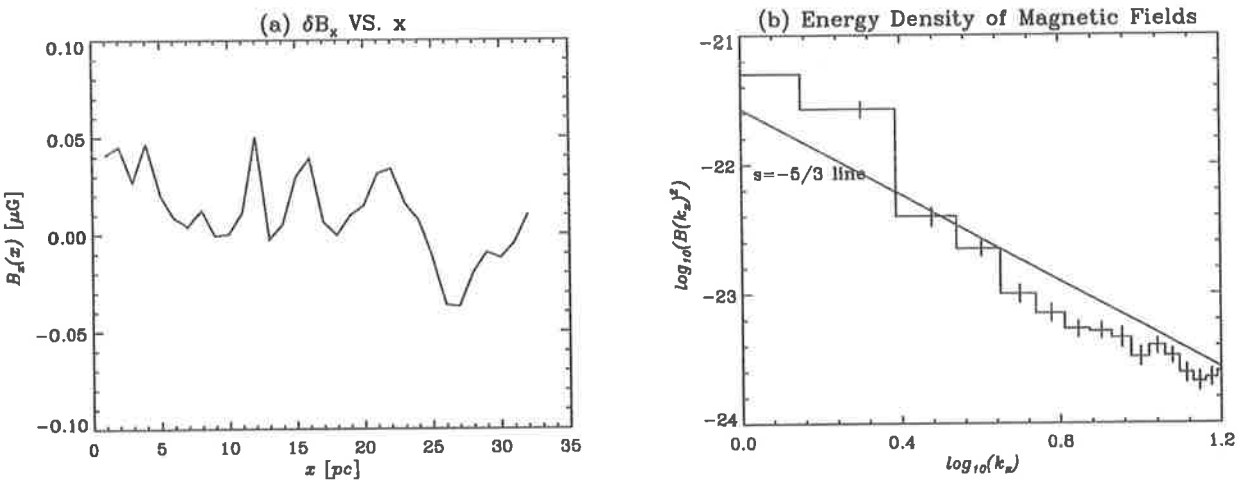

Figure 3.23: (a) Strength of irregular magnetic fields along the x-direction. (b) Average energy density of irregular magnetic fields on logarithmic scale. The solid line is $-5/3$ line. The results were obtained when Equation 3.3.3 was applied.

where L_0 is the maximum grid spacing, and corresponds to the scale of irregularity. However, since the grid spacing is reduced by the factor of 2 in the simulation, the lattice constant becomes,

$$L_i^{5/3} = \left(\frac{L_0}{2^{i/2}}\right)^{5/3}, \qquad (i = 1, 2, 3, \cdots) \tag{3.3.3}$$

Figure 3.23 (a) shows that the magnitude of the magnetic field and Figure 3.23 (b) shows the average energy density of the magnetic field $|B_x(k_x)|^2$ along the x-direction, when the lattice constant 3.3.3 is applied. The plots of spectrum $|B_x(k_x)|^2$ were created by using the Discrete Fourier Transform (DFT) algorithm. The simulation was run 100 times using different random numbers and average and standard errors (error bars) were calculated. For Kolmogorov turbulence, the spectrum of the magnetic fields must follow the $-5/3$ line. However, the slope of the spectrum is steeper than the $-5/3$ line (solid line) shown in Figure 3.23 (b).

Stanev et al. [24] discussed the spectrum of turbulent magnetic fields and proposed a

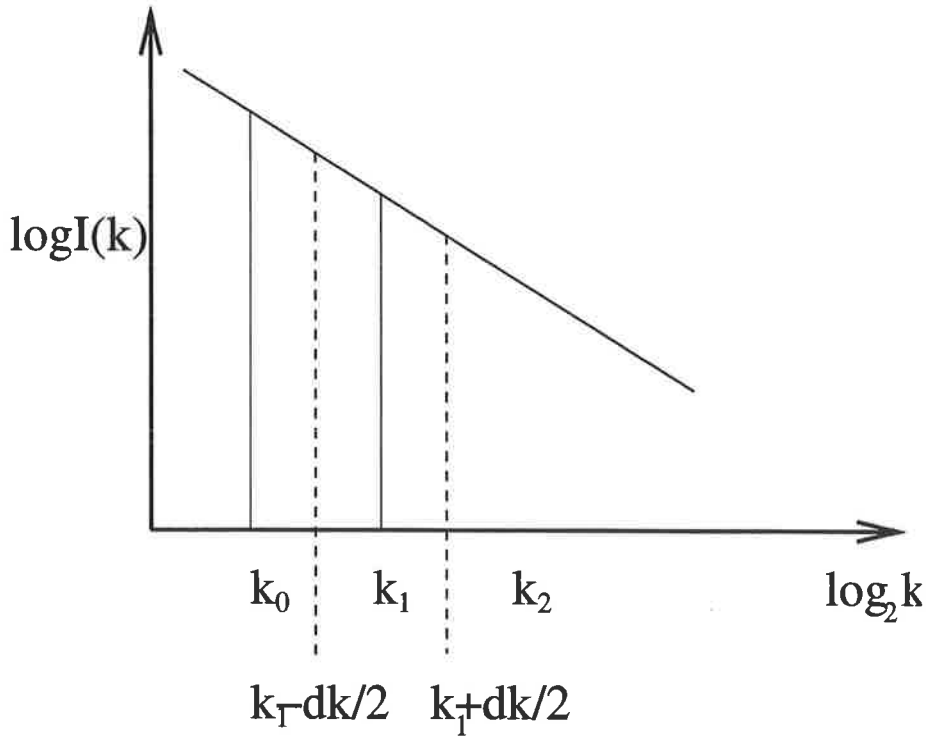

Figure 3.24: The schematic diagram of the energy density $I(k)$ in k-space (k: wavenumber).

new lattice constant. By definition, a Kolmogorov spectrum is

$$I(k) = I_0\Big(\frac{k}{k_0}\Big)^{-5/3}, \tag{3.3.4}$$

where k is wavenumber, and $I(k)$ is the energy density of the magnetic field per unit wavenumber k. k_0 is the smallest wavenumber and corresponds to the largest turbulence scale or irregularity. Because they were considering a limited range of energies, to simplify the problem, they used just three wavenumbers from k_0 to k_2, ie $k_i = 2^i k_0$, $(i = 0, 1, 2)$. Figure 3.24 shows the schematic diagram of the energy density for wavenumbers from k_0 to k_2. The space between two adjoining wavenumbers is 1 in $\log_2 k$ scale. Therefore, the energy density for i-th wavenumber is

$$U_i = \int_{k_i-\triangle k/2}^{k_i+\triangle k/2} I(k)dk \approx \frac{I(k)dk}{d(\log_2 k)}\Delta(\log_2 k). \tag{3.3.5}$$

Since

$$\frac{d(\log_2 k)}{dk} = \frac{1}{k \ln 2} \tag{3.3.6}$$

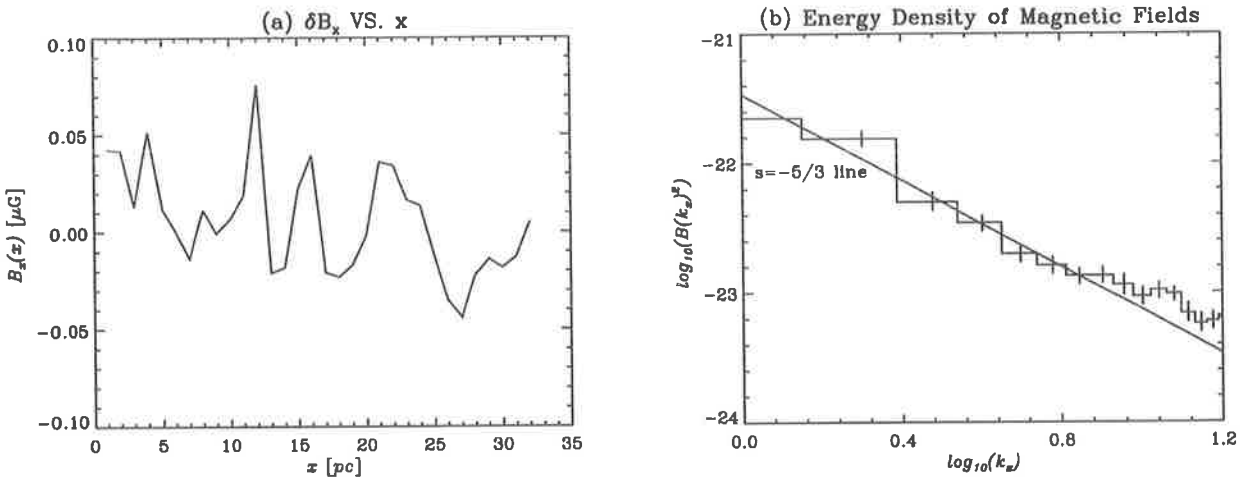

Figure 3.25: (a) Strength of irregular magnetic fields along the x-direction. (b) Average energy density of irregular magnetic fields on logarithmic scale. The solid line is $-5/3$ line. The results were obtained when Equation 3.3.9 was applied.

Equation 3.3.5 becomes

$$\begin{aligned}\frac{I(k)dk}{d(\log_2 k)}\Delta(\log_2 k) &= I_0\Big(\frac{k}{k_0}\Big)^{-5/3} k\ln 2 \\ &= I_0 k_0 \ln 2\Big(\frac{k}{k_0}\Big)^{-2/3}\end{aligned} \tag{3.3.7}$$

Therefore, the lattice constant is proportional to $k^{-2/3}$, ie,

$$\text{Lattice Constant} \propto k^{-2/3} \propto L^{2/3} \tag{3.3.8}$$

where L is grid spacing. Finally, the lattice constant chosen was

$$L_i^{2/3} = \Big(\frac{L_0}{2^{i/2}}\Big)^{2/3}, \qquad (i = 1, 2, 3, \cdots) \tag{3.3.9}$$

Figure 3.25 (a) shows the strength of the magnetic fields along x-direction and Figure 3.25 (b) shows their spectrum when the final lattice constant was applied. The solid line in Figure 3.25 (b) is the $-5/3$ line. Figure 3.25 (b) shows that the energy density spectrum $|B(k_x)|^2$ is consistent with $-5/3$ line. This concludes that the Kolmogorov magnetic field can be created if the r.m.s. value of the magnetic field $\delta\vec{B}$ is proportional to Equation 3.3.9.

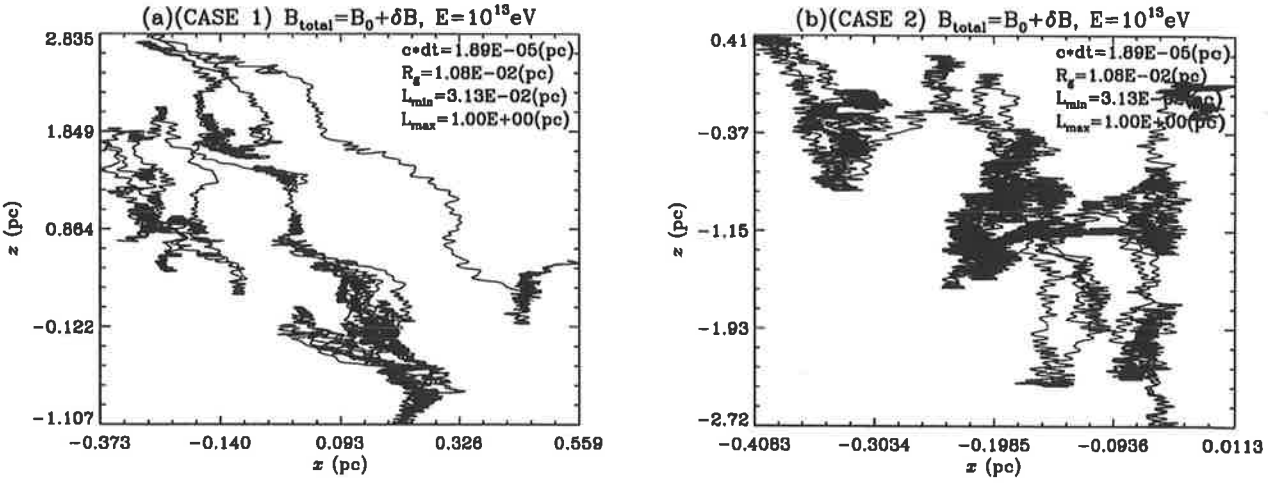

Figure 3.26: (a) (CASE 1) Trajectory of 10^{13}eV proton. (b) (CASE 2) Trajectory of 10^{13}eV proton. The mean magnetic field B_0 is 10^{-10}T and the r.m.s. value of $\delta\vec{B}$ is 0.5×10^{-10}T. The maximum grid spacing (=turbulence scale) L_{max} is 1.0pc.

In the next section I will discuss proton trajectories when Kolmogorov-type magnetic fields are applied in the simulation.

3.3.2 Trajectories of charged particles (Kolmogorov magnetic fields)

After producing Kolmogorov-like magnetic fields, the simulation injects 1000 protons into the magnetic fields to calculate the positions of the protons at various times. This section discuss the proton trajectories.

The initial values of the particles and magnetic fields are the same as Table 3.2, so that the results can be compared with the trajectories in the single grid spacing case. The calculation of the protons' positions is described in Section 3.2.3. When the simulation was implemented, the four different cases were compared. The summary of the four cases was shown in Table 3.3 in Section 3.2.3.

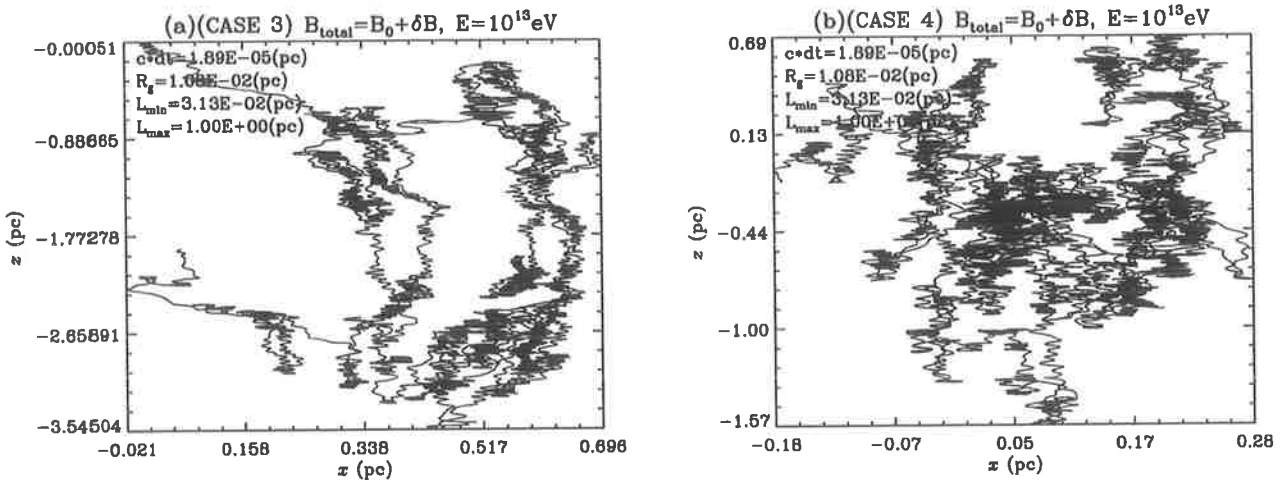

Figure 3.27: (a) (CASE 3) Trajectory of 10^{13}eV proton. (b) (CASE 4) Trajectory of 10^{13}eV proton. The mean magnetic field B_0 is 10^{-10}T and the r.m.s. value of $\delta\vec{B}$ is 0.5×10^{-10}T. The maximum grid spacing (=turbulence scale) L_{max} is 1.0pc.

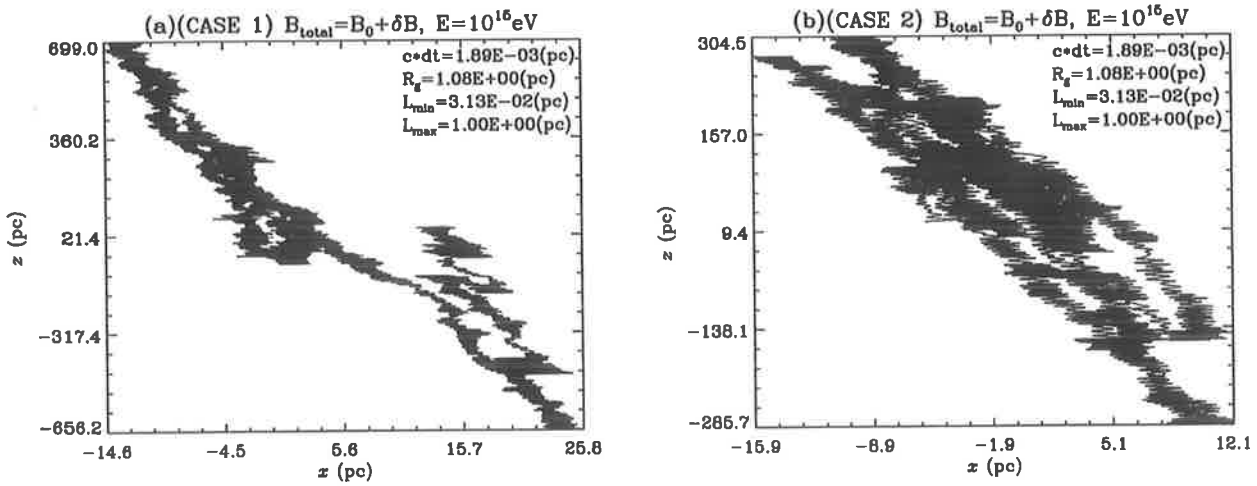

Figure 3.28: (a) (CASE 1) Trajectory of 10^{15}eV proton. (b) (CASE 2) Trajectory of 10^{15}eV proton. The mean magnetic field B_0 is 10^{-10}T and the r.m.s. value of $\delta\vec{B}$ is 0.5×10^{-10}T. The maximum grid spacing (=turbulence scale) L_{max} is 1.0pc.

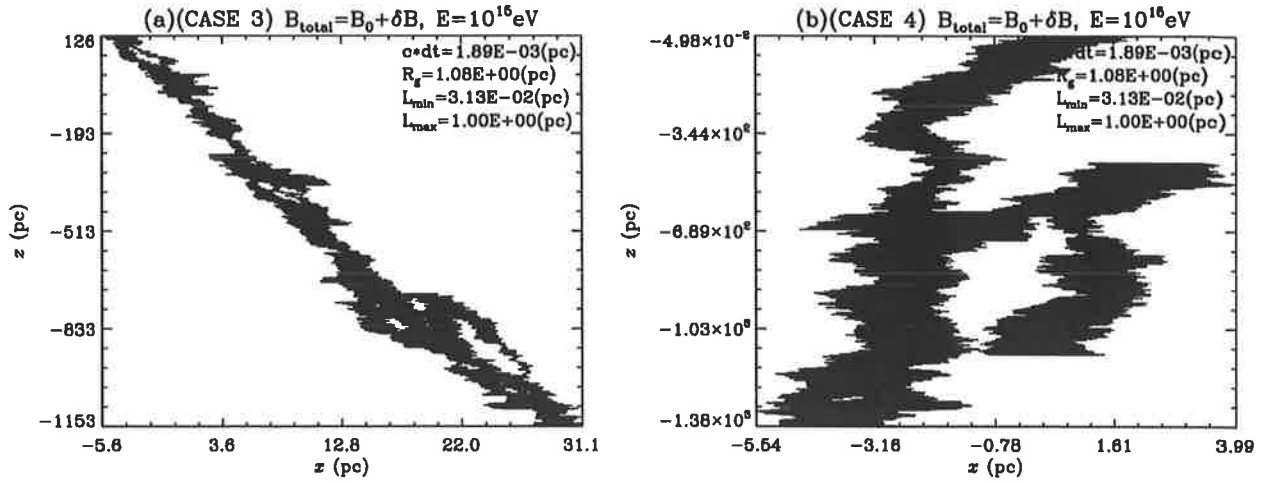

Figure 3.29: (a) (CASE 3) Trajectory of 10^{15}eV proton. (b) (CASE 4) Trajectory of 10^{15}eV proton. The mean magnetic field B_0 is 10^{-10}T and the r.m.s. value of $\delta\vec{B}$ is 0.5×10^{-10}T. The maximum grid spacing (=turbulence scale) L_{max} is 1.0pc.

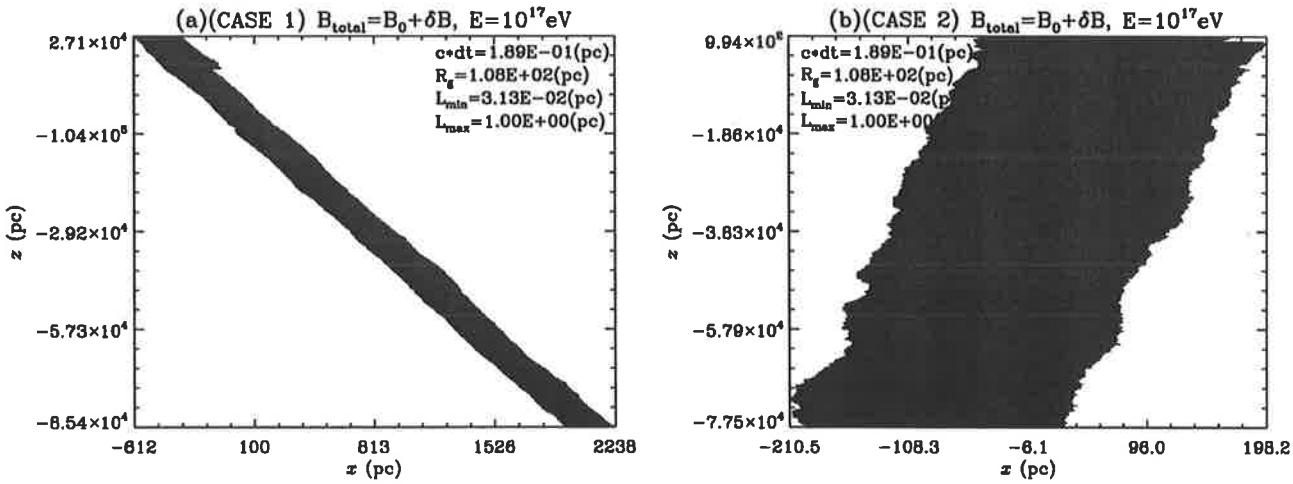

Figure 3.30: (a) (CASE 1) Trajectory of 10^{17}eV proton. (b) (CASE 2) Trajectory of 10^{17}eV proton. The mean magnetic field B_0 is 10^{-10}T and the r.m.s. value of $\delta\vec{B}$ is 0.5×10^{-10}T. The maximum grid spacing (=turbulence scale) L_{max} is 1.0pc.

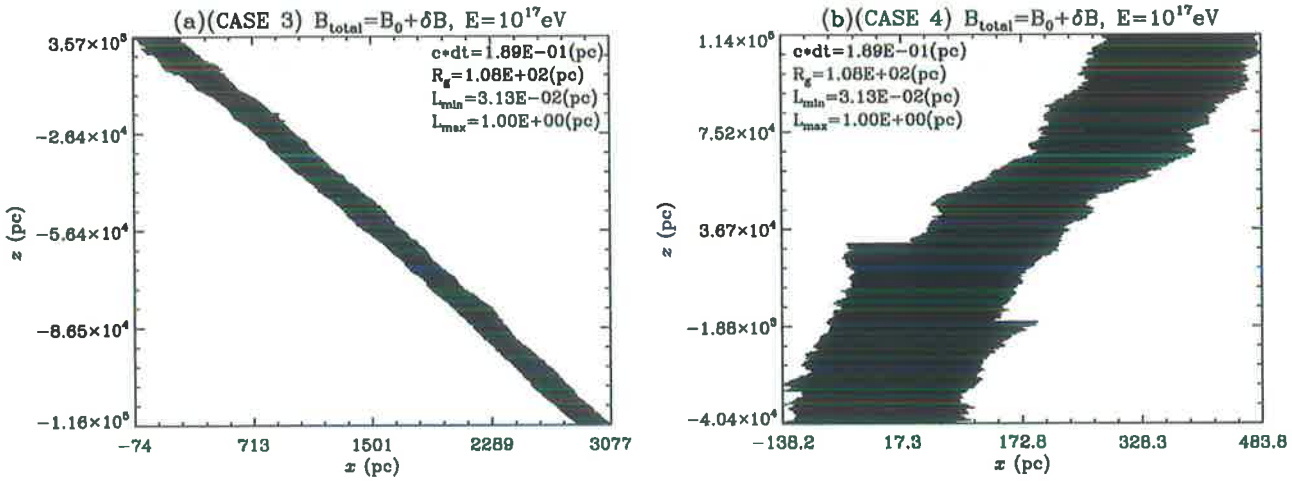

Figure 3.31: (a) (CASE 3) Trajectory of 10^{17}eV proton. (b) (CASE 4) Trajectory of 10^{17}eV proton. The mean magnetic field B_0 is 10^{-10}T and the r.m.s. value of $\delta\vec{B}$ is 0.5×10^{-10}T. The maximum grid spacing (=turbulence scale) L_{max} is 1.0pc.

Figures 3.26 to 3.31 show the examples of proton trajectories in the Kolmogorov-type magnetic field background. The total magnetic field in the simulation consists of the mean magnetic field $\vec{B}_0$ and the irregular magnetic field $\delta\vec{B}$, and $\vec{B}_0$ is 10^{-10}T and the r.m.s. value $|\delta\vec{B}_{rms}|$ is 0.5×10^{-10}T. The maximum grid spacing L_{max} is 1.0pc and minimum grid spacing L_{min} is $\frac{1.0\text{pc}}{32} = 0.031$pc, where 32 is the number of grid points in one direction.

Figures 3.26 and 3.27 show the trajectories of low energy protons ($E = 10^{13}$eV). The trajectories of the four cases have similar appearance to each other, whereas in the 10^{13}eV proton trajectories for the single grid spacing shown in Figures 3.7 and 3.8, the appearances of CASE 1 and CASE 2 trajectories are different from CASE 3 and CASE 4 trajectories due to three-dimensional magnetic field interpolation. The trajectories shown in Figures 3.26 to 3.27 are different from those of the single grid spacing magnetic fields shown in Figures 3.7 and 3.8. This may be because the structure of turbulent magnetic field is different between the single grid spacing magnetic field and Kolmogorov-like magnetic

field, the introduction of smaller scales making the results less sensitive to whether or not interpolation is used.

Figures 3.28 and 3.29 show the trajectories of low energy protons ($E = 10^{15}$eV). The gyroradius of 10^{15}eV for $B_0 = 10^{-10}$T is $\sim$ 1.0pc and is comparable to the maximum grid spacing L_{max}.

Figures 3.30 and 3.31 show the trajectories of higher energy protons ($E = 10^{17}$eV). The trajectories of the four cases are also similar in appearance to each other. However, the 10^{17}eV proton trajectories in the Kolmogorov-like magnetic field shown in Figures 3.26 and 3.27 are different from those in the single grid spacing magnetic fields shown in Figures 3.11 and 3.12. The trajectories of 10^{17}eV protons in single grid spacing magnetic fields shown in Figures 3.11 and 3.12 have more fluctuations than those in Kolmogorov-like magnetic fields shown in Figures 3.26 and 3.27. This also may be due to the structural difference between the single grid spacing magnetic field and the Kolmogorov-like magnetic field.

In the next section I will discuss the proton diffusion in Kolmogorov-like magnetic fields adopting CASE 1 magnetic field.

3.3.3 Calculation of diffusion tensor (Kolmogorov magnetic fields)

Diffusion tensors for propagation of cosmic ray protons in Kolmogorov-type turbulent magnetic fields were obtained from the positions of the protons at various time by using Equation 3.1.2 and 3.1.3. The procedure was explained in Section 3.2.4. The CASE 1 was adopted for cosmic ray diffusion simulations because CASE 1, CASE 2 and CASE 3 could not replace CASE 1 simulation even though they saved calculation time, because CASE 1 magnetic field is the most realistic among four cases.

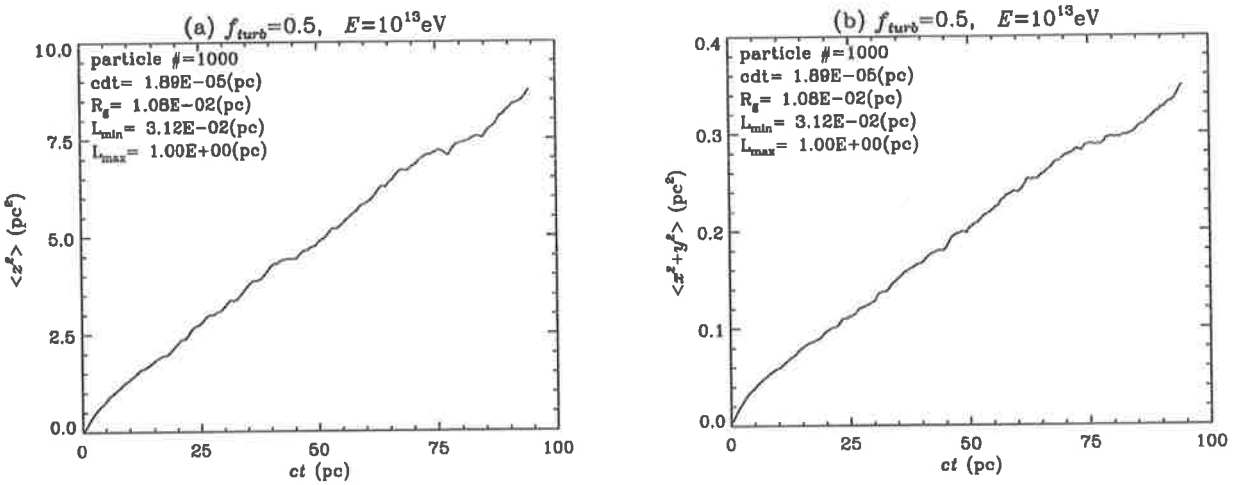

Figure 3.32: (a) $\langle z^2 \rangle$ as a function of time. (b) $\langle x^2+y^2 \rangle$ as a function of time. A turbulence level is $f^H_{turb} = 0.5$ and the proton's energy is $E = 10^{13}$eV. The irregular magnetic field has a Kolmogorov spectrum of turbulence.

Figure 3.32 shows the plots of $\langle z^2 \rangle$ and $\langle x^2+y^2 \rangle$ as a function of time for 10^{13}eV protons in Kolmogorov-type magnetic fields. The turbulence level parameter, f_{turb} in Figure 3.32, was introduced by Honda and is defined as

$$f^H_{turb} = \frac{|\delta B_{rms}|}{B_0}. \tag{3.3.10}$$

The maximum grid spacing in this simulation is 1.0pc and is about 100 times larger than the gyroradius for a 10^{13}eV proton.

Figure 3.33 shows plots of $\langle z^2 \rangle$ and $\langle x^2 + y^2 \rangle$ as a function of time for 10^{15}eV protons in Kolmogorov-type magnetic fields. The gyroradius of 10^{15}eV proton for $B_0 = 10^{-10}$T is $\sim$ 1.0pc and is comparable to L_{max}. In Figure 3.33 the curves in region $ct <$ 4kpc seem to be parabolic curves and the curves in region $ct >$ 4kpc are close to straight lines. This implies that two regimes may exist in 10^{15}eV proton diffusion, namely linear regime ($ct <$ 4kpc) and diffusive regime ($ct >$ 4kpc).

Figure 3.34 shows plots of $\langle z^2 \rangle$ and $\langle x^2+y^2 \rangle$ as a function of time for 10^{17}eV protons in

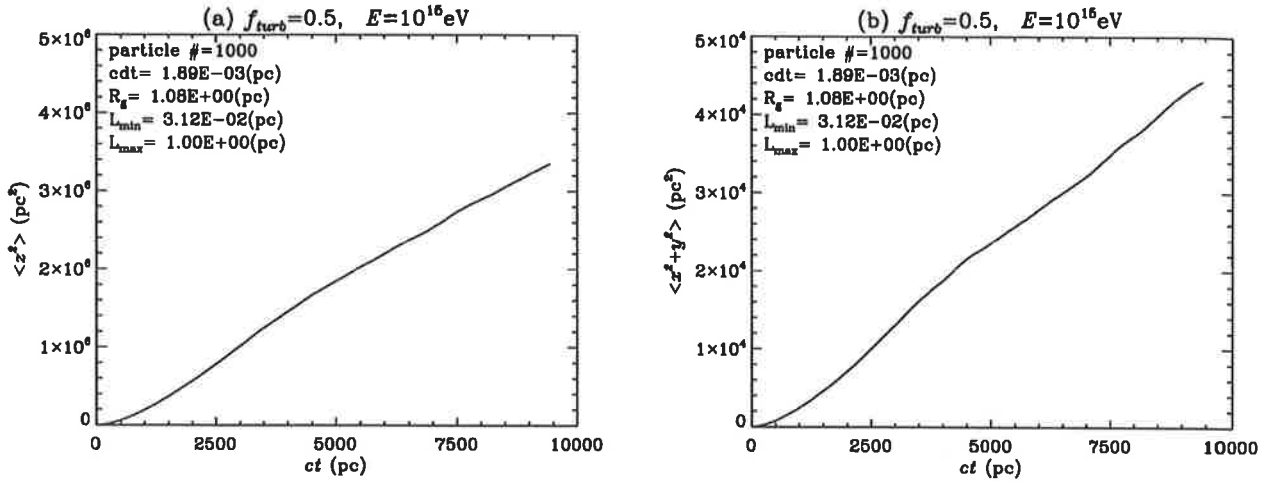

Figure 3.33: (a) $\langle z^2 \rangle$ as a function of time. (b) $\langle x^2+y^2 \rangle$ as a function of time. A turbulence level is $f^H_{turb} = 0.5$ and the proton's energy is $E = 10^{15}$eV. The irregular magnetic field has a Kolmogorov spectrum of turbulence.

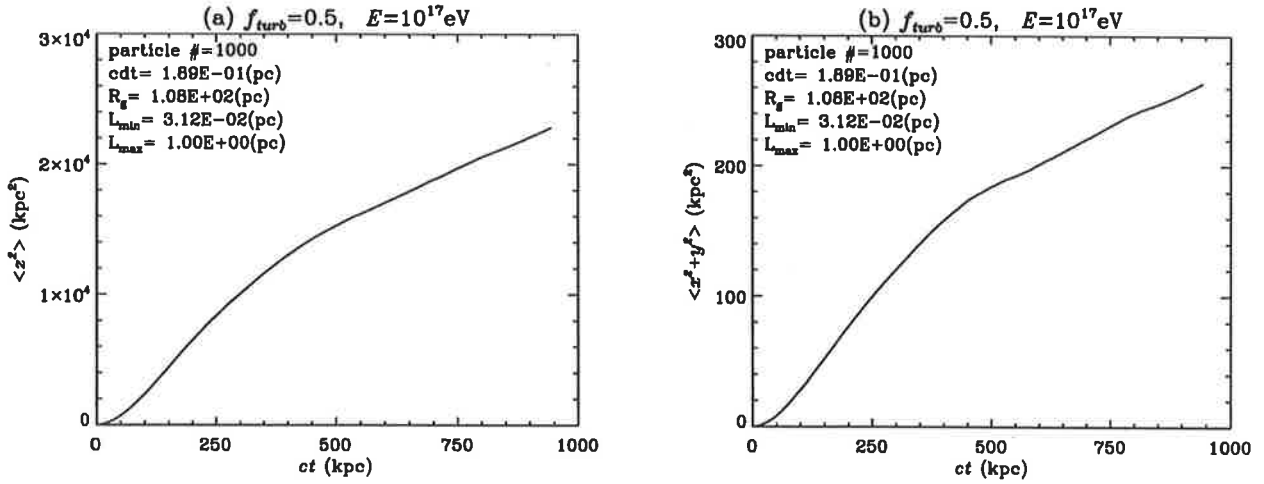

Figure 3.34: (a) $\langle z^2 \rangle$ as a function of time. (b) $\langle x^2 + y^2 \rangle$ as a function of time. The turbulence level is $f^H_{turb} = 0.5$ and the proton's energy is $E = 10^{17}$eV. The irregular magnetic field is Kolmogorov turbulence.

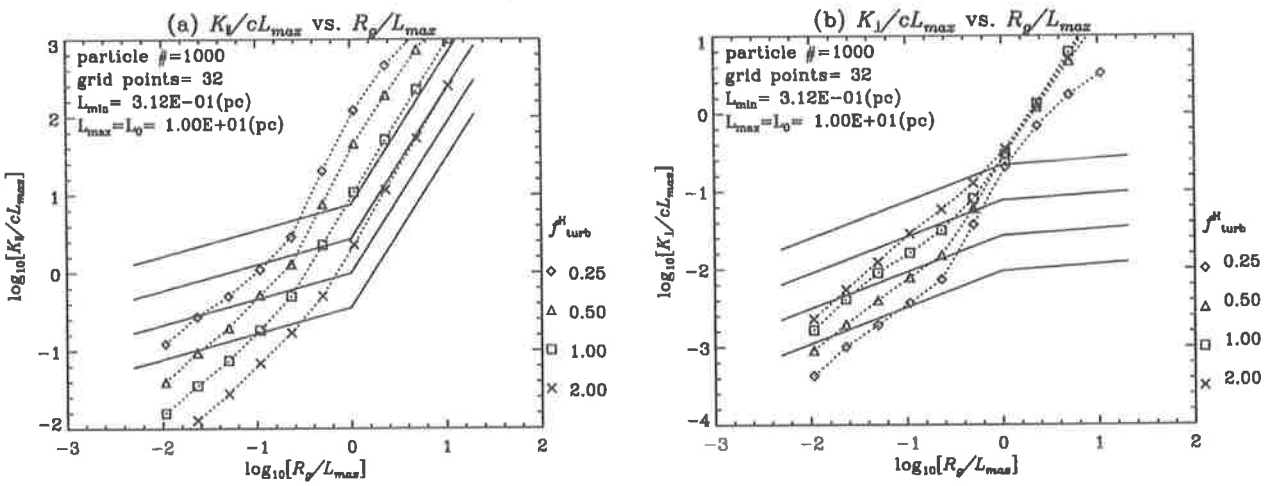

Figure 3.35: (a) Diffusion coefficients parallel to the mean magnetic field $B_0\hat{e}_z$ as a function of R_g/L_{max}. (b) Diffusion coefficients perpendicular to the mean magnetic field $B_0\hat{e}_z$ as a function of R_g/L_{max}. Solid lines are fits to Honda's results.

Kolmogorov-type magnetic fields. The slopes in Figure 3.34 decrease at time $ct \approx 400$kpc, which is of the order of the gyroradius in the regular field. The magnetic fields may prevent 10^{17}eV protons from diffusing in the $ct \geq 400$pc region.

	$E = 10^{13}$eV		$E = 10^{17}$eV	
	$K_\parallel$ [pc^2/sec]	$K_\perp$ [pc^2/sec]	$K_\parallel$ [pc^2/sec]	$K_\perp$ [pc^2/sec]
(CASE 1)	4.26×10^{-10}	8.32×10^{-12}	1.19×10^{-4}	6.91×10^{-7}

Table 3.6: The diffusion tensor components for the 10^{13}eV and 10^{17}eV protons in Kolmogorov magnetic fields. $K_\parallel$ represents diffusion tensor component parallel to the mean magnetic field. $K_\perp$ represents diffusion tensor component perpendicular to the mean magnetic field.

The diffusion tensors $K_\parallel$ and $K_\perp$ were calculated from the slopes of $\langle z^2 \rangle$ vs. time plots and $\langle x^2 + y^2 \rangle$ vs. time plots respectively. Table 3.6 shows the values of the diffusion coefficients for the 10^{13}eV and 10^{17}eV protons in Kolmogorov magnetic fields.

Honda analysed the $\frac{R_g}{L_{max}}$ dependence of the diffusion components. The parallel ($K_\parallel$)

and perpendicular ($K_\perp$) diffusion components were calculated by using CASE 1 simulation and compared with Honda's results. Figure 3.35 shows the plots of $\frac{K_\parallel}{cL_{max}}$ and $\frac{K_\perp}{cL_{max}}$ as a function of $\frac{R_g}{L_{max}}$. The maximum grid spacing is 10pc. The energy range of the protons is 10^{14}eV$< E < 10^{18}$eV and the corresponding gyroradius for this energy range is 0.1pc$< R_g <$ 1000pc for $B_0 = 10^{-10}$T. The solid lines in Figure 3.35 are fits to simulations by Honda [11] who found that the slope of K vs. R_g changed at $\log_{10}[\frac{R_g}{L_{max}}] = 0$. However, the simulation results do not agree with Honda's result. In Figure 3.35 (a) the data in the region $\log_{10}[\frac{R_g}{L_{max}}] > 0$ have the same slope as the solid lines, whereas the data in the region $\log_{10}[\frac{R_g}{L_{max}}] < 0$ are not consistent with the solid lines. In Figure 3.35 (b) the present results in the region $\log_{10}[\frac{R_g}{L_{max}}] \sim 0$ are of the same order of magnitude as the solid lines, but elsewhere the present data deviate from the solid lines. There are several possible explanations for this difference. This simulation uses a periodic boundary condition for producing turbulent magnetic fields, which Honda did not mention in his study. In Honda's study, the vector potentials $\delta\vec{A}$ follow an exponential distribution. However, in the present Honda simulation, the normal distribution was used instead to allow for negative values of the Cartesian components of $\delta\vec{A}$. This may also cause the difference in the results. The different index α in the turbulence energy density on different scales, $[\mathrm{L}_i]^\alpha$ (L_i: the i-th grid spacing), may be one of the causes for the different results shown in Figure 3.35. Honda's original work used $\alpha = \frac{5}{3}$, whereas here $\alpha = \frac{2}{3}$ was used as we found that the magnetic fields with $\alpha = \frac{2}{3}$ showed a Kolmogorov spectrum as indicated in Figure 3.25. Another possibility is that the number of time steps were not large enough for protons to reach the diffusion state.

Figure 3.36 shows the plots of $K_\parallel$ and $K_\perp$ as a function of energy E. In Figure 3.36 the energy dependence of $K_\parallel$ and $K_\perp$ change at $E = 10^7$GeV ($= 10^{16}$eV). The maximum

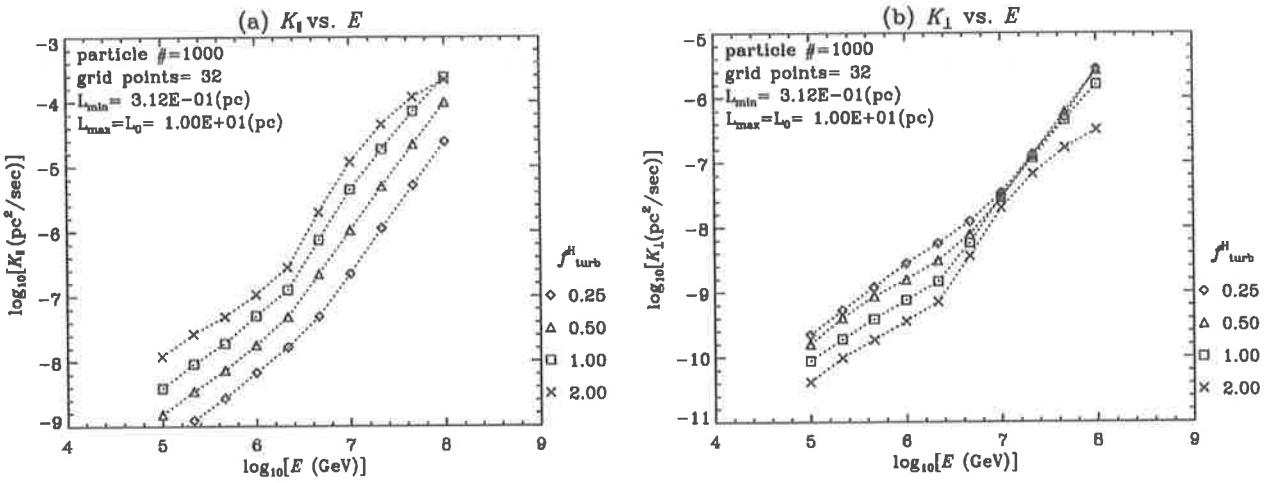

Figure 3.36: (a) The plots of diffusion tensor parallel to the mean magnetic field $B_0\hat{e}_z$ as a function of E(GeV). (b) The plots of diffusion tensor perpendicular to the mean magnetic field $B_0\hat{e}_z$ as a function of E(GeV).

grid spacing L_{max} is 10pc and the gyroradius R_g of 10^{16}eV protons for $B_0 = 10^{-10}$T is about 11pc. Appearances in Figure 3.36 are consistent with those in Figure 3.35 since R_g is proportional to E.

Figure 3.37 shows the time offset ct_{offset} from $ct = 0$ as a function of E(GeV). When the least squares fitting method was used to calculate the slopes $\frac{\langle z^2\rangle}{t}$ and $\frac{\langle x^2+y^2\rangle}{t}$ in the simulation, the the lines of best fit did not exactly start at $ct = 0$. The time offset is the difference between $ct = 0$ and the starting point of the line of best fit. The time offsets are close to 0 in the region $E < 10^6$GeV. However, they start increasing at 10^7GeV and increase rapidly at 10^8GeV. This suggests that in the lower energy region ($E < 10^7$GeV) the plots of $\langle z^2\rangle$ and $\langle x^2 + y^2\rangle$ vs. ct are close to straight lines starting from $ct = 0$, whereas in the higher energy region the large offset may imply a combination of diffusive and linear propagation.

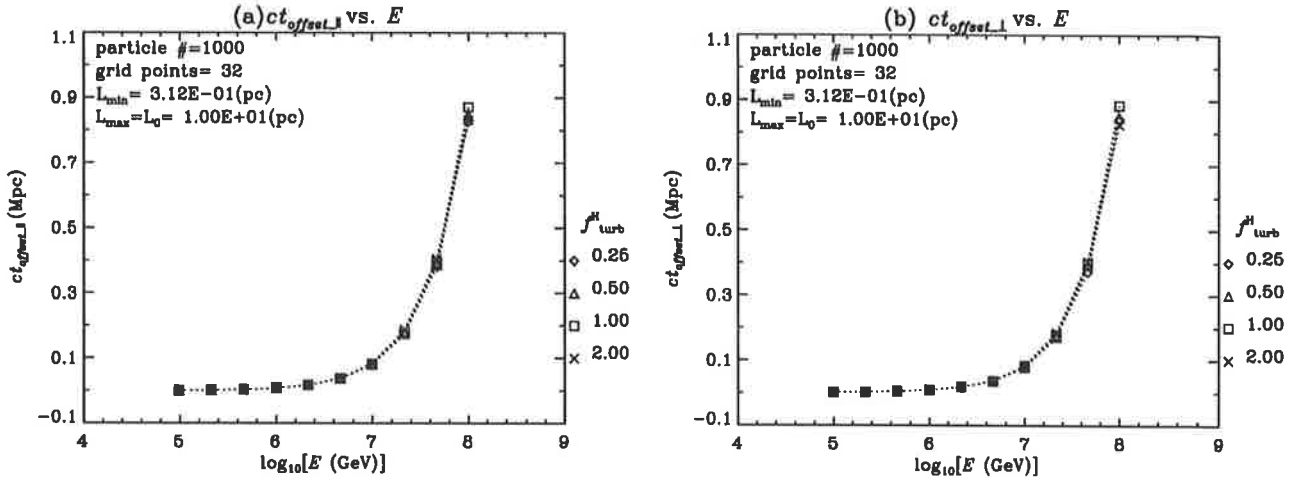

Figure 3.37: (a) The plots of time offset from $ct = 0$ as a function of E(GeV) when the diffusion tensor is parallel to the mean magnetic field $B_0\hat{e}_z$. (b) The plots of time offset from $ct = 0$ as a function of E(GeV) when the diffusion tensor perpendicular to the mean magnetic field $B_0\hat{e}_z$.

3.4 Summary and conclusion

Honda studied cosmic ray diffusion in Kolmogorov-type turbulent magnetic fields. He used a three-dimensional grid space and calculated $\vec{\nabla} \times \delta\vec{A}$ at each grid point to produce an irregular magnetic field $\delta\vec{B}$. The vector potentials in his original simulation were sampled from a Monte Carlo simulation and followed an exponential distribution.

In repeating Honda's simulation, two types of turbulent magnetic fields were examined; single grid spacing magnetic fields and Kolmogorov-type magnetic fields. To create turbulent magnetic fields, Monte Carlo simulation was used for sampling vector potential components from a normal distribution. The simulation applied periodic boundary conditions to the turbulent magnetic fields to save calculation time. The turbulent magnetic fields on the grid points were calculated from $\vec{\nabla} \times \delta\vec{A}$ and interpolation was implemented inside a cube between grid points. This simulation was named CASE 1 and was compared to other three cases:

1. $\vec{\nabla} \times \delta\vec{A}$ calculation, and interpolation: (CASE 1).

2. No $\vec{\nabla} \times \delta\vec{A}$ calculation, and interpolation: (CASE 2).

3. $\vec{\nabla} \times \delta\vec{A}$ calculation, and no interpolation: (CASE 3).

4. No $\vec{\nabla} \times \delta\vec{A}$ calculation, and no interpolation: (CASE 4).

These three cases (No.2 $\sim$ No.4) had less calculation time than CASE 1,and the CASE 3 and CASE 4 simulations were much faster than the CASE 1 simulation because interpolation at each proton position were not implemented. However, proton trajectories of these three simulation cases had different features from the CASE 1 simulation, and the values of diffusion tensor components from these three simulations were not consistent with the diffusion tensor components from the CASE 1 simulation. The quasi-linear theory approximation agreed with the diffusion tensors calculated from CASE 1 simulation to an order of magnitude. Therefore, CASE 1 simulation method was used for the simulation of high energy proton diffusion in a turbulent magnetic field.

Kolmogorov-type magnetic fields were created by using grid spaces with different grid sizes $L_i = 2^{-i/2}L_0$, where L_0 is the maximum grid spacing. The magnitude of the magnetic field for each grid spacing was $[L_i]^{\alpha}$. Honda proposed that it is $[L_i]^{5/3}$ for a Kolmogorov-type magnetic field. Stanev et al. [24] calculated the energy density of the Kolmogorov magnetic field $\vec{B}(\vec{k})$. They showed that

$$\vec{B}(\vec{k}) \propto k^{-2/3} \propto L_i^{2/3}, \tag{3.4.1}$$

where $\vec{k}$ is the wavevector. The energy density $B(k_x)$ was calculated by using discrete Fourier transform method, and the two forms ($\alpha = \frac{5}{2}$ by Honda or $\alpha = \frac{2}{3}$ by Stanev et al.) were compared. It seemed that the energy density by applying $\alpha = \frac{2}{3}$ was close to

Kolmogorov spectral line as shown in Figure 3.25. Therefore $[L_i]^{2/3}$ was chosen for creating a Kolmogorov-type turbulent magnetic field.

Diffusion tensors calculated from the present version of Honda's simulation were compared to the results from Honda's original work. The plots of parallel diffusion component $K_{\parallel}$ in Figure 4.6 do not agree with Honda's results in the low energy region ($\log_{10}[\frac{R_g}{L_{max}}] < 0$), and the plots of the perpendicular diffusion coefficient $K_{\perp}$ in Figure 4.6 do not agree with Honda's results in the high energy region ($\log_{10}[\frac{R_g}{L_{max}}] > 0$). These differences could be explained by four possibilities:

1. The present simulation used the normal distribution instead of exponential distribution to sample vector potentials $\delta\vec{A}$.

2. The present simulation used periodic boundary conditions, so the magnetic fields repeated every 32 grid points.

3. The present simulation used $\alpha = \frac{2}{3}$ instead of $\alpha = \frac{5}{3}$ for lattice constant $[L_i]^{\alpha}$.

4. The number of time steps was not large enough to accurately calculate diffusion tensors.

Cosmic ray diffusion simulations proposed by Giacalone and Jokipii will be discussed, and compared with present results using Honda's simulation method, in the next section.

Chapter 4

Simulation by Giacalone and Jokipii (1999)

4.1 Summary of Giacalone and Jokipii simulation

The simulation method used by Giacalone and Jokipii [9] is summarised in the following paragraphs. Giacalone and Jokipii used the superposition of plane waves to create a Kolmogorov-like magnetic field for the irregular part of the magnetic field. They proposed that the irregular part $\delta\vec{B}(x,y,z)$ be the superposition of plane waves with isotropic directions, and with random polarisations and phases. The irregular part $\delta\vec{B}(x,y,z)$ is

$$\delta\vec{B}(x,y,z) = \sum_{n=1}^{N_m} A(k_n)(\cos\alpha_n \hat{e}'_{xn} + i\sin\alpha_n \hat{e}'_{yn}) \exp\left(ik_n z'_n + i\beta_n\right) \tag{4.1.1}$$

where

$$\begin{pmatrix} x' \\ y' \\ z' \end{pmatrix} = \begin{pmatrix} \cos\theta_n\cos\phi_n & \cos\theta_n\sin\phi_n & -\sin\theta_n \\ -\sin\phi_n & \cos\phi_n & 0 \\ \sin\theta_n\cos\phi_n & \sin\theta_n\sin\phi_n & \cos\theta_n \end{pmatrix} \begin{pmatrix} x \\ y \\ z \end{pmatrix}$$

This matrix is the combination of rotation along the x-axis and the y-axis. This ensures $\delta\vec{B}$ is perpendicular to the wavevector $\vec{k}_n$ and $\vec{\nabla}\cdot\vec{B} = 0$ is automatically satisfied.In

Equation 4.1.1, α_n and β_n are the n-th polarisation and phase respectively, and α_n makes δB isotropic.

θ_n, ϕ_n, α_n and β_n are sampled randomly from each range,

$$\begin{cases} -1 < \cos\theta_n < 1 \quad (n = 1, 2, \cdots) \\ 0 < \phi_n < 2\pi \quad (n = 1, 2, \cdots) \\ 0 < \alpha_n < 2\pi \quad (n = 1, 2, \cdots) \\ 0 < \beta_n < 2\pi \quad (n = 1, 2, \cdots) \end{cases} \tag{4.1.2}$$

$A(k_n)$ expresses the amplitude of the n-th wave mode with wave number k_n as a Kolmogorov envelope to the power spectrum, and is proportional to $k_n^{-1/3}$. $A^2(k_n)$ is given by

$$A^2(k_n) = \sigma^2 G(k_n) \left[\sum_{n=1}^{N_m} G(k_n) \right]^{-1}, \tag{4.1.3}$$

where

$$G(k_n) = \frac{\triangle V_n}{1 + (k_n L_c)^\gamma}. \tag{4.1.4}$$

In Equations 4.1.3 and 4.1.4, σ^2 and L_c are the wave variance and the correlation length, respectively. $\triangle V_n$ is a normalization factor. For three-dimensional turbulence, $\triangle V_n = 4\pi k_n^2 \triangle k_n$. Giacalone and Jokipii noted that the index γ also depended on the dimension of the turbulence. The index γ is $\frac{11}{3}$ for three-dimensional Kolmogorov spectrum.

The trajectories of the charged particles were calculated by the equation of motion. They calculated new magnetic fields from the constants α_n, β_n, $\cdots$ etc., each time a particle changed its position, whereas Honda [11] set magnetic fields at each lattice point initially and interpolated. Interpolation was not necessary in the Giacalone and Jokipii simulation. The method of calculation of diffusion tensors is the same as that used by

Honda.

4.2 Repeating Giacalone and Jokipii simulation

4.2.1 Creating Kolmogorov magnetic fields

Giacalone and Jokipii [9] simulated Kolmogorov turbulent magnetic fields by using the superposition of plane waves. The superimposed plane waves which Giacalone and Jokipii proposed is defined as Equation 4.1.1. However, Equations 4.1.1, 4.1.3 and 4.1.4 seem unnecessarily complicated, and therefore, a simpler but equivalent plane wave method was applied to generate an irregular magnetic field. Equation 4.2.1 is a revised definition of irregular magnetic fields.

$$\delta\vec{B}(\vec{r}) = \sum_{n=1}^{N_m} A(k_n)\hat{n}\cos\left(k_n\hat{\xi}_n\cdot\vec{r}-\psi_n\right), \tag{4.2.1}$$

where k_n is n-th wavenumber and $\hat{\xi}_n$ is n-th unit vector, giving the direction of the wave, so the n-th wavevector is $\vec{k}_n = k_n\hat{\xi}_n$. The minimum wavenumber is defined as $k_{min} = \frac{2\pi}{L_0}$, where L_0 is the scale of the turbulent magnetic fields and is assumed to be 1pc (parsec) $= 3\times10^{16}$m. The maximum wavenumber is $k_{max} = 10^3 k_{min}$. Wavenumber k_n was obtained from following method. In logarithmic scale the minimum and maximum wavenumber are

$$\ln k_{min} = \ln\left[\frac{2\pi}{L_0}\right], \qquad \ln k_{max} = \ln\left[10^3 k_{min}\right]. \tag{4.2.2}$$

Using Equation 4.2.2, n-th wavenumber is

$$\begin{aligned}\ln k_n &= \exp\left[\ln k_{min} + \eta(\ln k_{max} - \ln k_{min})\right] \\ &= \exp\left[\ln k_{min} + \eta\ln 10^3\right]\end{aligned} \tag{4.2.3}$$

where η is randomly selected from $0 < \eta < 1$.

ψ_n is the phase, sampled randomly from $0 \le \psi_n \le 2\pi$. The number of plane waves N_m is set to be 100, so that $\delta\vec{B}$ becomes isotropic. The vector $\hat{n}$ is the n-th unit vector giving

the direction of the field and is sampled uniformly in azimuth in a plane perpendicular to $\hat{\xi}_n$, so $\hat{n} \cdot \hat{\xi}_n$ becomes 0 and therefore $\nabla \cdot (\delta \vec{B}) = 0$ is ensured.

The amplitude $A(k_n)$ is also simplified instead of using Equations 4.1.3 and 4.1.4 directly. If the index $\gamma = \frac{11}{3}$ is applied to $G(k_n)$, because $\triangle V_n = 4\pi k_n^2 \triangle k_n \propto k_n^3$, $G(k_n)$ will become

$$\begin{aligned} G(k_n) &= \frac{\triangle V_n}{1 + (k_n L c)^{11/3}} \approx \frac{\triangle V_n}{(k_n L c)^{11/3}} \\ &\propto \frac{k_n^3}{k_n^{11/3}} = k_n^{-2/3} \quad \text{for} \quad k_n L_c \gg 1. \end{aligned} \tag{4.2.4}$$

where $\triangle k_n$ is space between k_{n+1} and k_n, and is proportional to k_n because $\frac{\triangle k_n}{k_n} = \text{cons't.}$ In Equation 4.1.3, $[\sum_{n=1}^{N_m} G(k_n)]^{-1}$ is a normalization factor and is a constant. σ^2 is also a constant. Therefore the amplitude $A(k_n)$ becomes

$$\begin{aligned} A^2(k_n) = \sigma^2 G(k_n) \left[\sum_{n=1}^{N_m} G(k_n) \right]^{-1} &\propto k_n^{-2/3} \\ \therefore A(k_n) &\propto k_n^{-1/3} \end{aligned} \tag{4.2.5}$$

Finally the simpler version of irregular magnetic field $\delta \vec{B}$ is

$$\delta \vec{B}(\vec{r}) = \frac{1}{C} \sum_{n=1}^{N_m} k_n^{-1/3} \hat{n} \cos\left(k_n \hat{\xi}_n \cdot \vec{r} - \psi_n\right), \tag{4.2.6}$$

where C is a normalization constant. Due to $A(k_n) \propto k_n^{-1/3}$ in Equation 4.2.6, the energy density $|\delta B(\vec{k})|^2$ will show the Kolmogorov spectrum.

In Equation 4.2.6, unit vectors $\hat{n}$ and $\hat{\xi}_n$ must be normal to each other to satisfy $\vec{\nabla} \cdot \vec{B} = 0$. In order to make $\hat{n}$ and $\hat{\xi}_n$ orthogonal, the following algorithm is used. Firstly arbitrary wavevector $\vec{k}_n (= k_n \hat{\xi}_n)$ is selected. The vector product of the unit vector $\hat{z} = (0, 0, 1)$ and $\vec{k}_n$ is calculated as (a) of Figure 4.1 shows

$$\vec{p}_1 = \vec{k} \times \hat{z}. \tag{4.2.7}$$

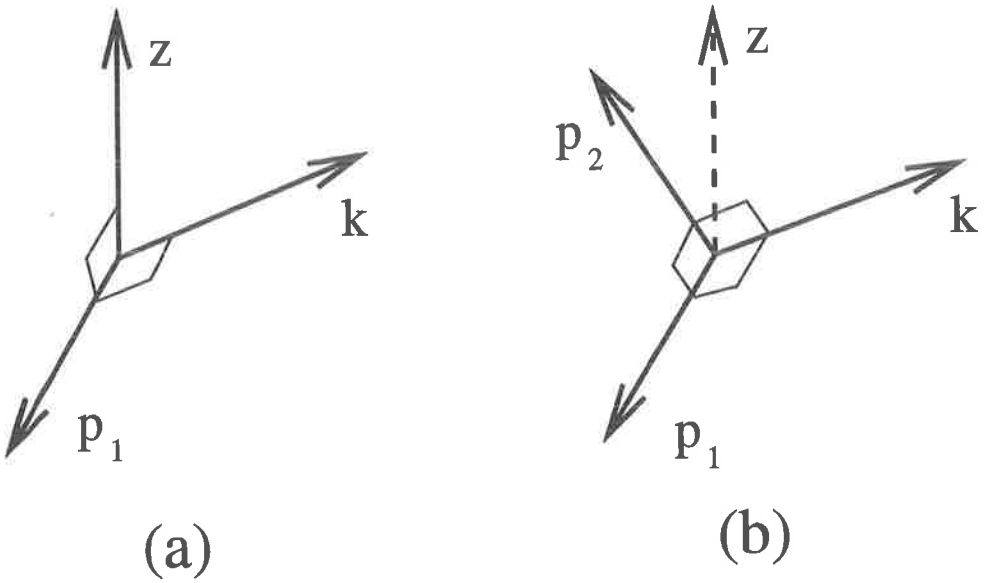

Figure 4.1: Schematic diagram of unit vectors $\hat{p}_1$ and $\hat{p}_2$ which are perpendicular to wavevector $\vec{k}_n$. (a) Calculation of $\vec{k} \times \hat{z}$ gives $\vec{p}_1$. (b) Calculation of $\vec{p}_1 \times \vec{k}$ gives $\vec{p}_2$.

Calculating the vector product of $\vec{k}$ and $\vec{p}_1$ produces $\vec{p}_2$, so that $\vec{k}$, $\vec{p}_1$ and $\vec{p}_2$ are orthogonal to each other shown in Figure 4.1 (b).

$$\vec{p}_2 = \vec{p}_1 \times \vec{k} \tag{4.2.8}$$

The vectors $\vec{p}_1$ and $\vec{p}_2$ are then divided by their magnitude to obtain unit vectors $\hat{p}_1$ and $\hat{p}_2$.

$$\hat{p}_1 = \frac{\vec{p}_1}{|\vec{p}_1|}, \qquad \hat{p}_2 = \frac{\vec{p}_2}{|\vec{p}_2|} \tag{4.2.9}$$

Arbitrary angles ϕ are chosen from the angle range $0 \leq \phi \leq 2\pi$ for isotropy to create unit vector perpendicular to $\vec{k}_n$ namely,

$$\hat{n} = \begin{pmatrix} \cos\phi & \sin\phi \end{pmatrix} \begin{pmatrix} \hat{p}_1 \\ \hat{p}_2 \end{pmatrix} = \cos\phi \begin{pmatrix} p_{1,x} \\ p_{1,y} \\ p_{1,z} \end{pmatrix} + \sin\phi \begin{pmatrix} p_{2,x} \\ p_{2,y} \\ p_{2,z} \end{pmatrix}.$$

As a result, components of the irregular magnetic fields $\delta\vec{B}$ become perpendicular to the wavenumber vectors $\vec{k}_n$ and assures $\vec{\nabla} \cdot \delta\vec{B} = 0$.

4.2.2 Trajectories of charged particles

Table 4.1 shows the values of the important parameters in the simulation. A proton is selected as a charged cosmic ray.

Particle	proton ($m_p = 938$ MeV/c^2)
Energy, E	10^{13}eV$\leq E \leq 10^{16}$eV
B_0	10^{-10}T $(= 1\mu$G)
$\lvert\delta\vec{B}_{rms}\rvert/B_0$	$\frac{1}{4}$, $\frac{1}{2}$, 1, 2
r_{gyro}	0.01pc$\leq r_{gyro} \leq$ 10pc
Wavenumber, k	$\frac{2\pi}{1\text{pc}} \leq k \leq \frac{2\pi}{1\text{pc}} \times 1000$
Step size, $c\triangle t$	$0.01 \times r_{gyro}$

Table 4.1: Some important values of the cosmic ray and the magnetic fields in the simulation.

In the study of Giacalone and Jokipii [7] [8] [9], they applied their simulation to the interplanetary magnetic fields. The range of the particle energy they assumed was 10^6eV$\leq E \leq 10^9$eV and they set the mean homogeneous magnetic field being 50×10^{-10}T$(= 50\mu$G). However, this research focuses on the propagation of relativistic cosmic rays ($E \geq 10^{15}$eV), and so the energy range was changed to 10^{13}eV$\leq E \leq 10^{16}$eV. The Galactic magnetic fields were considered in this study, and so the strength of the mean magnetic field was set to $B_0 = 1 \times 10^{-10}$T$(= 1\mu$G). The ratios of the irregular and mean magnetic fields are

$$\frac{|\delta\vec{B}_{rms}|}{B_0} = \frac{2^n}{4}, \qquad (n = 0,\ 1,\ 2,\ 3). \tag{4.2.10}$$

The ratios are the same as those of Honda's simulation [11], so the outcome of the simulation can be compared to Honda's result. The gyroradius r_{gyro} has the range from 0.01pc to 10pc. This range correlates to the proton's energy range. The gyroradius is calculated

from Equation 4.2.11,

$$r_{gyro}(\vec{r}) = \Big(\frac{\gamma_p}{10^6}\Big)\Big(\frac{1\mu\mathrm{G}}{|\vec{B}_0 + \delta\vec{B}(\vec{r})|}\Big)\ \mathrm{pc}, \tag{4.2.11}$$

where γ_p is the Lorentz factor of the proton and the range is

$$\gamma_p = 10^{(8+n)/2}, \qquad (n = 0,\ 1,\ \cdots,\ 6). \tag{4.2.12}$$

The minimum wavenumber is defined as $k_{min} = \frac{2\pi}{L_0}$, where L_0 is the turbulence scale and is set to 1pc($= 3 \times 10^{16}$m). The maximum wavenumber k_{max} is set to be 1000 times larger than the minimum wavenumber k_{min}, following Giacalone and Jokipii.

The time step size is set as follows. The product of the speed of light c and the time increment $\triangle t$ represents the step length and must be much smaller than the gyroradius,

$$c\triangle t \ll r_{gyro}. \tag{4.2.13}$$

The typically, the step size needs to be 100 times smaller than the gyroradius to maintain a circular orbit, namely

$$c\triangle t = 0.01 \times r_{gyro}. \tag{4.2.14}$$

In order to draw the trajectories of cosmic rays in the turbulent magnetic fields, the following method was applied. Firstly the velocity unit vector ,

$$\hat{\beta}(\vec{r}) = ([\hat{\beta}]_x, [\hat{\beta}]_y, [\hat{\beta}]_z) = \frac{1}{|\vec{v}(\vec{r})|}(v_x, v_y, v_z) \tag{4.2.15}$$

is defined. This expresses the direction of the particle. The proton starts at the origin and the initial direction $(\hat{\beta}_x, \hat{\beta}_y, \hat{\beta}_z)$ of the particle is randomly selected. Then the change in relativistic three-momentum in the units of mc is calculated by using the Lorentz force

$\vec{F} = q(\vec{v} \times \vec{B})$,

$$\begin{cases} p_{x,n+1} = p_{x,n} + \triangle p_x = p_{x,n} + 0.01\gamma_p([\hat{\beta}]_y[\hat{B}]_z - [\hat{\beta}]_z[\hat{B}]_y) \\ p_{y,n+1} = p_{y,n} + \triangle p_y = p_{y,n} + 0.01\gamma_p([\hat{\beta}]_z[\hat{B}]_x - [\hat{\beta}]_x[\hat{B}]_z) \\ p_{z,n+1} = p_{z,n} + \triangle p_z = p_{z,n} + 0.01\gamma_p([\hat{\beta}]_x[\hat{B}]_y - [\hat{\beta}]_y[\hat{B}]_x) \end{cases} \tag{4.2.16}$$

where $([\hat{B}]_x, [\hat{B}]_y, [\hat{B}]_z)$ is the unit magnetic field vector and is defined as

$$\hat{B}(\vec{r}) = ([\hat{B}]_x, [\hat{B}]_y, [\hat{B}]_z) = \frac{1}{|\vec{B}(\vec{r})|}(B_x, B_y, B_z). \tag{4.2.17}$$

From Equation 4.2.15 to 4.2.17, the new direction of the particle $\hat{\beta}_{new}(\vec{r})$ is calculated as

$$\hat{\beta}_{new}(\vec{r}) = ([\hat{\beta}]_x, [\hat{\beta}]_y, [\hat{\beta}]_z) = \frac{1}{|\vec{p}(\vec{r})|}(p_x, p_y, p_z). \tag{4.2.18}$$

Finally, the particle's $(n+1)$-th position, $\vec{r}_{n+1} = (x_{n+1}, y_{n+1}, z_{n+1})$ is calculated from

$$\begin{cases} x_{n+1} = x_n + \hat{\beta}_{x,n}[c\triangle t_n] \\ y_{n+1} = y_n + \hat{\beta}_{y,n}[c\triangle t_n]. \\ z_{n+1} = z_n + \hat{\beta}_{z,n}[c\triangle t_n] \end{cases} \tag{4.2.19}$$

where $(\hat{\beta}_{x,n},\ \hat{\beta}_{y,n},\ \hat{\beta}_{z,n})$ is the n-th velocity unit vector and $[c\triangle t_n]$ is the n-th step size.

In the simulation, the maximum time scale $[ct]_{max}$ is introduced. The time span should be large enough for the particle to reach the diffusion regime. The results from Honda's simulation [11] are used for setting the maximum time scale $[ct]_{max}$. The maximum time scales for $\frac{r_{gyro}}{L_0} < 1$ are

$$\begin{aligned} [ct]_{max,\parallel} &= 100 \times L_0\Big(\frac{K_\parallel^0}{cL_0}\Big)\Big(\frac{\delta B_{rms}}{B_0}\Big)^{\alpha\parallel}\Big(\frac{r_{gyro}}{L_0}\Big)^{\beta\parallel} \\ &= 100 \times L_0(0.981)\Big(\frac{\delta B_{rms}}{B_0}\Big)^{-1.465}\Big(\frac{r_{gyro}}{L_0}\Big)^{0.332} \end{aligned} \tag{4.2.20}$$

$$\begin{aligned} [ct]_{max,\perp} &= 100 \times L_0\Big(\frac{K_\perp^0}{cL_0}\Big)\Big(\frac{\delta B_{rms}}{B_0}\Big)^{\alpha\perp}\Big(\frac{r_{gyro}}{L_0}\Big)^{\beta\perp} \\ &= 100 \times L_0(0.0765)\Big(\frac{\delta B_{rms}}{B_0}\Big)^{1.505}\Big(\frac{r_{gyro}}{L_0}\Big)^{0.470} \end{aligned} \tag{4.2.21}$$

The maximum time scales for $\frac{r_{gyro}}{L_0} > 1$ are

$$[ct]_{max,\parallel} = 100 \times L_0(0.981)\left(\frac{\delta B_{rms}}{B_0}\right)^{-1.465}\left(\frac{r_{gyro}}{L_0}\right)^{1.907} \tag{4.2.22}$$

$$[ct]_{max,\perp} = 100 \times L_0(0.0765)\left(\frac{\delta B_{rms}}{B_0}\right)^{1.505}\left(\frac{r_{gyro}}{L_0}\right)^{0.088} \tag{4.2.23}$$

Figures 4.2 and 4.3 show examples of trajectories of protons with smaller energy ($E = 10^{13}$eV), and Figures 4.4 and 4.5 show examples of trajectories of protons with larger energy ($E = 10^{16}$eV). The turbulence parameter, f_{turb} is defined as

$$f_{turb} = \frac{|\delta B_{rms}|}{B_0}. \tag{4.2.24}$$

Equation 4.2.24 represents thc ratio of the magnetic fluctuation $|\delta B_{rms}|$ to the mean magnetic field B_0.

Figure 4.2 shows $E = 10^{13}$eV proton trajectories for $f_{turb} = \frac{1}{4}$ (a) and $f_{turb} = \frac{1}{2}$ (b). Figure 4.3 shows $E = 10^{13}$eV proton trajectories for $f_{turb} = 1$ (a) and $f_{turb} = 2$ (b). The gyroradius in the regular field $B_0 = 10^{-10}$T for energy $E = 10^{13}$eV is 0.01pc according to Equation 4.2.11, and is smaller than the turbulent scale, $L_0 = 1$pc. Therefore, the low energy protons tend to follow the magnetic field lines. Moreover, if the f_{turb} is smaller, this means the magnetic fluctuations are very small, and the effect of the mean magnetic field, B_0 becomes significant. Hence, the magnetic field lines with the small f_{turb} are close to straight lines toward z-direction. As a result, the cosmic rays in small f_{turb} magnetic field environment have tendency to move along z-direction, whereas in the large f_{turb} magnetic field environment, the cosmic rays have more chance to move in the x-direction and the y-direction.

Figure 4.4 shows $E = 10^{16}$eV proton trajectories for $f_{turb} = \frac{1}{4}$ (a) and $f_{turb} = \frac{1}{2}$ (b). Figure 4.5 shows $E = 10^{16}$eV proton trajectories for $f_{turb} = 1$ (a) and $f_{turb} = 2$ (b). The gyroradius for the energy $E = 10^{16}$eV is 10pc according to the Equation 4.2.11 and is

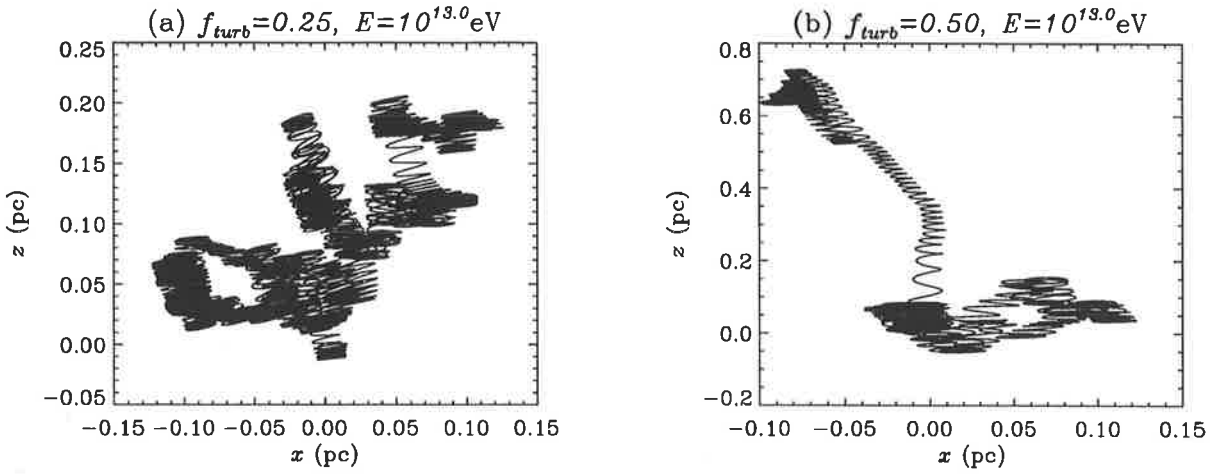

Figure 4.2: Trajectories of 10^{13}eV proton. (a) $f_{turb} = \frac{1}{4}$. (b) $f_{turb} = \frac{1}{2}$.

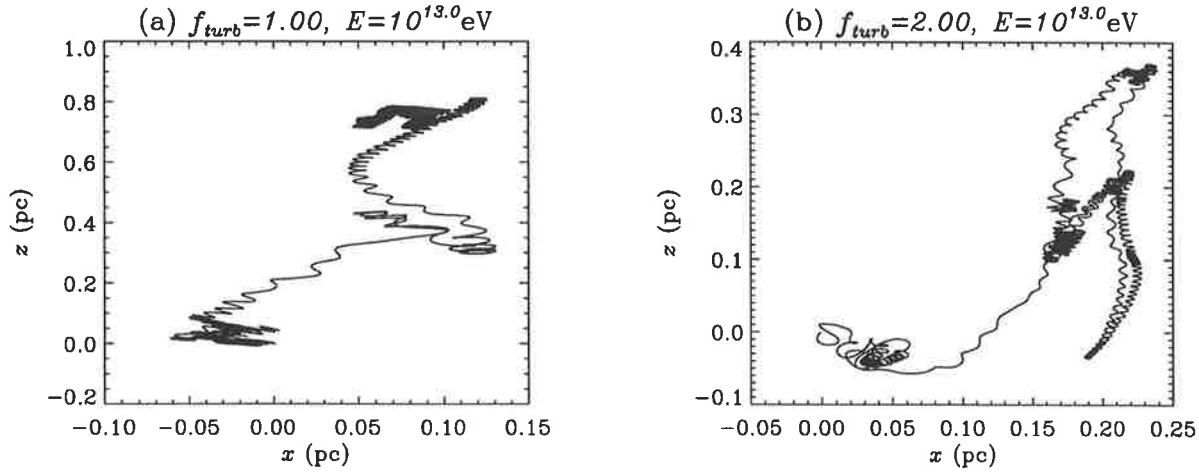

Figure 4.3: Trajectories of 10^{13}eV proton. (a) $f_{turb} = 1$. (b) $f_{turb} = 2$.

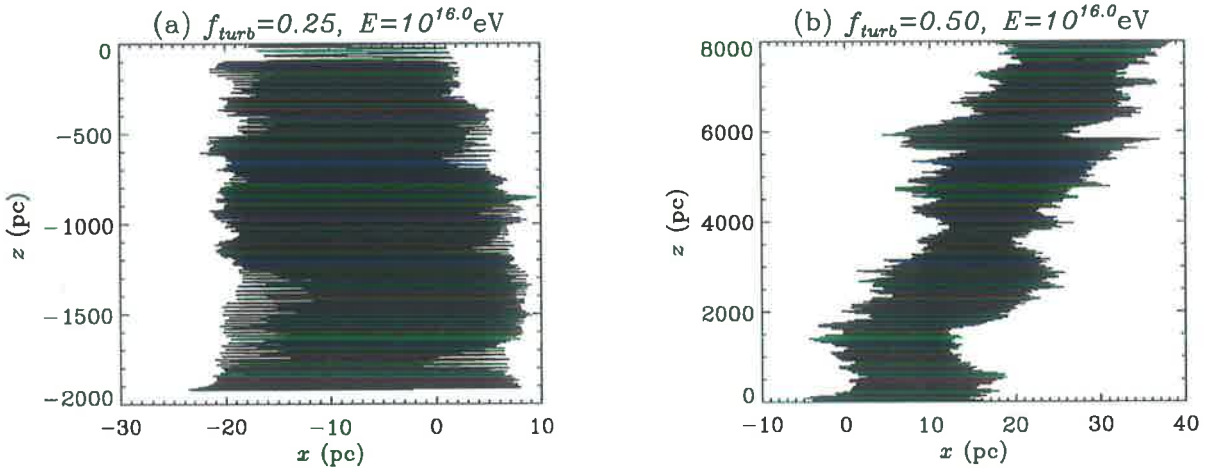

Figure 4.4: Trajectories of 10^{16}eV proton. (a) $f_{turb} = \frac{1}{4}$. (b) $f_{turb} = \frac{1}{2}$.

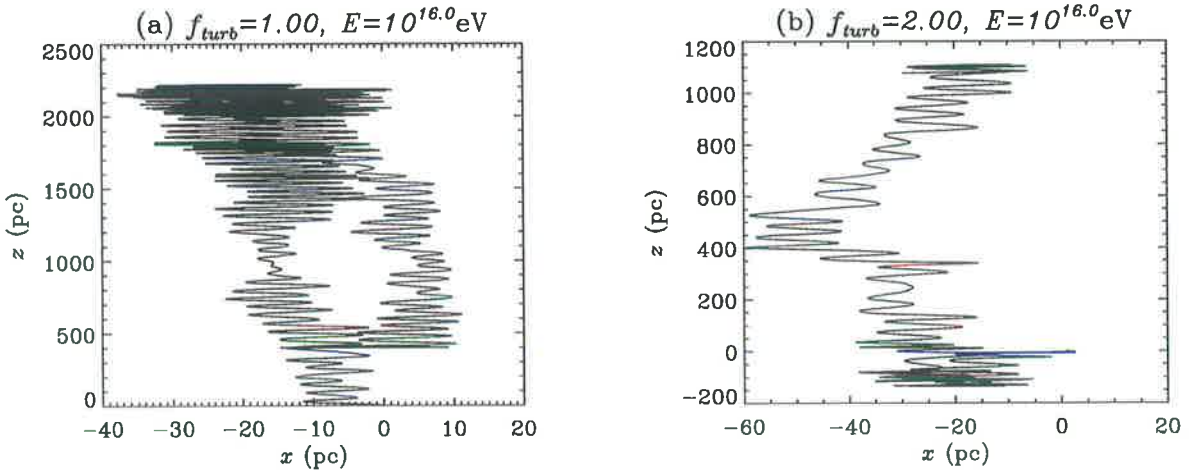

Figure 4.5: Trajectories of 10^{16}eV proton. (a) $f_{turb} = 1$. (b) $f_{turb} = 2$.

larger than the turbulence scale, $L_0 = 1$pc. This implies that higher energy proton will be affected by the magnetic fields but it is unlikely to follow single magnetic field lines. Figure 4.5 also shows that the high energy proton has an inclination to propagate in x-direction and y-direction if the large f_{turb} magnetic fields exist.

4.2.3 Calculation of diffusion tensor

Diffusion tensor calculations were implemented in the energy range $10^{13}\text{eV} \leq E \leq 10^{16}\text{eV}$. The diffusion coefficients perpendicular and parallel to the regular magnetic fields, B_0 are the average of squared distance divided by time, which are,

$$K_{\parallel} = \frac{\langle z^2 \rangle}{2t} \tag{4.2.25}$$

$$K_{\perp} = \frac{\langle x^2 + y^2 \rangle}{4t} \tag{4.2.26}$$

In Equations 4.2.25 and 4.2.26, the average of positions (x, y, z) is calculated over 2000 protons ($N_p = 2000$).

Figure 4.6 shows the behavior of the $\frac{K_{\parallel}}{cL_0}$ (a) and $\frac{K_{\perp}}{cL_0}$ (b) with respect to $\frac{r_g}{L_0}$ on a logarithmic scale. In Figure 4.6, L_0 represents turbulence scale and corresponds to $\frac{2\pi}{k_{min}}$, and c represents the speed of light. The $r_g (= r_{gyro})$ is the gyroradius and is proportional to proton energy. The f^H_{turb} represents the turbulence parameter in Honda's simulation and is defined as

$$f^H_{turb} = \frac{\langle \delta B_{rms} \rangle}{B_0}. \tag{4.2.27}$$

If $f^H_{turb} > 1$, the irregular magnetic field $\delta\vec{B}$ dominates the total magnetic field $\vec{B}_{total}$ and the total magnetic field fluctuates significantly. On the other hand, if $f^H_{turb} < 1$, the mean magnetic field $B_0\hat{e}_z$ dominates the total magnetic field.

The dashed lines in Figure 4.6 indicate the diffusion tensors calculated from Honda's result. As Honda noted, the behavior of the diffusion tensor is different for $\log_{10}\left(\frac{r_g}{L_0}\right) < 1$

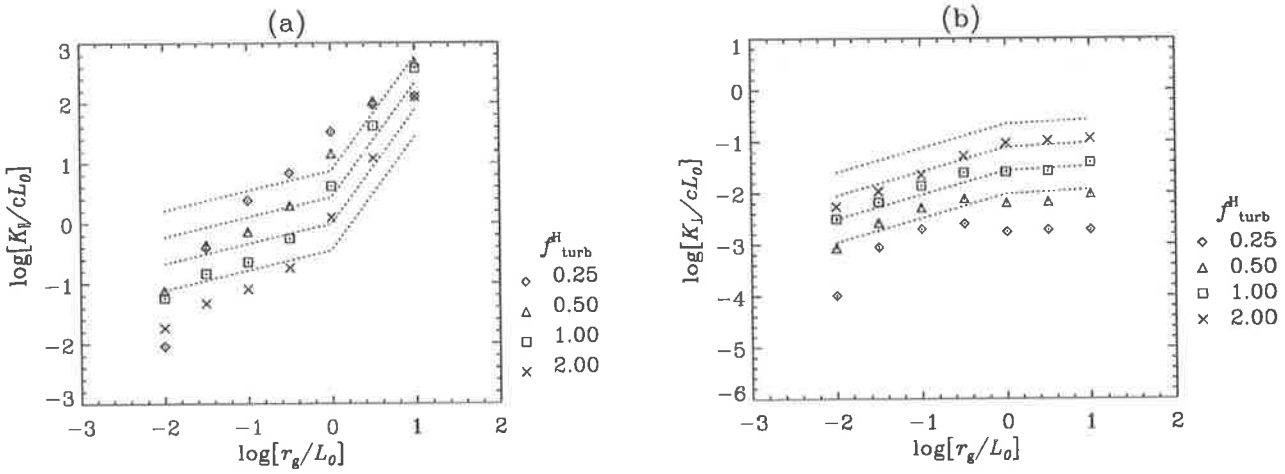

Figure 4.6: Diffusion tensor plot in logarithmic scale. Dotted curves from Honda for some f^H_{turb} values. (a) $\frac{K_\parallel}{cL_0}$ versus $\frac{r_g}{L_0}$ plot. (b) $\frac{K_\perp}{cL_0}$ versus $\frac{r_g}{L_0}$ plot.

and $\log_{10}\left(\frac{r_g}{L_0}\right) > 1$. It seems that difference between $\frac{K_\parallel}{cL_0}$ and $\frac{K_\perp}{cL_0}$ increases as $\frac{r_g}{L_0}$ becomes smaller.

The diffusion tensors $K_\parallel$ and $K_\perp$ at high energy ($\log\left(\frac{r_g}{L_0}\right) \gg 1$) are consistent with Honda's result. However, in the low energy regime ($\log\left(\frac{r_g}{L_0}\right) \ll 1$), the present result deviates from the dashed lines.

Casse et al. [5] have also performed propagation calculations using a method qualitatively similar to the method of Giacalone and Jokipii and applied it to relativistic particles. I shall compare my results with theirs. In the Casse et al. simulations [5], however, there is interpolation of the turbulent magnetic fields and so $\vec{\nabla} \cdot \vec{B} = 0$ is not exact.

Figure 4.7 shows the behavior of $\frac{K_\parallel}{r_g c}$ and $\frac{K_\perp}{r_g c}$ with respect to $\frac{2\pi r_g}{L_0}$ in logarithmic scale. The turbulence parameter in Casse et al. term f^C_{turb} is

$$f^C_{turb} = \frac{\langle \delta B^2_{rms} \rangle}{B_0^2 + \langle \delta B^2_{rms} \rangle}. \tag{4.2.28}$$

Distributions of the final distance of protons were compared for various f^H_{turb} and proton energies. The distributions of the proton's final positions for different injection angles were

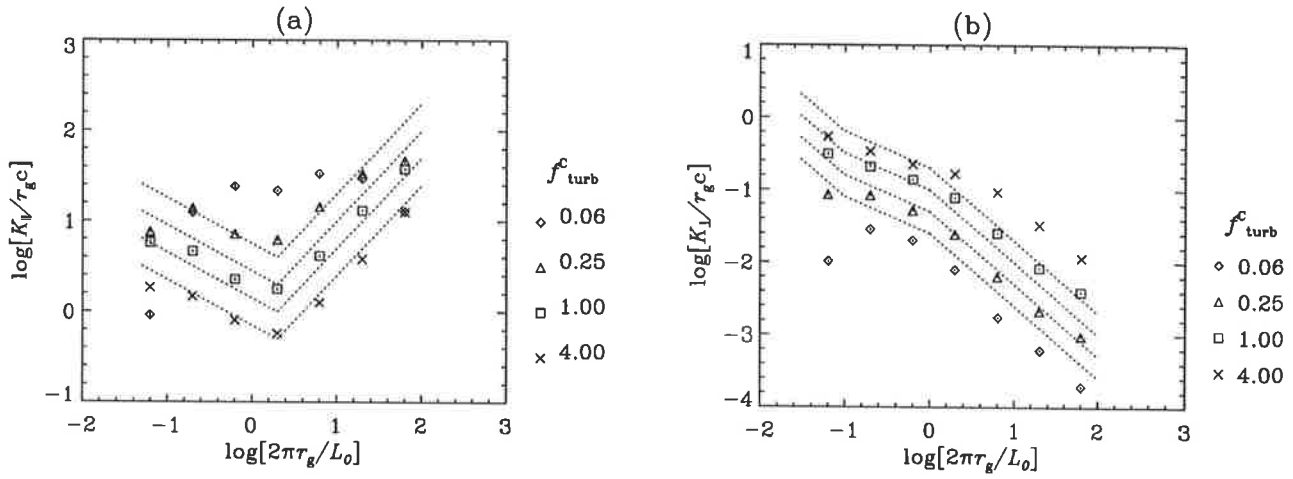

Figure 4.7: Diffusion tensor plot in logarithmic scale. Dotted curves from Casse et al. for some f^C_{turb} values. (a) $\frac{K_\parallel}{r_g c}$ versus $\frac{2\pi r_g}{L_0}$ plot. (b) $\frac{K_\perp}{r_g c}$ versus $\frac{2\pi r_g}{L_0}$.

also investigated. The range of angles is defined schematically in Figure 4.8. The upper angle range shown in Figure 4.8 (b) is $(\theta_1 < \theta_U < \theta_2)$, and the lower angle range shown in Figure 4.8 (c) is $(0 > \theta_L > \theta_1,\ \theta_2 < \theta_L < \pi)$.

Figures 4.9, 4.10, 4.11 and 4.12 show the distributions of the final proton distance normalized by $\sqrt{2ct}$, where t is the final time: (a) is x-component and (b) is z-component. The solid curves in Figures 4.9, 4.10, 4.11 and 4.12 represents the Gaussian distribution based on the position of the particles. For example of x-component, the Gaussian curve $f(x)$ is given by

$$f(x) = \frac{1}{\sqrt{2\pi K_x}} \exp\Big[\frac{x^2}{2K_x}\Big], \tag{4.2.29}$$

where K_x is x-component of diffusion tensor calculated by Equations 4.2.25 and 4.2.26. The dotted histogram represents the distribution of the particles starting with upper injection angle. The mean magnetic field $\vec{B}_0$ lies in z-direction. Thus the dotted histograms in Figures 4.9, 4.10, 4.11 and 4.12 correspond to the angular range of protons at injection as in Figure 4.8 (b).

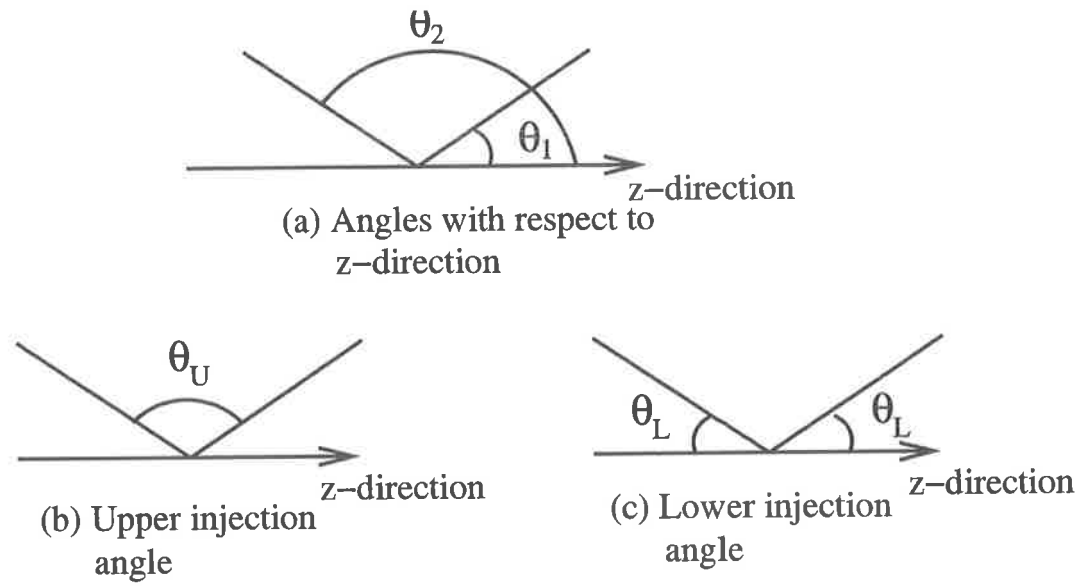

Figure 4.8: Schematic diagram of the range of angle with respect to z-direction when protons were injected at the origin: The mean magnetic field $\vec{B}_0$ lies in the z-direction. (a) Angles θ_1 and θ_2 with respect to z-direction. (b) Upper injection angle range θ_U. (c) Lower injection angle range θ_L.

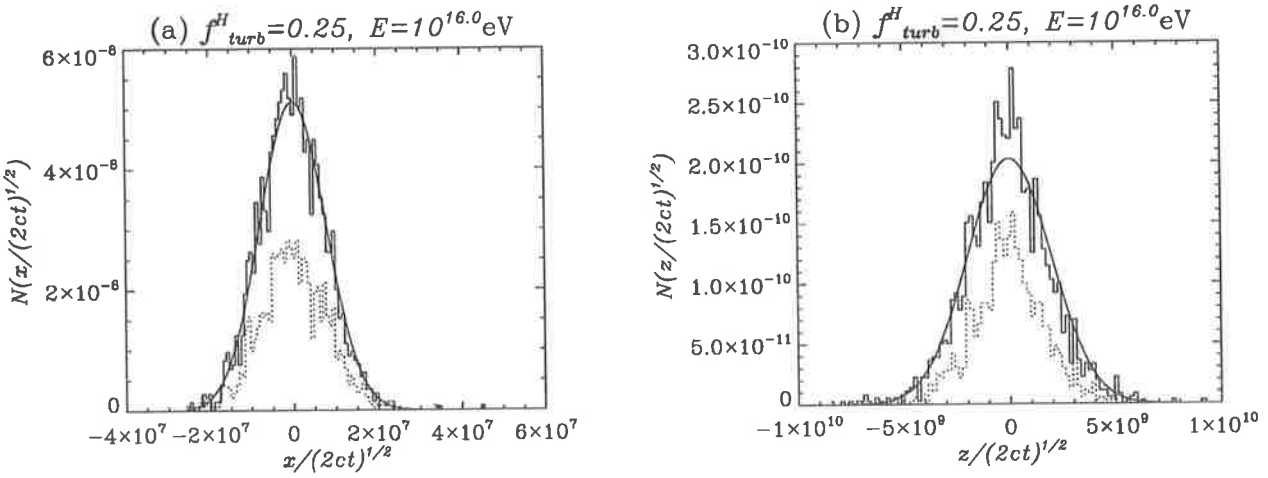

Figure 4.9: Distributions of the proton position from the origin: (a) x-component. (b) z-component. $f_{turb} = 0.25$ and $E = 10^{16}$eV. The solid lined histogram shows the distribution for all injection angle range and the dotted histogram shows the distribution for upper injection angle range.

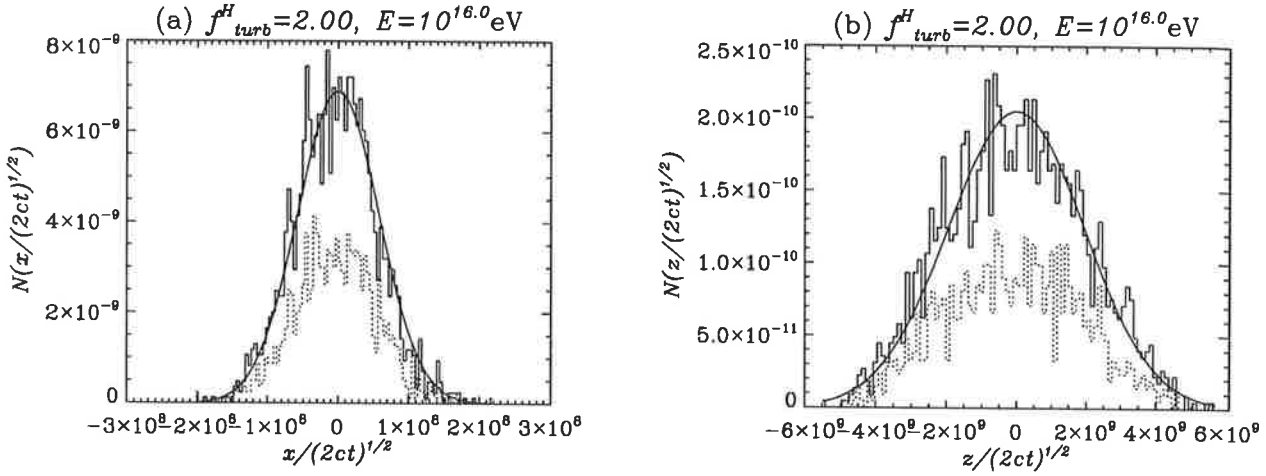

Figure 4.10: Distributions of the proton position from the origin: (a) x-component. (b) z-component. $f_{turb} = 2$ and $E = 10^{16}$eV. The solid lined histogram shows the distribution for all injection angle range and the dotted histogram shows the distribution for upper injection angle range.

Figures 4.9 and 4.10 show the distribution for $E = 10^{16}$eV. In Figure 4.9 the turbulence parameter f_{turb} is 0.25, so the effect of the irregular magnetic field $\delta\vec{B}$ is small, whereas in Figure 4.10, which is for $f_{turb} = 2$, the effect at $\delta\vec{B}$ is large and the total magnetic field $\vec{B}_{total}$ appears to be a more random. The distribution for high energy protons obeys the Gaussian distribution, which is defined by Equation 4.2.29. This is expected because the solution of the diffusion equation 1.4.1 is a Gaussian. It is also noticed that the x-component of the proton's position is concentrated near the origin in the case of $f^H_{turb} = 0.25$. On the other hand, if f^H_{turb} is 2, x-component of the proton position distribution spreads out due to the highly disordered magnetic field.

However, in the low energy regime, the position distribution of protons is different from the distribution in the high energy case. Figures 4.11 and 4.12 show the position distribution for $E = 10^{13}$eV. Figure 4.11 shows the position distribution of 10^{13}eV protons for the $f_{turb} = 0.25$ case. Figure 4.11 shows the position distribution of 10^{13}eV protons

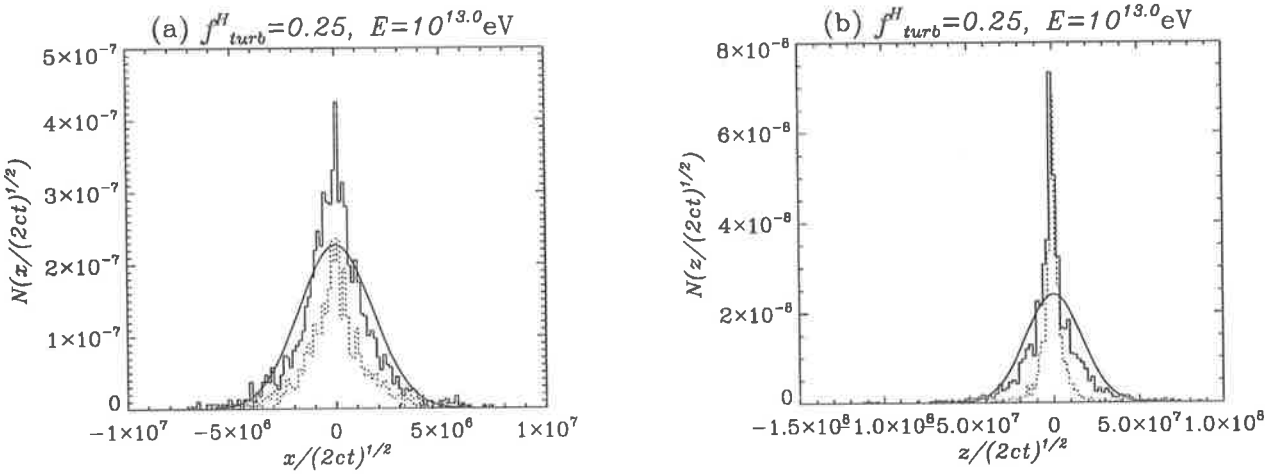

Figure 4.11: Distributions of the proton position from the origin: (a) x-component. (b) z-component. $f_{turb} = 2$ and $E = 10^{13}$eV. The solid lined histogram shows the distribution for all injection angle range and the dotted histogram shows the distribution for upper injection angle range.

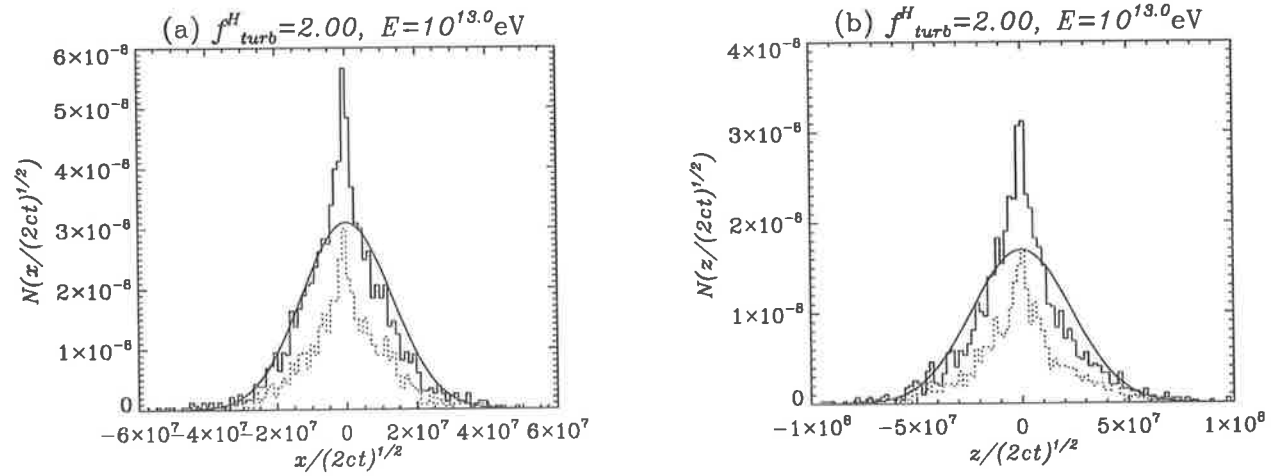

Figure 4.12: Distributions of the proton position from the origin: (a) x-component. (b) z-component. $f_{turb} = 2$ and $E = 10^{13}$eV. The solid lined histogram shows the distribution for all injection angle range and the dotted histogram shows the distribution for upper injection angle range.

for the $f_{turb} = 2$ case. In Figures 4.11 and 4.12, there exists a high peak near the origin, in particular the z-component of the position distribution shown in Figure 4.11 (a) has an acute peak. The dotted histograms in Figures 4.11 and 4.12 also show acute peaks at the origin. This implies that protons with low energy have tendency to remain close to the same position and to diffuse more slowly in turbulent magnetic fields. Figure 4.13 shows a schematic diagram of a 10^{13}eV proton's trajectory along the turbulent magnetic fields. If the pitch angle of the proton is high due to the high incident angle shown in Figure 4.8 (b) and insufficient energy to escape from the magnetic fields, the proton tends to be trapped by the magnetic fields and to move circularly. Furthermore, if the turbulent parameter f_{turb} is small and the magnetic turbulence is weak, the proton also tends to move circularly at the origin. For these reason, the dotted histogram in Figure 4.11 (a) shows a high peak at the origin. On the other hand, if the turbulence parameter f_{turb} is large and the magnetic fields become more random, the chance to escape from the origin will increase. Therefore in Figure 4.12 (a), the distribution has slightly smaller peak than the distribution in Figure 4.11 (a).

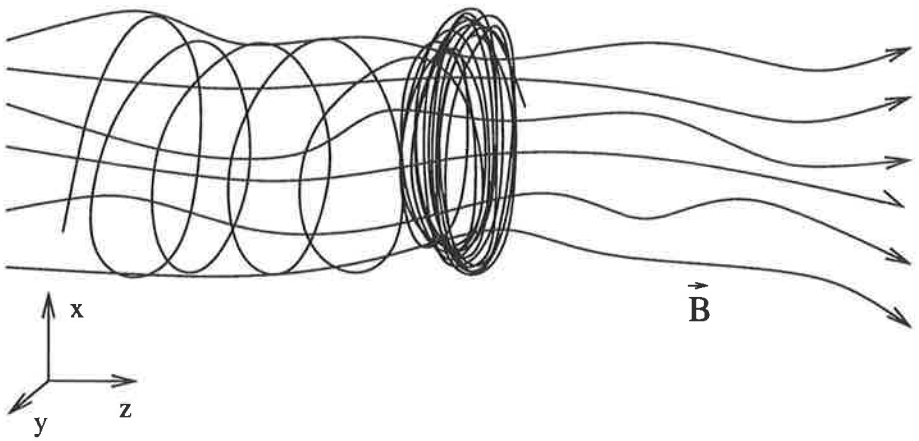

Figure 4.13: Schematic diagram of the trajectory of proton with low energy ($E \geq 10^{13}$ eV) along the turbulent magnetic fields in the case of high pitch angle.

4.3 Summary and Conclusion

The simulation proposed by Giacalone and Jokipii [9] is described in this chapter. They used the superposition of plane waves to create the irregular magnetic field $\delta\vec{B}(\vec{r})$. However, the simpler, but equivalent, version of superposition of plane waves, shown in Equation 4.2.6 was used for $\delta\vec{B}(\vec{r})$.

The trajectories of the cosmic rays are presented in Section 4.2.2. The Figures 4.2 and 4.3 show examples of low energy cosmic ray ($E = 10^{13}$eV) trajectories. The Figures 4.4 and 4.5 show examples of high energy cosmic ray ($E = 10^{16}$eV) trajectories. According to the Figures from 4.2 to 4.5, it seems that the cosmic ray diffusion is dependent upon the particle energy. It also depends on the turbulence level defined by Equation 4.2.24.

In Section 4.2.3, the calculation of diffusion tensors was presented. The results using the Giacalone and Jokipii method are compared with those of the Honda's simulation and the Casse et al. simulation. Figures 4.6 and 4.7 show the results are in reasonable agreement at high energy with the results of Honda and the Casse et al. simulation. However, the diffusion tensors are different in the low energy regime. This is perhaps due to different methods. The big difference between Giacalone and Jokipii method and the method of Honda and Casse et al. is the method of creating the turbulent magnetic fields. Honda and Casse et al. used a three-dimensional grid space, whereas Giacalone and Jokipii did not use any grid space. In the Honda and Casse et al simulations, magnetic field interpolation was implemented. This could be a cause of the difference at low energy. The sensitivity to L_{min}, the minimum grid spacing, and the size of time step could also be the reason for the difference between the results of using Giacalone and Jokipii method, and the other two methods.

In conclusion, the modified Giacalone and Jokipii method used here is adequate in the

high energy regime, and therefore this method will be used to investigate shock acceleration phenomena.

Chapter 5

Application to shock acceleration

In Chapters 3 and 4 I discuss two different simulation methods for cosmic ray diffusion in turbulent magnetic fields. In these two simulations by Honda [11], and by Giacalone and Jokipii [7] [8] [9], the turbulent magnetic fields are assumed to be static, and this approximation is fine for propagation of cosmic rays exert in regions where cosmic ray acceleration takes place. The magnetic fields in supernova shock phenomenon are an example of non-static magnetic fields, and so the supernova phenomenon is a possible acceleration source of Galactic cosmic rays.

In this chapter I use the simulation method proposed by Giacalone and Jokipii [7] [8] [9] and applied it to shock acceleration, and so Chapter 5 describes an application of diffusion simulation methods used for static magnetic fields to a real astronomical phenomena.

5.1 Mechanisms of cosmic ray acceleration

The cosmic ray acceleration process has been studied since Fermi first proposed the original theory of acceleration in 1949 [6]. This section is mainly based on Chapter 21 of "High Energy Astrophysics" by M.S. Longair [19].

Section 5.1.1 is a brief introduction of particle acceleration. This section describes how the electromagnetic fields are associated with the cosmic ray acceleration mechanism. Section 5.1.2 outlines Fermi's original theory of particle acceleration known as Second Order Fermi Acceleration. Section 5.1.3 presents the problems in Second Order Fermi Acceleration that require a new theory to be developed to solve these problems and to adequately explain cosmic ray acceleration. In Section 5.1.4, the modified Fermi theory of particle acceleration, known as First Order Fermi Acceleration or diffusive shock acceleration, is explained. The modifications of Fermi's original theory were made in the late 1970's. Section 5.1.4 also presents the theory as described by Bell in 1978 [3]. In Section 5.1.5 I discuss how the cosmic ray power-law spectrum arises in the First Order Fermi Acceleration.

5.1.1 Particle acceleration

Equation 5.1.1 describes the motion of a charged particle in electric and magnetic fields.

$$\frac{d}{dt}(\gamma m\vec{v}) = e(\vec{E} + \vec{v} \times \vec{B}) \tag{5.1.1}$$

The right hand side of Equation 5.1.1 is called the Lorentz force. In static magnetic fields, the fields may change the direction of the particle but no work is done on the particle. Magnetic fields only change the direction of the particle. However, if the magnetic fields are time dependent, induced electric fields are produced according to Maxwell's equation (Faraday's law),

$$\vec{\nabla} \times \vec{E} = -\frac{\partial \vec{B}}{\partial t} \tag{5.1.2}$$

In most astrophysical environments, static electric fields cannot be maintained because ionised gases have very high electrical conductivity. Therefore, astrophysical acceleration

mechanisms can only be associated either with dynamic electric fields, or with time-varying magnetic fields.

5.1.2 Second Order Fermi Acceleration

This section considers Fermi's original theory of particle acceleration. In 1949 Fermi [6] proposed a particle acceleration process in which acceleration resulted from particles colliding with clouds in the interstellar medium.

To make calculation simple, this theory assumed the cloud to be a mirror, so a collision between a particle and a mirror is elastic. The θ was defined as a angle that a particle's initial direction with respect to the normal to the cloud's surface, as shown in Figure 5.1. Supposing the cloud is infinitely massive so that its velocity V is not affected by the collision, then the particle energy in cloud frame is

$$E' = \gamma_V (E + Vp\cos\theta) \tag{5.1.3}$$

where γ_V is the gamma factor in cloud frame, E and p are the particle energy and momentum in the frame outside of the cloud, and β_V is the cloud velocity over the speed of light, hence

$$\gamma_V = \frac{1}{\sqrt{1-\beta_V^2}} \quad \text{and,} \quad \beta_V = \frac{V}{c}$$

The z-component of the relativistic three momentum in the centre of momentum frame is

$$p'_z = \gamma_V \left(p_z + \frac{\beta_V E}{c}\right) \tag{5.1.4}$$

In the collision, the particle's energy is conserved, and its momentum in the z-direction is reversed. Therefore, the particle's energy in the observer's frame is

$$E'' = \gamma_V (E' + Vp'_z) \tag{5.1.5}$$

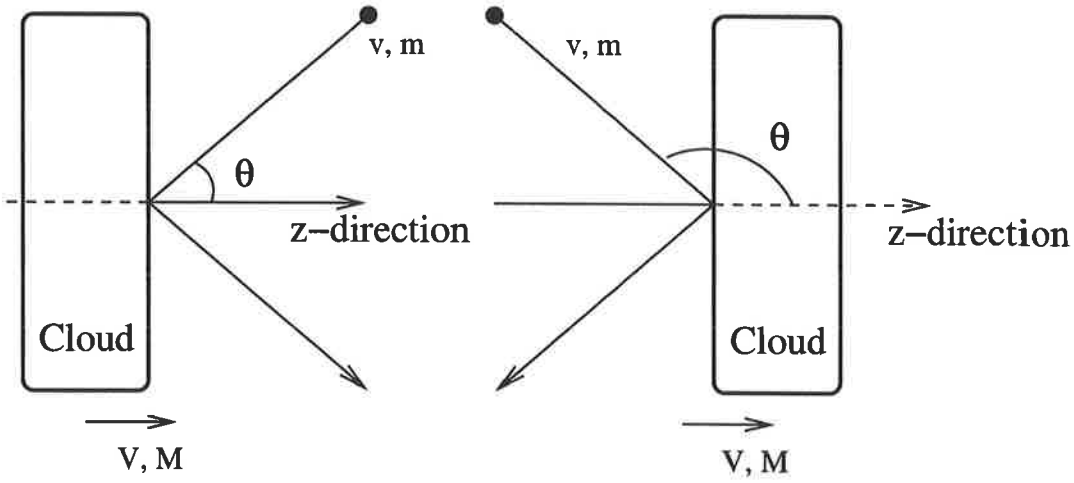

(a) Head–On type collision (b) Following type collision

Figure 5.1: The schematic diagram of the collision between relativistic particle and interstellar cloud. (a) Head-on type collision. (b) Following type collision. v and m are the velocity and mass of the relativistic particle. V and M are the velocity and mass of the cloud.

Using $p_z/E = v\cos\theta/c^2$, Equations 5.1.3 and 5.1.4 become

$$E' = \gamma_V(E + Vp_z) = \gamma_V\left(E + \frac{v\beta_V E\cos\theta}{c}\right) \tag{5.1.6}$$

$$p'_z = \gamma_V(p_z + \frac{\beta_V E}{c}) = \gamma_V\left(\frac{vE\cos\theta}{c^2} + \frac{\beta_V E}{c}\right) \tag{5.1.7}$$

Substituting Equations 5.1.6 and 5.1.7 into Equation 5.1.5, Equation 5.1.5 becomes

$$\begin{aligned} E''(\beta_V) &= \gamma_V\left[\gamma_V\left(E + \frac{v\beta_V E\cos\theta}{c}\right) + V\gamma_V\left(\frac{vE\cos\theta}{c^2} + \frac{\beta_V E}{c}\right)\right] \\ &= \gamma_V^2 E\left(1 + \frac{2v\beta_V\cos\theta}{c} + \beta_V^2\right) \end{aligned} \tag{5.1.8}$$

Therefore, the energy change ΔE becomes

$$E'' - E = \Delta E = \frac{2\beta_V v\cos\theta}{c} + \beta_V^2 \tag{5.1.9}$$

Figure 5.1 shows the collision path between a relativistic particle and the interstellar cloud. In Figure 5.1 v and m are the velocity and mass of the relativistic particle. V and M are the velocity and mass of the cloud. The probability of a collision at angle θ is proportional to $v + V\cos\theta$ in the case of the head-on type collision ((a) of Figure 5.1),

whereas in a following type collision, the probability is proportional to $v - V\cos\theta$ ((b) of Figure 5.1). Since the particle is relativistic and $v \approx c$, the probability of the collision at angle θ range from 0 to π and is proportional to $\gamma_V(1 + \beta_V \cos\theta)$. The probability of the pitch angle is proportional to $\sin\theta d\theta (= -d(\cos\theta))$. Therefore the average of the first term in Equation 5.1.9 in the relativistic limit ($v \rightarrow c$) is

$$\begin{aligned} \langle 2\beta_V \cos\theta \rangle &= 2\beta_V \frac{\int_{-1}^{1} \cos\theta[1 + \beta_V \cos\theta] d(\cos\theta)}{\int_{-1}^{1} [1 + \beta_V \cos\theta] d(\cos\theta)} \\ &= 2\beta_V \frac{\frac{2}{3}\beta_V}{2} = \frac{2}{3}\beta_V^2 \end{aligned} \tag{5.1.10}$$

The average energy gain per collision in the relativistic limit is,

$$\frac{\langle \triangle E \rangle}{E} = \frac{2}{3}\beta_V^2 + \beta_V^2 = \frac{5}{3}\beta_V^2 \tag{5.1.11}$$

The increase of energy is a factor of β_V^2. This is the Fermi's original theory of particle acceleration and called the "Second Order Fermi Acceleration".

5.1.3 Problems in Second Order Fermi Acceleration

There are several difficulties in Fermi's original theory as a mechanism for accelerating the Galactic cosmic rays:

1. The random velocities of interstellar clouds in the Galaxy are very small in comparison with the velocity of light, namely $\beta_V \leq 10^{-4}$.

2. The original theory estimates the mean free path of the cosmic rays in the interstellar medium to be the order of 1pc. This suggests that the number of collisions would be roughly one per year, resulting in very slow gain of energy by the particle.

3. The original calculation does not consider the effect of energy loss upon the acceleration process. Ionisation losses in particular prevent the acceleration of particles

from low energy. If the acceleration mechanism is to be effective, the particles must either be injected into the acceleration region with energies greater than that corresponding to the maximum energy loss rate, or else the initial acceleration process must be sufficiently rapid to overcome the energy loss.

4. The theory does not explain why the exponent of the energy spectrum should be roughly 2.5 everywhere.

In particular, Fermi's original theory is inadequate to explain the acceleration of particles to a high energy.

5.1.4 First Order Fermi Acceleration (Diffusive Shock Acceleration)

Many researchers in the late 1970's attempted to describe a more efficient particle acceleration process. The following model proposed by Bell in 1978 [3] has been found to be useful in addressing the limitations outlined in Section 5.1 3.

According to Bell [3], Figure 5.2 illustrates the vicinity near a shock front for a strong shock case as in the case of a supernova explosion.

1. In the shock frame, the shock front is stationary, and the ratio of the upstream V_u to the downstream velocity V_d for a strong shock is

$$\frac{V_u}{V_d} = \frac{\gamma + 1}{\gamma - 1}, \tag{5.1.12}$$

where γ is the ratio of specific heat of gas. For a monatomic and fully ionised plasma in the case of supernova, $\gamma = 5/3$ and then the downstream velocity is one fourth of the upstream velocity.

$$V_d = \frac{1}{4} V_u. \tag{5.1.13}$$

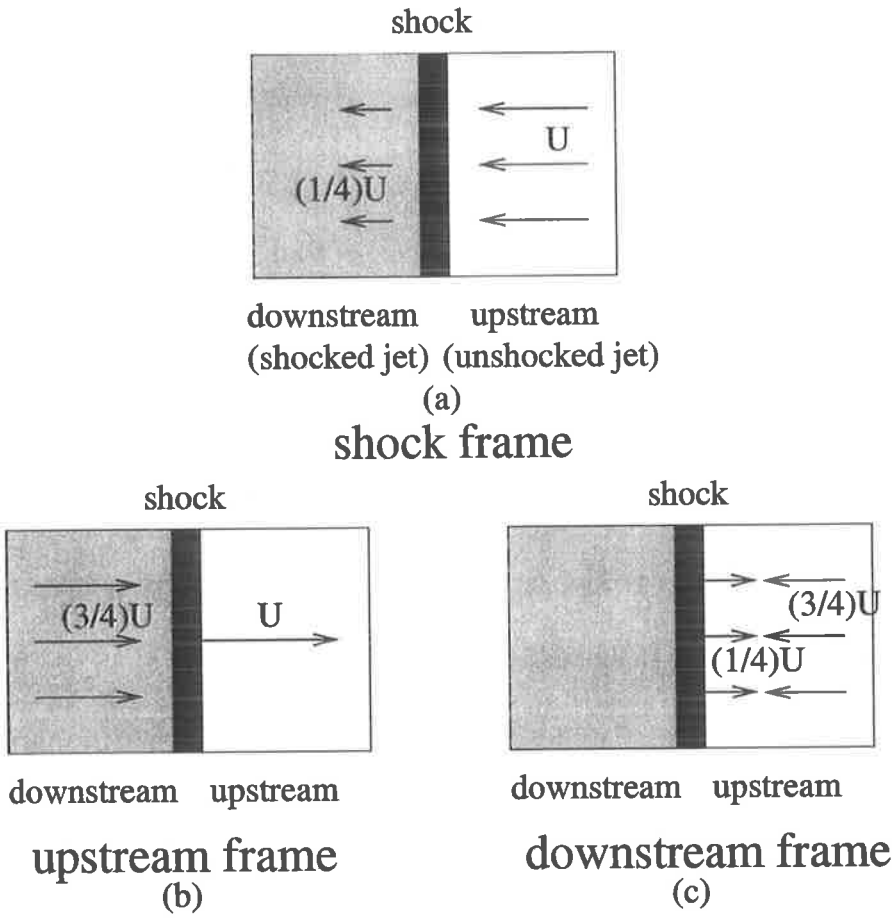

Figure 5.2: The schematic diagram of shock phenomenon. (a) Shock front frame. (b) Upstream frame. (c) Downstream frame.

2. In the upstream (unshocked region) frame namely Figure 5.2 (b), the downstream gas moves at $\frac{3}{4}U$ (U : shock front velocity) compared to the upstream gas velocity. When a high energy particle crosses the shock front and enters the downstream region, it gains energy of the order of $\sim \frac{U}{c}$ as a result of collisionless scattering. Once the particles enter the downstream region, they are then scattered by turbulent magnetic fields, so the velocity distributions of the particles become isotropic.

3. In the downstream (shocked region) frame of Figure 5.2, the gas in upstream region moves toward the shock front at velocity, $\frac{3}{4}U$. Once the particles in the downstream frame enter the upstream region, they feel the upstream gas moving against them with the same velocity, $\frac{3}{4}U$. As a result, when the particle crosses the shock front, it also obtains the same amount of energy increase $\frac{\triangle E}{E} \sim \frac{U}{c}$.

According to the model proposed by Bell [3], the high energy particles gain energy whenever it crosses the shock front. In this model there are mainly head-on type collisions, and so the particles gain energy of the order $\sim \frac{U}{c}$, whereas in Fermi's original theory there are both head-on type and following type collisions with almost equal frequency.

The following is the derivation of the average energy increase when the particle crosses from the upstream to the downstream region. If the gas in the downstream region moves toward the particle at velocity $V(= V_{down}) = \frac{3}{4}U$, then the particle's energy when it passes into the downstream region is

$$E' = \gamma_V (E - p_z V) \tag{5.1.14}$$

where the z-coordinate is perpendicular to the shock front. It is assumed that the shock is non-relativistic, namely

$$V \ll c \quad \text{and} \quad \gamma_V = 1 \tag{5.1.15}$$

However the particles are relativistic, so

$$E = pc \quad \text{and} \quad p_z = -\frac{E}{c}\cos\theta \tag{5.1.16}$$

Therefore, the energy change ΔE is

$$\triangle E = pV\cos\theta \quad , \quad \frac{\triangle E}{E} = \beta_V \cos\theta \tag{5.1.17}$$

The probability of a particle crossing the shock front with angle θ can be derived. The number of particles within the angles of θ to $\theta + d\theta$ is proportional to $\sin\theta d\theta$. The rate at which the particles approach the shock front is proportional to $c\cos\theta$. From the above result, the probability of a particle crossing the shock front is proportional to $\sin\theta\cos\theta d\theta$. Therefore, the probability distribution function over the angle range from 0 to $\frac{\pi}{2}$ becomes

$$p(\theta) = 2\sin\theta\cos\theta d\theta \tag{5.1.18}$$

Finally the average gain in energy on crossing the shock front is

$$\begin{aligned}\frac{\langle\triangle E\rangle}{E} &= \int_0^{\pi/2} p(\theta)\frac{\triangle E}{E}d\theta \\ &= \beta_V \int_0^{\pi/2} 2\cos^2\theta\sin\theta d\theta \\ &= \frac{2}{3}\beta_V\end{aligned} \tag{5.1.19}$$

The particle gains energy when it crosses the shock front, so the average energy increase for the return trip is

$$\frac{\langle\triangle E\rangle}{E} = \frac{4}{3}\beta_V = \frac{U}{c} \tag{5.1.20}$$

The average increase in energy of the particle is proportional to β_V. This is called the First Order Fermi Acceleration and is a more efficient acceleration model than the Second Order Fermi Acceleration.

5.1.5 Power-law Spectrum

The power-law spectrum can be explained by the result from the First Order Fermi Acceleration, and the derivation of the cosmic ray energy spectrum follows.

The average energy of the particle after k-th crossing of the shock front is expressed as

$$E = \alpha^k E_0 \tag{5.1.21}$$

where α is small fractional change in particle energy, and E_0 is the initial particle energy. The number of the particles with energies $E = \alpha^k E_0$ after k collisions is

$$N = N_0 P_{\rm ret}^k \tag{5.1.22}$$

where $P_{\rm ret}$ is the probability of the particle returning to the upstream region after one shock crossing (probability of returning). Taking natural logarithms of both Equations 5.1.21 and 5.1.22, and eliminating k.

$$\frac{N}{N_0} = \left(\frac{E}{E_0}\right)^{\ln P_{\rm ret}/\ln \alpha} \tag{5.1.23}$$

From equation 5.1.23, the power-law spectrum is derived,

$$N(E)dE = \text{cons't} \times E^{-1+(\ln P_{\rm ret}/\ln \alpha)} dE \tag{5.1.24}$$

The next step is to calculate the index $(\ln P_{\rm ret}/\ln \alpha)$ from the first order Fermi acceleration result. Starting from the average of the fractional energy increase,

$$\frac{\langle \triangle E \rangle}{E} = \frac{4}{3}\beta_v \tag{5.1.25}$$

and using $E - E_0 = \langle \triangle E \rangle$, α becomes

$$\alpha = \frac{E}{E_0} = 1 + \frac{4}{3}\beta_v \tag{5.1.26}$$

The probability of returning $P_{\rm ret}$ can be derived as follows. For an isotropic distribution, the flux of particles crossing the shock front is $\frac{1}{4}Nc$, where N is the number density of

particles. Once the particles enter the shocked (downstream) region, the particles are removed from that region. The rate at which the particles are transported from the shocked region is $NV = \frac{1}{4}NU$, where U is shock front velocity. Therefore, the fraction of the particles lost downstream per shock crossing (escape probability: $P_{\rm escape}$)

$$P_{\rm escape} = \frac{\frac{1}{4}NU}{\frac{1}{4}Nc} = \frac{U}{c}. \tag{5.1.27}$$

Finally, the probability of returning to the shock $P_{\rm ret}$ becomes

$$P_{\rm ret} = 1 - P_{\rm escape} = 1 - \frac{U}{c} \tag{5.1.28}$$

Then, taking logarithm of both $P_{\rm ret}$ and α, and using the approximation, $\ln x \approx 1 + x$,

$$\ln P_{\rm ret} = \ln\left(1 - \frac{U}{c}\right) \approx -\frac{U}{c}$$
$$\ln \alpha = \ln\left(1 + \frac{4}{3}\beta_V\right) \approx \frac{U}{c} \qquad \left(\because \frac{U}{c} = \frac{4}{3}\beta_V\right)$$

Therefore, the $(\ln P_{\rm ret}/\ln \alpha)$ becomes

$$\frac{\ln P_{\rm ret}}{\ln \alpha} = \frac{(-U/c)}{(U/c)} = -1 \tag{5.1.29}$$

Finally, the differential energy spectrum of the particle is obtained,

$$N(E)dE \propto E^{-1+(-1)}dE = E^{-2}dE \tag{5.1.30}$$

The observed energy spectrum is in the range approximately from -3.2 to -2.5, which is different from the spectrum above because of energy-dependent cosmic ray diffusive transport in our Galaxy (e.g. Leaky Box Model).

The theory of First Order Fermi Acceleration succeeded in explaining cosmic ray acceleration of supernova explosion and other shock phenomena. It also can explain the cosmic ray energy spectrum, and so the theory has been widely accepted in the field of astrophysics. In the next section I will describe the numerical simulation of cosmic ray diffusive shock acceleration by using the simulation method of Giacalone and Jokipii [7] [8] [9] for the diffusion.

5.2 Simulating Shock Acceleration Process

This section presents the application of the simulation method of Giacalone and Jokipii to cosmic ray shock acceleration and discusses the result from the simulation.

5.2.1 Creating shock environment

This section describes how to simulate the shock phenomenon. In Chapters 3 and 4 I discussed high energy cosmic ray (proton) diffusion in turbulent magnetic fields. In previous simulations by Honda [11], Giacalone and Jokipii [7] [8] [9], the magnetic fields are "static". However, in the shock phenomena, the magnetic fields are time varying and due to this phenomena, relativistic particles may gain energy.

In the simulation of shock acceleration, it is assumed that there are two regions, a downstream region which contains shocked plasma and an upstream region which contains unshocked plasma. The shock front separates them. Each region has its own frame of reference. Therefore, once a cosmic rays crosses the shock front, Lorentz transformation to the other frame must be considered. Returning to the original frame after scattering causes an energy increase in the cosmic rays.

Figure 5.3 shows a schematic diagram of the shock at $t = 0$ sec in the shock simulation. The shock front starts at the origin for convenience of calculation. Then it moves toward the $+z$-direction with constant speed, $U = 0.03 \times c = 9.0 \times 10^6$ m/s, where c is the speed of light; this is typical supernova shock speed. At the same time, a relativistic proton starts moving and crosses the shock front, Figure 5.4 shows the range of the injection angle. The proton injection angles are randomly sampled from

$$-1 \leq \cos\theta \leq 0, \qquad 0 \leq \phi < 2\pi, \tag{5.2.1}$$

where θ is the direction angle with respect to z-axis as shown in Figure 5.4 (a), and ϕ is

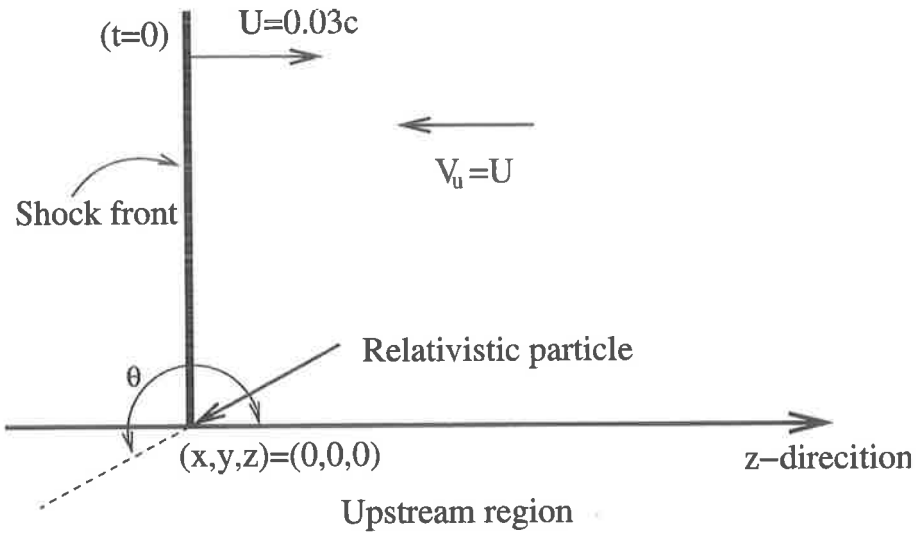

Figure 5.3: The beginning of the shock simulation. The shock front starts at $z = 0$ and moves toward $+z$-direction. The shock front speed is $U = 0.03 \times c$. Protons start at origin with injection angle range defined by Equation 5.2.1.

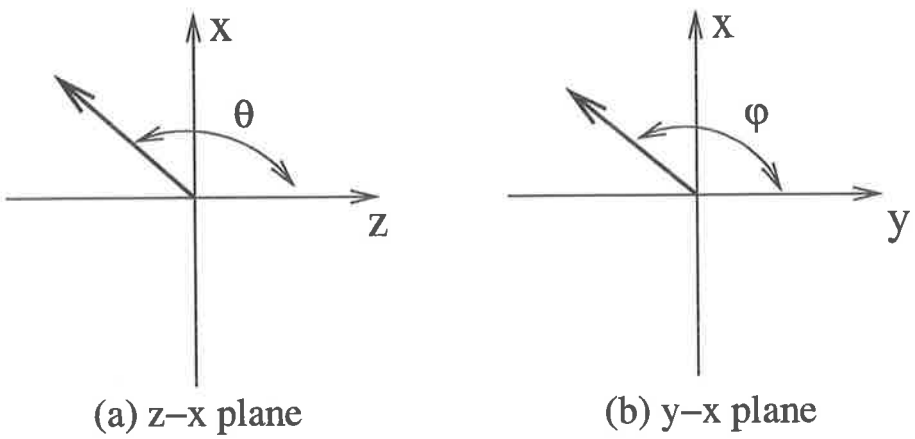

Figure 5.4: Injection angle. (a) z-x plane. The range of θ is $-1 \leq \cos\theta \leq 0$. (b) y-x plane. The range of ϕ is $0 \leq \phi < 2\pi$.

the direction angle with respect to y-axis as shown in Figure 5.4 (b). If the direction of the shock front is the same as the direction of the mean magnetic field $\vec{B}_0$ of the total turbulent magnetic field, this shock is called a 'Parallel Shock'. If the direction of the shock front is perpendicular to the direction of $\vec{B}_0$, this shock is called a 'Perpendicular Shock'.

In the downstream region, because it is a shocked region, the plasma gas and the magnetic fields are compressed. Therefore, a special treatment is necessary for simulating

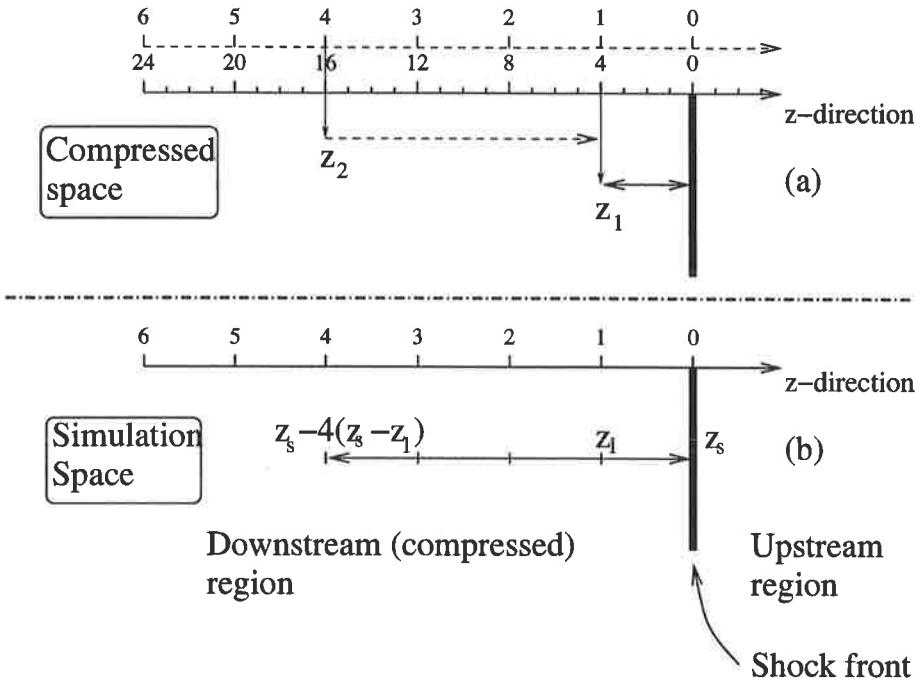

Figure 5.5: The schematic diagram of the proton position in downstream region. (a) Proton position z_1 in the compressed scale and proton position z_2 in the uncompressed scale. (b) Proton position in the simulation space. The position $z_s - 4(z_s - z_1)$ was named 'Effective Position', where z_s is the shock front position.

the downstream region of the shock. In the shock frame of reference, the plasma speed in upstream region is the shock speed U, which is four times faster than downstream plasma gas. This leads to the downstream region plasma being compressed into $\frac{1}{4}$ of its scale in the z-direction. Figure 5.5 shows a schematic diagram of the proton position in the downstream region. Figure 5.5 (a) describes the proton position in the compressed downstream space. The dashed lined scale in Figure 5.5 (a) is the scale of uncompressed space and the solid lined scale is the scale of compressed space. Supposing that the proton entering the downstream region moves to the position z_1, the position z_1 would correspond to position z_2 in the uncompressed space as shown in Figure 5.5. This means that the magnetic field at position z_1 should be $\vec{B}(z_2)$ compressed in the z-direction.

Figure 5.5 (b) shows how to express positions z_1 and z_2 in the simulation space. Assuming z_1 is a position of proton in Figure 5.5 (b), z_2 in Figure 5.5 (a) can be expressed as $z_{\text{shock}} - 4(z_{\text{shock}} - z_1)$ shown in Figure 5.5 (b), where z_{shock} is the position of the shock

front. This was named the 'Field Position', $\vec{r}_{\text{field}}$ and the components of the field position in the downstream region are

$$\begin{cases} x_{\text{field}} = x \\ y_{\text{field}} = y \\ z_{\text{field}} = z_{\text{shock}} - 4(z_{\text{shock}} - z) \end{cases} \tag{5.2.2}$$

The magnetic field at position $\vec{r} = (x,\ y,\ z)$ $\vec{B}^U(\vec{r}_{\text{field}})$ is appropriately compressed, where $\vec{B}^U(\vec{r}_{\text{field}})$ is the magnetic field that would have been present at $\vec{r}_{\text{field}}$ before the shock arrived. The strength of the magnetic field that the proton perceives also changes due to the compression of the plasma in the downstream region. The scale in the downstream region is compressed into $\frac{1}{4}$ of its original scale in the z-direction. Thus the distance in the z-direction between two magnetic field lines is four times smaller if the plasma were not compressed in the z-direction. This leads to the x- and y-component of the magnetic field becoming four times larger than the original magnitude. Equivalent expression of the compressed magnetic field at position $\vec{r} = (x,\ y,\ z)$ in the simulation space can be done by expanding x- and y-components of the magnetic field by factor of four as shown in Figure 5.6. Therefore when the proton enters the downstream region and reaches the position $\vec{r} = (x,\ y,\ z)$, the magnetic field that affects the proton at position $\vec{r}$ is

$$\vec{B}(\vec{r}) = 4B_x^U(\vec{r}_{\text{field}})\hat{x} + 4B_y^U(\vec{r}_{\text{field}})\hat{y} + B_z^U(\vec{r}_{\text{field}})\hat{z} \tag{5.2.3}$$

The following sections will explain how to draw the trajectory of relativistic proton in the shock environment and discusses the characteristics of the proton trajectories.

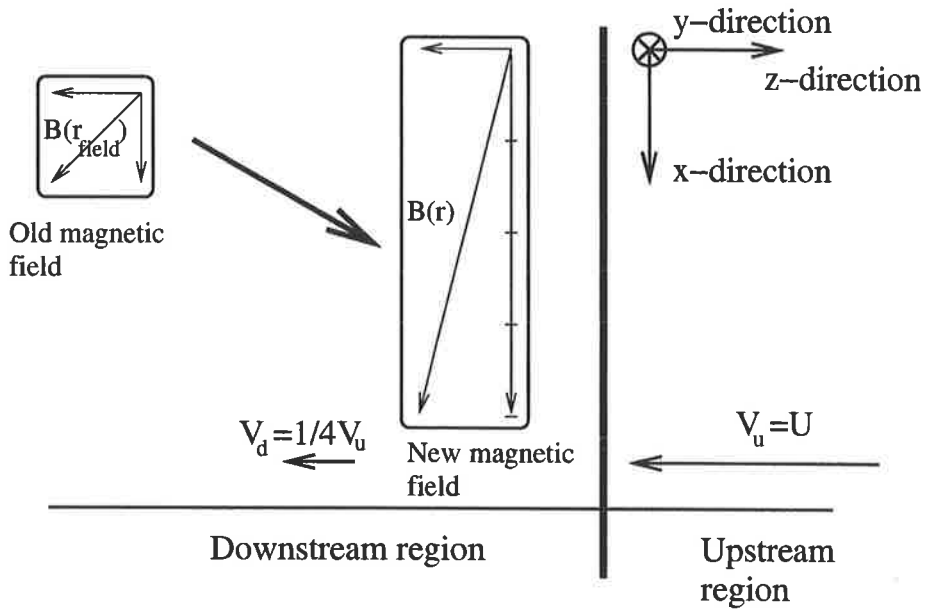

Figure 5.6: The schematic diagram of the downstream magnetic field in the simulation space. The x- and y-components of the magnetic field $\vec{B}(\vec{r}_{\rm field})$ are expanded to four times of the original x- and y-components.

5.2.2 Drawing the trajectories of relativistic protons

The method of Giacalone and Jokipii for simulation of turbulent magnetic field was applied to shock acceleration simulations. In the simulation, the initial data for the particle and the magnetic fields were the same as those in the Giacalone and Jokipii simulation. A relativistic proton in the energy range 10^{13}eV$< E < 10^{16}$eV was injected. The corresponding gyroradius range for this energy range is 0.01pc$< r_{gyro} <$ 10pc for a mean magnetic field $B_0 = 10^{-10}$T. Step size $c\triangle t$ is as usual $(0.01 \times r_{gyro})$. The turbulent magnetic field consists of a mean magnetic field B_0 and an irregular magnetic field δB. The mean magnetic field strength is assumed to be 1.0×10^{10}T and the irregular magnetic field is a Kolmogorov type magnetic field. The turbulence parameter f^H_{turb} in this simulation is

$$f^H_{turb} = \frac{|\delta \vec{B}_{rms}|}{B_0} = \frac{2^n}{4}, \qquad (n = 0,\ 1,\ 2,\ 3) \tag{5.2.4}$$

and this is the ratios of the r.m.s. value of the irregular magnetic field $\delta \vec{B}_{rms}$ to mean magnetic field B_0.

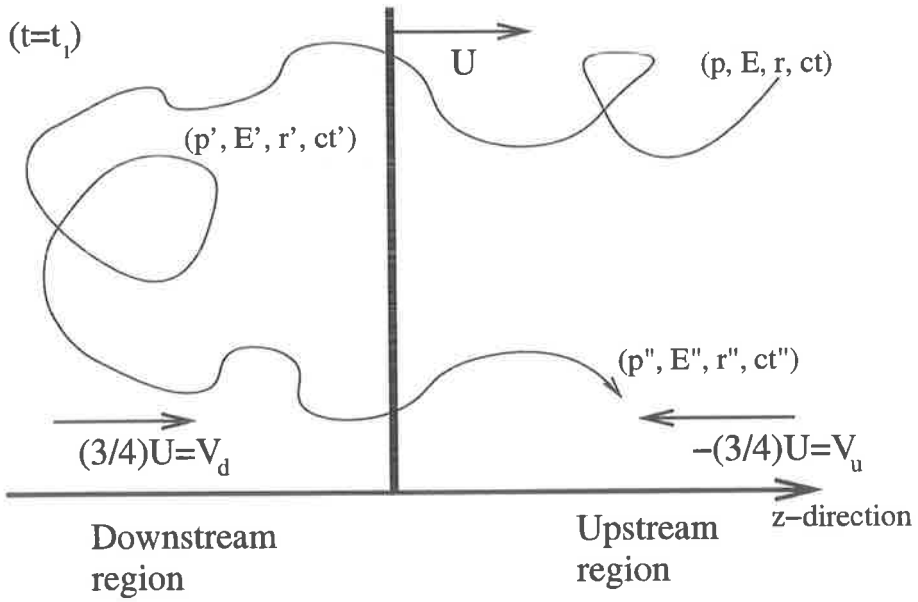

Figure 5.7: The schematic diagram of a relativistic particle's trajectory at $t = t_1$. When the relativistic particle enters the downstream region from upstream region, a Lorentz transformation to downstream frame is applied to the particle $[(\vec{p}, E, \vec{r}, ct) \rightarrow (\vec{p}', E', \vec{r}', ct')]$. When it returns to upstream region, a Lorenz transformation to upstream frame is applied to the particle $[(\vec{p}', E', \vec{r}', ct') \rightarrow (\vec{p}'', E'', \vec{r}'', ct'')]$

A relativistic proton is injected at the origin as the shock front passes $z = 0$ with velocity $U = (0.03 \times c)$. Figure 5.7 shows the schematic diagram of a relativistic particle's trajectory after $t = t_0$. Once the relativistic particle crosses the shock front into the downstream region, a Lorentz transformation to the downstream frame will be applied to the particle $[(\vec{p}, E, \vec{r}, ct) \rightarrow (\vec{p}', E', \vec{r}', ct')]$. If the particle returns from the downstream to the upstream region, a Lorenz transformation of the upstream frame will be applied to the particle $[(\vec{p}', E', \vec{r}', ct') \rightarrow (\vec{p}'', E'', \vec{r}'', ct'')]$. This was repeated until the particle was considered to have escaped downstream.

Table 5.1 (a) shows the Lorentz transformation when the particle enter the downstream region. In Table 5.1 (a), γ_d is the Lorentz factor in downstream frame and is $(1 - \beta_d^2)^{-1/2}$, where $\beta_d = \frac{V_d}{c}$. V_d represents the velocity of downstream plasma with respect to the upstream plasma, and is $\frac{3}{4}U$ (U: shock front velocity). Table 5.1 (b) shows the Lorentz transformation when the particle returns to the upstream region. V_u represents the velocity

(a)	Upstream	$\Longrightarrow$	Downstream	(b)	Downstream	$\Longrightarrow$	Upstream
	$(\vec{p}, E, \vec{r}, ct)$	$\Longrightarrow$	$(\vec{p}', E', \vec{r}', ct')$		$(\vec{p}', E', \vec{r}', ct')$	$\Longrightarrow$	$(\vec{p}'', E'', \vec{r}'', ct'')$
	p_z	$\Longrightarrow$	$p'_z = \gamma_d\left(p_z - \frac{\beta_d E}{c}\right)$		p'_z	$\Longrightarrow$	$p''_z = \gamma_u\left(p'_z + \frac{\beta_u E'}{c}\right)$
	E	$\Longrightarrow$	$E' = \gamma_d(E - \beta_d c p_z)$		E'	$\Longrightarrow$	$E'' = \gamma_u(E' + \beta_u c p'_z)$
	z	$\Longrightarrow$	$z' = \gamma_d(z - \beta_d ct)$		z'	$\Longrightarrow$	$z'' = \gamma_u(z' + \beta_u ct')$
	ct	$\Longrightarrow$	$ct' = \gamma_d(ct - \beta_d z)$		ct'	$\Longrightarrow$	$ct'' = \gamma_u(ct' + \beta_u z')$

Table 5.1: Lorentz transformation. (a) From upstream to downstream frame. $\gamma_d = (1-\beta_d^2)^{-1/2}$ and $\beta_d = \frac{V_d}{c}$, where $V_d = \frac{3}{4}U$. Subscript "d" represents downstream frame. (b) From downstream to upstream frame. $\gamma_u = (1-\beta_u^2)^{-1/2}$ and $\beta_u = \frac{V_u}{c}$, where $V_u = \frac{3}{4}U$. Subscript "u" represents upstream frame.

of upstream plasma with respect to the downstream plasma, which is also $\frac{3}{4}U$.

The energy gain by particle acceleration at shock, depends on how many times the particle crosses the shock front, according to the study by Bell [3]. In other words, if the particle proceeds far away from the shock front and remains in the same region, it will not gain any more energy. For the computer simulation it is necessary to stop the simulation when a proton is never likely to return to the shock, and so it is necessary to set a maximum distance downstream from the shock front before the simulation for that proton is stopped. The simulation then considers the trajectory of the next particle. The following is the idea of how to settle this maximum distance from the shock front. Firstly, the convection distance d_{conv} is defined as the distance between the shock front and the particle if the particle is stationary with respect to the downstream plasma,

$$d_{conv} = \frac{1}{4}Ut. \tag{5.2.5}$$

The diffusion transport root mean square distance represents how far the particle will

diffuse according to quasi-linear theory and is defined as

$$d_{diff} = \sqrt{2K_\alpha t}, \tag{5.2.6}$$

where K_α is diffusion coefficient and $\alpha = \parallel$ for the parallel diffusion coefficient and $\alpha = \perp$ for the perpendicular diffusion tensor. The values of K_α were calculated from Honda's fitting function [11]. The diffusion tensor components for $\frac{R_g}{L_0} < 1$ are

$$\frac{K_\parallel}{cL_0} = (0.981)(f^H_{turb})^{-1.465}\left(\frac{R_g}{L_0}\right)^{0.332} \tag{5.2.7}$$

$$\frac{K_\perp}{cL_0} = (0.0765)(f^H_{turb})^{1.505}\left(\frac{R_g}{L_0}\right)^{0.470}, \tag{5.2.8}$$

where R_g is proton's gyroradius and L_0 is the turbulence scale. The diffusion tensor components for $\frac{R_g}{L_0} > 1$ are

$$\frac{K_\parallel}{cL_0} = (0.981)(f^H_{turb})^{-1.465}\left(\frac{R_g}{L_0}\right)^{1.907} \tag{5.2.9}$$

$$\frac{K_\perp}{cL_0} = (0.0765)(f^H_{turb})^{1.505}\left(\frac{R_g}{L_0}\right)^{0.088}. \tag{5.2.10}$$

From Equations 5.2.5 and 5.2.6, the maximum distance will be calculated,

$$d_{max} = \eta\frac{K_\alpha}{U}. \tag{5.2.11}$$

In Equation 5.2.11, η is the constant and in the simulation η was chosen between $2 \leq \eta \leq 3$. If the relativistic proton is farther than the maximum distance downstream, d_{max}, the particle is regarded as trapped in the downstream region, and then the simulation is terminated.

5.2.3 Propagation of relativistic protons near parallel shocks

The propagation of protons in a parallel shock environment was investigated. In a parallel shock, the shock normal is parallel to the direction of the mean magnetic field $\vec{B}_0$. In the simulation, the z-direction is the direction of the mean magnetic field vector.

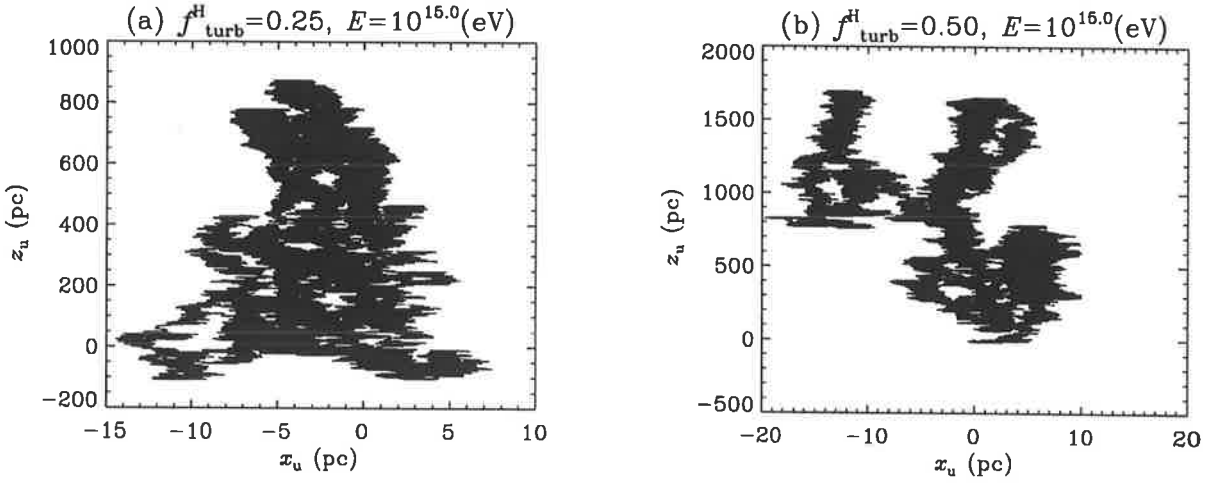

Figure 5.8: Trajectories of 10^{15}eV protons in the parallel shock. (a) Trajectory in $f^H_{turb} = 0.25$ magnetic field. (b) Trajectory in $f^H_{turb} = 0.5$ magnetic field. The mean magnetic field and the shock front is in z-direction.

Figures 5.8 and 5.9 show examples of proton trajectories near a parallel shock. x_u and z_u in Figures 5.8 and 5.9 indicate x- and z-components of proton's upstream-frame position. The initial energy of the proton is 10^{15}eV. Figure 5.8 (a) and (b) show the trajectories of the protons in $f^H_{turb} = 0.25$ magnetic field and $f^H_{turb} = 0.5$ magnetic field respectively. Figure 5.9 (a) and (b) show trajectories of protons in a $f^H_{turb} = 1.0$ magnetic field and a $f^H_{turb} = 2.0$ magnetic field respectively. f^H_{turb} is the turbulence level parameter and is defined in Equation 5.2.4. If the turbulence level f^H_{turb} is smaller than 1.0, the mean magnetic field dominates the total magnetic field. If f^H_{turb} is larger than 1.0, the irregular magnetic field dominates the total magnetic field and the magnetic field become more isotropic. The simulation for low f^H_{turb} took longer time for a proton to reach the maximum distance d_{max} in downstream because d_{max} for low f^H_{turb} is larger than that for high f^H_{turb} according to Equation 5.2.7. The protons in Figure 5.8 tend to diffuse more in the z-direction than the protons in Figure 5.9 due to the low f^H_{turb}.

Figures 5.10 (a) shows an example of the z-component of a 10^{15}eV proton's upstream-

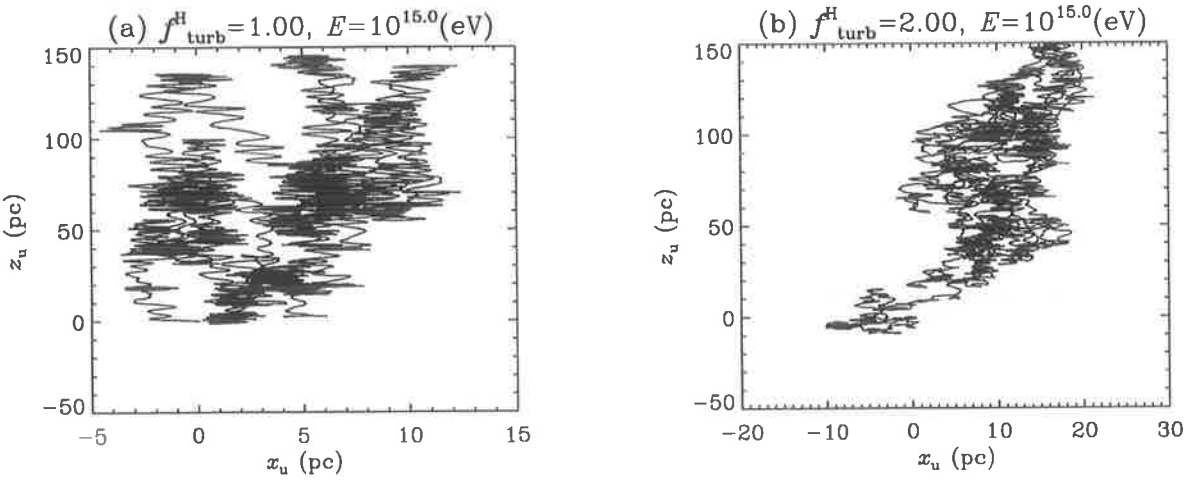

Figure 5.9: Trajectories of 10^{15}eV protons in the parallel shock. (a) Trajectory in $f^H_{turb} = 1.0$ magnetic field. (b) Trajectory in $f^H_{turb} = 2.0$ magnetic field. The mean magnetic field and shock front is in z-direction.

frame position vs. upstream-frame time ct_u in a $f^H_{turb} = 0.25$ magnetic field. The solid line in Figure 5.10 (a) indicates the position of shock front, and the dotted line indicates the distance of protons from the shock front at which they are considered to have escaped downstream. If a proton reaches the maximum distance, the simulation will stop. Figures 5.10 (b) shows the proton's energy vs. upstream-frame time ct_u. The energy of proton in Figure 5.10 goes up every acceleration cycle. Figure 5.10 (b) shows that the upstream energy is constant while the proton propagates in the upstream region, whereas the upstream energy oscillates gyro-motion while the proton propagates in the downstream region. Figures 5.11 (a) shows an example of the z-component of the 10^{15}eV proton's position with time ct_u in $f^H_{turb} = 2.0$ magnetic field. Figures 5.11 (a) shows the proton's energy vs. time ct_u.

Figures 5.12 shows that the distribution of $N_{\rm return}$. $N_{\rm return}$ is the number of times a proton returns to the upstream region before escaping the downstream. Figures 5.12 (a) is the case of 10^{15}eV protons in $f^H_{turb} = 0.25$ magnetic fields and Figures 5.12 (b) is the case

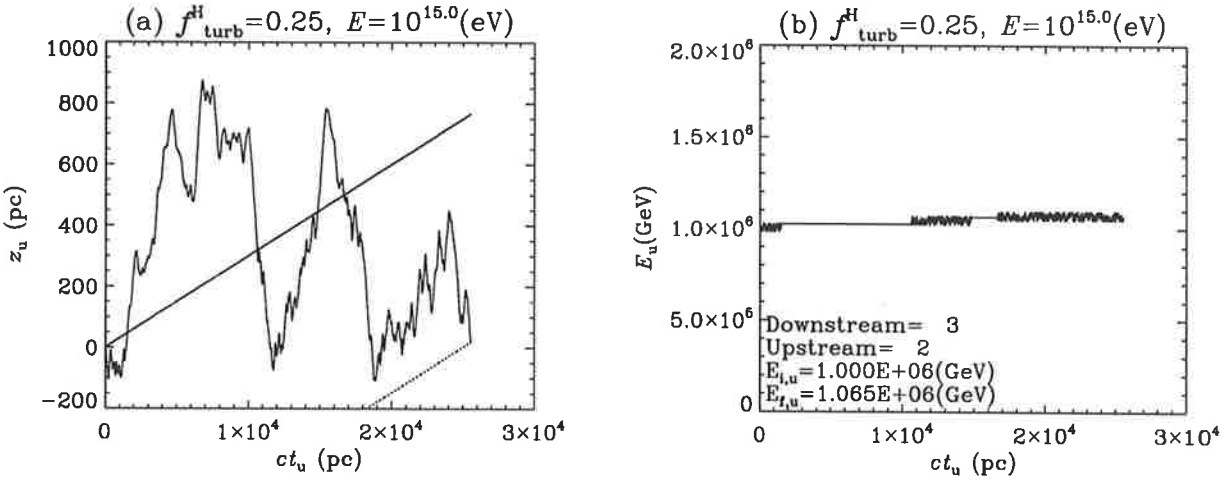

Figure 5.10: (a) z-component of proton's position as a function of time ct_u in shock environment. Solid line indicates the position of shock front and dotted line indicates the maximum distance from the shock front. Initial energy of proton is 10^{15}eV= 10^{6}GeV and the turbulence level is f^{H}_{turb} = 0.25. (b) Transition of proton's energy in the shock environment.

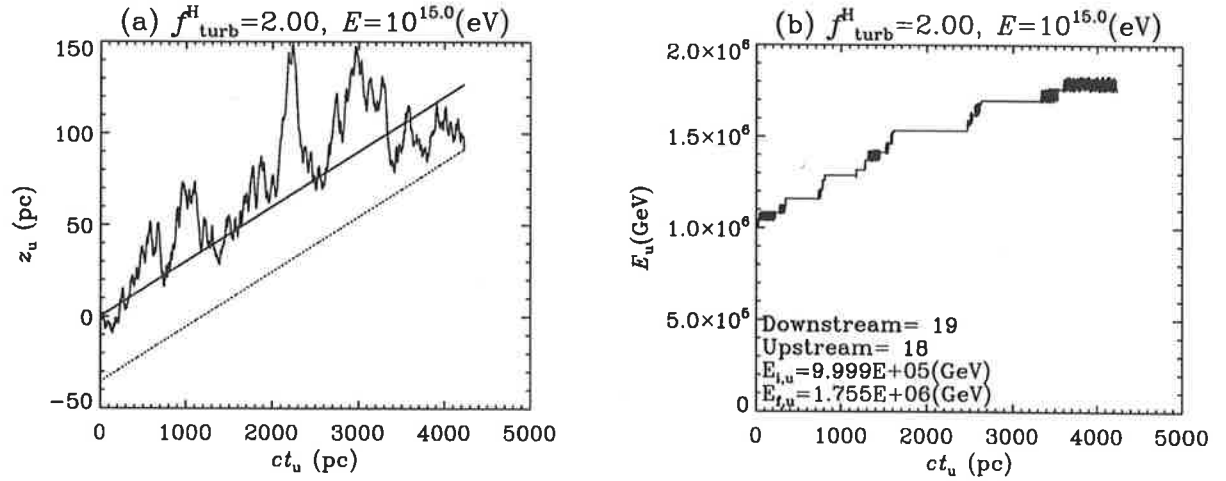

Figure 5.11: (a) z-component of proton's position as a function of time ct_u in shock environment. Solid line indicates the position of shock front and dotted line indicates the maximum distance from the shock front. Initial energy of proton is 10^{15}eV= 10^{6}GeV and the turbulence level is f^{H}_{turb} = 2.0. (b) Transition of proton's energy in the shock environment.

of 10^{15}eV protons in $f^H_{turb} = 0.5$ magnetic field. The number of sample trajectories is 100. The dashed lines in Figure 5.12 indicate the mean value of $N_{\rm return}$. The solid curves in Figures 5.12 and 5.13 indicate the n-th probabilities of returning to the shock $(P_{\rm return})^n$ for various values of $P_{\rm return}$ from the range $0.9 < P_{\rm return} < 1.0$. The $P_{\rm return}$ could be estimated as follows. The probability of returning more than n times is

$$P^{\geq n}_{\rm return} = (P_{\rm return})^n \tag{5.2.12}$$

Using Equation 5.2.12, the probability of returning n times is

$$\begin{aligned} P^{n}_{\rm return} &= P^{\geq n}_{\rm return} - P^{\geq n+1}_{\rm return} \\ &= (P_{\rm return})^n - (P_{\rm return})^{n+1} \end{aligned} \tag{5.2.13}$$

$P_{\rm escape} \approx U/c = 0.03$, and so the probability of returning at least once is

$$P_{\rm return} = 1 - P_{\rm escape} = 0.97 \tag{5.2.14}$$

Therefore Equation 5.2.13 becomes

$$P^{n}_{\rm return} = (0.97)^n - (0.97)^{n+1} \tag{5.2.15}$$

Figures 5.13 shows that the distribution of $N_{\rm return}$. Figures 5.13 (a) is the case of 10^{15}eV protons in $f^H_{turb} = 1.0$ magnetic field and Figures 5.13 (b) is the case of 10^{15}eV protons in $f^H_{turb} = 2.0$ magnetic field. When the protons propagate in high f^H_{turb} magnetic field ($f^H_{turb} \geq 1.0$), the distribution of $N_{\rm return}$ tends to spread and the chance of never returning to the shock becomes small. Especially in $f^H_{turb} = 2.0$ case as shown in Figure 5.13 (b), the distribution is more extensive and the mean value and its uncertainty is 16.31 ± 1.60. This may also be due to the isotropic pattern of the turbulent magnetic field and therefore the proton propagation will not be confined in z-direction.

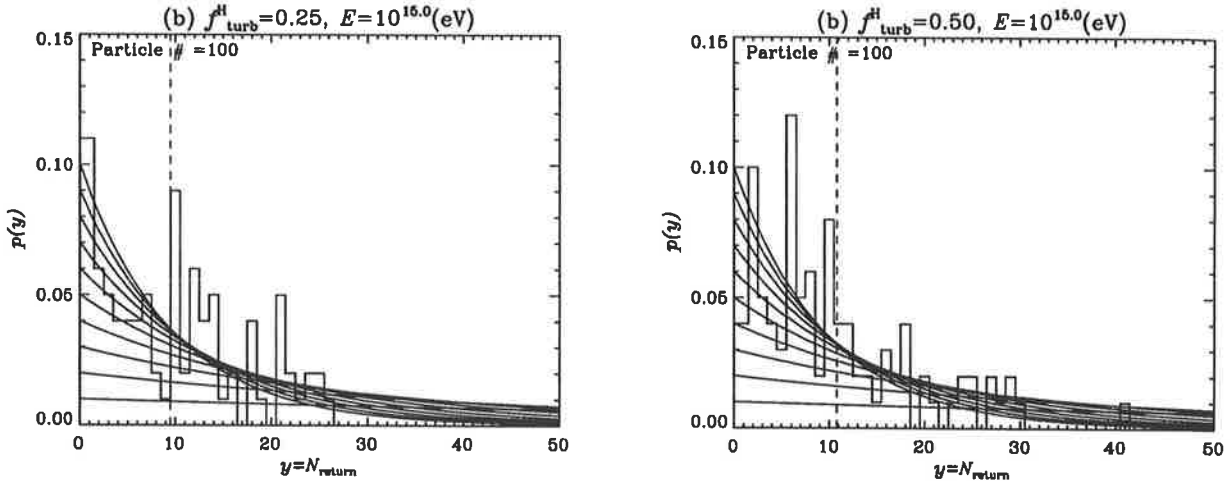

Figure 5.12: Distribution of the number of 10^{15}eV protons' returning to the upstream region, $N_{\rm return}$. (a) In $f^H_{turb} = 0.25$ magnetic field. (b) In $f^H_{turb} = 0.5$ magnetic field. The dashed lines indicate the mean of $N_{\rm return}$ and the solid curves indicate Equation 5.2.13 for $P_{\rm esc} = 0.01, 0.02 \ldots 0.10$, i.e. $P_{\rm return} = 0.99, 0.98 \ldots 0.90$.

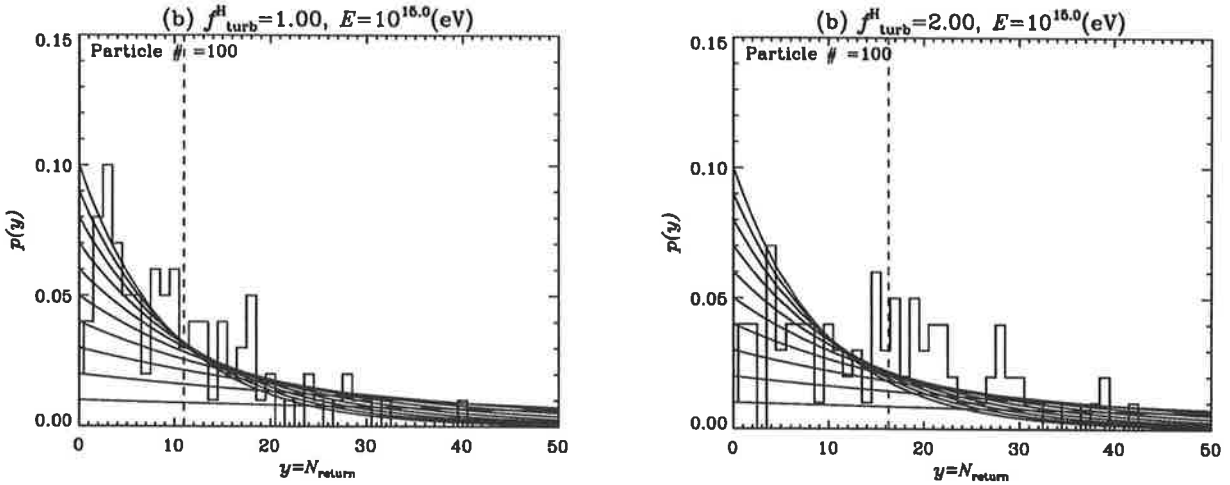

Figure 5.13: Distribution of the number of 10^{15}eV protons returning to the upstream region, $N_{\rm return}$. (a) In $f^H_{turb} = 1.0$ magnetic field. (b) In $f^H_{turb} = 2.0$ magnetic field. The dashed lines indicate the mean on $N_{\rm return}$ and the solid curves indicate Equation 5.2.13 for $P_{\rm esc} = 0.01, 0.02 \ldots 0.10$, i.e. $P_{\rm return} = 0.99, 0.98 \ldots 0.90$.

Table 5.2 shows average energy change $\frac{\langle \delta E \rangle}{E_i}$ and escape probability P_{escape} for protons with initial energies 10^{14}eV, 10^{15}eV and 10^{16}eV in various turbulence level magnetic field. The number of proton trajectory samples is 100. According to First Order Fermi Acceleration Theory, discussed in Section 5.1.4, given the average energy increase for return trip,

$$\frac{\langle \delta E \rangle}{E_i} = \frac{U}{c}, \tag{5.2.16}$$

where δE is energy change for return trip and E_i is an initial energy of protons. In the simulation the shock front velocity U was assumed to be $0.03 \times c$, therefore Equation 5.2.16 becomes

$$\frac{\langle \delta E \rangle}{E_i} = 0.03. \tag{5.2.17}$$

Average energy changes $\frac{\langle \delta E \rangle}{E_i}$ for various initial energy are relatively similar to the expected value in Equation 5.2.17.

Escape probability was discussed in Section 5.1.5 and is $P_{\text{escape}} \approx \frac{U}{c} = 0.03$. In Table 5.2, values of the escape probability P_{escape} were estimated from the solid curves (P_{escape} fitting lines) in Figures 5.12 and 5.13. Uncertainties of P_{escape} in the Monte Carlo simulation were calculated from the simulation data. Uncertainties are very high because of small number of proton trajectory samples which is 100. P_{escape} for various f_{turb}^{H} in $E = 10^{14}$eV protons are close to 0.03. On the other hand, P_{escape} in higher energy tend to increase. This suggests that higher energy protons have a tendency to escape from the shock front after entering the downstream region.

5.3 Summary and conclusion

Shock acceleration was investigated by applying the cosmic ray diffusion simulation method proposed by Giacalone and Jokipii [7] [8] [9].

	10^{14}eV		10^{15}eV		10^{16}eV	
	$\frac{\langle \delta E \rangle}{E_i}$	P_{escape}	$\frac{\langle \delta E \rangle}{E_i}$	P_{escape}	$\frac{\langle \delta E \rangle}{E_i}$	P_{escape}
$f^H_{turb} = 0.25$	0.024	0.03±0.03	0.012	0.10±0.01	0.009	0.05±0.02
$f^H_{turb} = 0.5$	0.026	0.03±0.04	0.016	0.09±0.01	0.011	0.08±0.02
$f^H_{turb} = 1.0$	0.026	0.04±0.06	0.016	0.08±0.01	0.014	0.12±0.02
$f^H_{turb} = 2.0$	0.026	0.05±0.07	0.019	0.04±0.02	0.015	0.07±0.02

Table 5.2: Average energy change $\frac{\langle \delta E \rangle}{E_i}$ and escape probability P_{escape} for protons with initial energies 10^{14}eV, 10^{15}eV and 10^{16}eV. The number of sample trajectories is 100.

Section 5.1 I explained the development of shock acceleration theory. Second Order Fermi [6] Acceleration was proposed in 1949 and it concluded that the average energy increase was the order of $\left(\frac{U}{c}\right)^2$, where U is the cloud velocity. A more efficient cosmic ray diffusive shock acceleration theory was developed in the late 1970's, and Bell [3] showed that the average energy increase was proportional to $\frac{U}{c}$. In this First Order Fermi Acceleration, the differential form of cosmic ray spectrum is $N(E)dE \propto E^{-2}dE$ on acceleration.

In Section 5.2 I described on acceleration methods for the shock acceleration simulation. In this study, the simulation of Giacalone and Jokipii was applied to simulating the shock acceleration. The study investigated the Parallel Shock Case, in which the direction of the mean magnetic field is parallel to the shock front direction, which in the present simulation was the z-direction. To investigate the parallel shock acceleration of protons, four routines were included in the shock simulation:

1. Shock front moves toward z-direction with the speed $U = 0.03 \times c$.

2. Compressed magnetic field was created in downstream region. The magnetic field was compressed by factor of 4 in z-direction.

3. Lorentz transformation between downstream and upstream frame.

4. The maximum distance of protons downstream position from the shock front was set, so that the simulation stops before a proton is stuck in the downstream region.

The shock simulation was implemented for various proton energies and various turbulence level f_{turb}^{H}.

In conclusion, the values of $\frac{\langle \delta E \rangle}{E_i}$ and P_{escape} are close to the expected values from the First Order Fermi Acceleration.

Chapter 6

Summary and further work

6.1 Cosmic ray diffusion simulation

In this research, the diffusion of high energy cosmic rays (protons) in turbulent magnetic fields was investigated by using a Monte Carlo technique. Propagation of cosmic rays in turbulent magnetic fields can be described by three-dimensional diffusion Equations 1.4.1 and 1.4.3. Cosmic ray diffusion in turbulent magnetic fields was discussed in Section 1.4.

In the research I selected two cosmic ray diffusion simulation techniques which used Monte Carlo methods to investigate the propagation of cosmic rays in turbulent magnetic fields. The two simulations were:

1. The simulation method proposed by Honda [11]

2. The simulation method proposed by Giacalone and Jokipii [7] [8] [9]

In the two simulations, the magnetic field was assumed to be static, and the total magnetic field was divided into two components: the regular part $\vec{B}_0$ and the irregular part $\delta\vec{B}$,

namely,

$$\begin{aligned}\vec{B}_{total}(\vec{r}) &= \vec{B}_0 + \delta\vec{B}(\vec{r}) \\ &= B_0\hat{e}_z + \delta\vec{B}(\vec{r}).\end{aligned} \tag{6.1.1}$$

The regular part of the total magnetic field in Equation 6.1.1 is directed toward the z-direction, and the irregular part was a Kolmogorov-like turbulent magnetic field in both simulations. A Kolmogorov-like magnetic field is typical of the turbulent magnetic field which exist in the interstellar medium. The power spectrum of the Kolmogorov-type magnetic field follows a power law $|\vec{B}^2(\vec{k})| \propto k^{\alpha}$, where $\alpha = -5/3$. The detailed discussion of the Kolmogorov magnetic field was given in Section 1.3. The method used to generate a Kolmogorov-like magnetic field differs between Honda's simulation and the Giacalone and Jokipii simulation.

In the cosmic ray diffusion simulations, relativistic charged cosmic rays (protons) were injected into the turbulent magnetic field $\vec{B}_{total}$ and the positions of the protons were calculated at time t. In the simulations a number of cosmic rays were injected into the Kolmogorov turbulent magnetic fields, and the average squared distances, namely $\langle z^2 \rangle$ and $\langle x^2 + y^2 \rangle$, for each time t were calculated. Then the diffusion tensor components were calculated from Equation 6.1.2,

$$\langle z^2 \rangle = 2K_{\parallel}t, \qquad \langle x^2 + y^2 \rangle = 4K_{\perp}t, \tag{6.1.2}$$

where $K_{\parallel}$ represents diffusion tensor components parallel to the regular magnetic field B_0, which is in z-direction and $K_{\perp}$ represents the components perpendicular to the regular magnetic field.

In this study, Honda's simulation, and the simulation studied by Giacalone and Jokipii, were repeated, and the results were investigated and compared with the original results. Then one of these two simulation method was selected to investigate the propagation of

high energy protons in the shock environment and the proton acceleration by the shock.

6.2 Honda's simulation

In the present research I first investigated the cosmic ray diffusion simulation method that Honda had proposed. Honda used a three-dimensional lattice and placed random vector potentials at each lattice point [11]. The vector potentials were sampled from the Monte Carlo simulation and following an exponential distribution. Then he created irregular magnetic fields by using Equation 6.2.1

$$\delta\vec{B} = \nabla \times \delta\vec{A}. \tag{6.2.1}$$

The curl of vector potential ensures $\vec{\nabla} \cdot \delta\vec{B} = 0$.

I decided to compare Honda's method with a simpler method in which the magnetic field on grid points is sampled directly. Also, I decided to investigate whether or not it is necessary to interpolate the magnetic field for positions between the grid points. Thus there were four cases considered:

1. $\vec{A}$ at grid points sampled, $\vec{B} = \vec{\nabla} \times \vec{A}$, $\vec{B}$ interpolated.

2. $\vec{B}$ at grid points sampled, $\vec{B}$ interpolated.

3. $\vec{A}$ at grid points sampled, $\vec{B} = \vec{\nabla} \times \vec{A}$, no interpolation.

4. $\vec{B}$ at grid points sampled, no interpolation.

While, the no-interpolation cases saved considerable computing time, the results were not consistent with the cases where interpolation was done. In particular, the parallel and perpendicular diffusion coefficients were calculated from the simulation results in each case and compared to the low and high energy limits which can be obtained theoretically

from random walk theory. This comparison was made in Table 3.4 of Chapter 3. It was found that only CASE 1 was consistent with the theoretical result, and hence I adopted Honda's method with interpolation of $\vec{B}$ between grid points.

Secondly, the proton diffusion in the Kolmogorov-like magnetic field was investigated. The same calculations and analyses of the proton diffusion were carried out in Kolmogorov-type magnetic field environment. In the Kolmogorov-type magnetic field a lattice space with a different length of grid spacing was used. The magnetic fields placed on each grid point have an r.m.s. value dependent upon the grid spacing. Then the magnetic fields at the grid points were vectorially added to create the irregular part of the magnetic field. The energy-dependent diffusion tensors of high energy protons in Kolmogorov magnetic fields were discussed in Section 3.3.3. In Section 3.3.3, the results using Honda's method were compared to Honda's original results.

In Figure 4.6 the plots of $\frac{K_{\parallel}}{cL_{max}}$ do not agree to Honda's results in $\log_{10}[\frac{R_g}{L_{max}}] < 0$ region and the plots of $\frac{K_{\perp}}{cL_{max}}$ do not agree to Honda's results $\log_{10}[\frac{R_g}{L_{max}}] > 0$ region. These differences can be explained by four reasons:

1. The simulation used a normal distribution to sample vector potentials $\delta\vec{A}$, whereas an exponential distribution was used in the Honda's original simulation .

2. The simulation used the periodic boundary condition which was not mentioned in Honda's study.

3. The simulation used $\alpha = \frac{2}{3}$, whereas Honda used $\alpha = \frac{5}{3}$ for $[L_i]^{\alpha}$.

4. The number of time steps might not have been large enough to calculate diffusion tensors.

6.3 Giacalone and Jokipii simulation

The next simulation to be repeated and investigated was developed by Giacalone and Jokipii. Giacalone and Jokipii used the superposition of plane waves to create the Kolmogorov-like magnetic fields for the irregular part of the magnetic field [7] [8] [9]. They proposed that the irregular part $\delta\vec{B}(x,y,z)$ be a superposition of plane waves with isotropic propagation directions and with random polarisations and phases.

The trajectories of the charged particles were calculated from the equation of motion. Giacalone and Jokipii created new magnetic fields at each time step as a particle changed its position, whereas Honda set magnetic fields at each lattice point initially. So a magnetic field interpolation is not necessary in Giacalone and Jokipii simulation. The diffusion tensors were calculated by using Equation 6.1.2 and the results were compared to Honda's result, and the result from the Casse et al. simulation. The diffusion tensors for high energy protons ($\log\left(\frac{r_g}{L_0}\right) \gg 1$) were consistent with the results from Honda and Casse et al. However the diffusion tensors with low energy protons ($\log\left(\frac{r_g}{L_0}\right) \ll 1$) were inconsistent with the Honda and Casse et al. results.

For the above reason, distributions of the proton's final position were investigated. The distribution of the final position was expected to be a Gaussian distribution, but the low energy protons ($E = 10^{13}$eV) showed a high peak at the origin. This implied that the 10^{13}eV protons were strongly influenced by the magnetic field and were likely to be trapped by the magnetic field.

The peak shape in the distribution of the position of the low energy protons might depend upon the pitch angle of the protons. The simulation selected the final positions of the protons with larger initial pitch angles and the their distribution was analysed. The protons with larger initial pitch angles showed a much higher peak than those with smaller

initial pitch angle. The 10^{13}eV protons with large initial pitch angles were likely to stay in the vicinity of the origin, and they seemed to be trapped by the magnetic field, whereas the 10^{13}eV protons with small initial pitch angles had more opportunity to travel further from the origin.

In comparing the Honda simulation with the Giacalone and Jokipii simulation, the latter does not need magnetic field interpolation. Moreover a periodic boundary conditions was applied in Honda's simulation method, and so the turbulent magnetic field repeated every 1.0 pc. The sensitivity to the minimum grid spacing L_{min} and size of time step can also cause Honda's result to differ from the results of the Giacalone and Jokipii simulation. For these reasons, the modified Giacalone and Jokipii simulation was used to investigate the shock acceleration phenomenon.

6.4 Shock acceleration

The study used the simulation method proposed by Giacalone and Jokipii [7] [8] [9] for the application of shock acceleration at a shock parallel to the mean magnetic field $\vec{B}_0$ (Parallel Shock).

The shock simulation was implemented for various proton energies and various turbulence level f^H_{turb}. Values of $\frac{\langle \delta E \rangle}{E_i}$ and P_{escape} were found to be close to the expected values of the $\frac{\langle \delta E \rangle}{E_i}$ and P_{escape}.

6.5 Further work

There is further work to extend the study of cosmic ray shock acceleration.

In the study, the cosmic ray acceleration in the Parallel Shock was investigated. The

same study could be done on Perpendicular Shock. In a Perpendicular Shock, the direction of the shock front is perpendicular to the mean magnetic field vector of the turbulent magnetic field. Figure 6.1 shows a schematic diagram of a Perpendicular Shock. The direction of the mean magnetic field can be either the x- or y-direction.

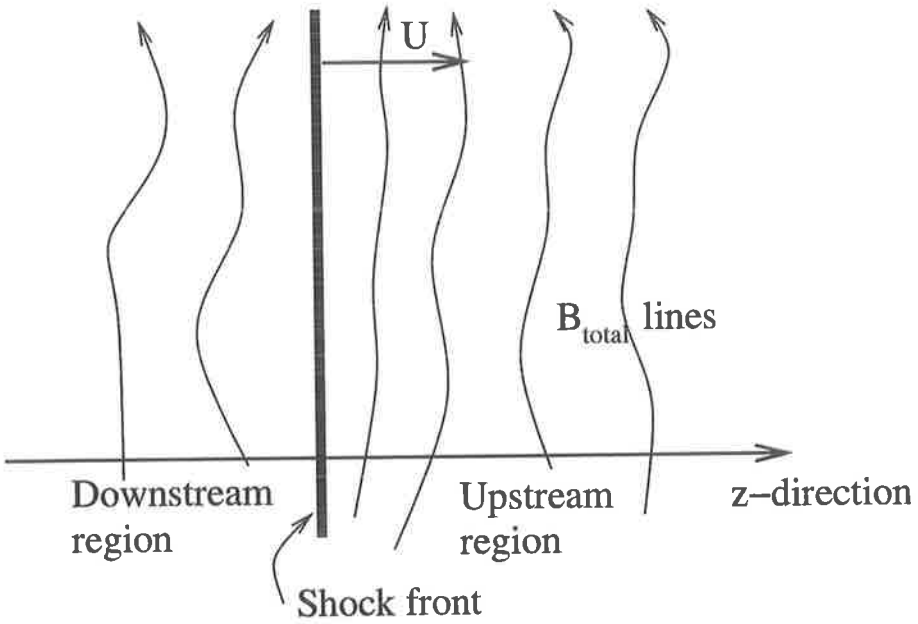

Figure 6.1: The schematic diagram of the Perpendicular Shock. The direction of the shock front is perpendicular to the mean magnetic field.

In a Perpendicular Shock simulation, Lorentz transformation of the electromagnetic field should be considered. Figure 6.2 shows the schematic diagram of two different frames of references. In Figure 6.2, frame K is stationary and frame K' is moving with velocity v in z-direction. When a relativistic particle moves from one frame of reference to other frame, the Lorentz transformations should be applied to the position-time four-vector and the four-momentum of relativistic protons. In the shock simulation, a subroutine to calculate the Lorentz transformation of four-vector and four-momentum was included. Lorentz transformation of a perpendicular magnetic field, an electric field appears in the new frame. Equations 6.5.1 and 6.5.2 give the Lorentz transformations of the electromagnetic field from frame K to frame K', the frame K remaining stationary and frame K' moving

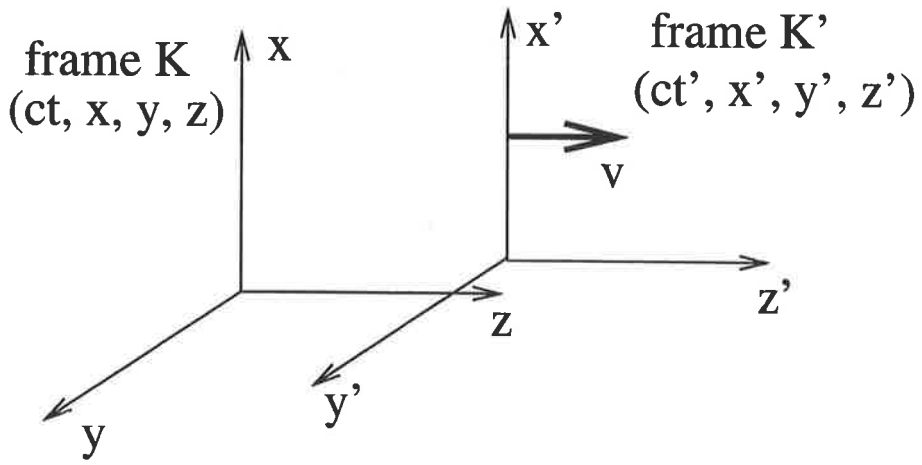

Figure 6.2: The schematic diagram of two frames of reference. The frame K is fixed frame and the frame K' is moving toward z-direction.

toward z-direction with speed v.

$$\begin{cases} E'_x(ct',\ \vec{r}') = \gamma[E_x(ct,\ \vec{r}) - \vec{v}B_y(ct,\ \vec{r})] \\ E'_y(ct',\ \vec{r}') = \gamma[E_y(ct,\ \vec{r}) + \vec{v}B_x(ct,\ \vec{r})] \\ E'_z(ct',\ \vec{r}') = E_z(ct,\ \vec{r}) \end{cases} \tag{6.5.1}$$

$$\begin{cases} B'_x(ct',\ \vec{r}') = \gamma[B_x(ct,\ \vec{r}) + \frac{\beta}{c}E_y(ct,\ \vec{r})] \\ B'_y(ct',\ \vec{r}') = \gamma[B_y(ct,\ \vec{r}) - \frac{\beta}{c}E_x(ct,\ \vec{r})] \\ B'_z(ct',\ \vec{r}') = B_z(ct,\ \vec{r}) \end{cases} \tag{6.5.2}$$

Performing a Perpendicular Shock simulation, and comparing with a Parallel Shock acceleration, will give us more useful information about shock acceleration of protons, and including the Lorentz transformation of electromagnetic field will refine the shock simulation. These could be done to extend this study.

Bibliography

[1] Armstrong, J.W. and Rickett, B.J., 1981, Monthly Notice of The Royal Astronomical Society, 194, 623-638.

[2] Armstrong, J.W., Rickett, B.J. and Spangler, S.R., 1995, Astronomical Journal, 443: 209-221, 1995 April 10.

[3] Bell, A.R., 1978, Mon.Not.R.astro.Soc., 182, 147.

[4] Bhattacharjee, P. and Sigl, G., 2000, Physics Reports, 327,109-247.

[5] Casse, F., Lemoine, M. and Pelletier, G., astro-ph/0109223.

[6] Fermi, E., 1949, Phys.Rev., 75, 1169.

[7] Giacalone, J. and Jokipii, J.R., 1994, Astrophysical Journal, 430: L137-L14, 1994 August 1.

[8] Giacalone, J. and Jokipii, J.R., 1996, Journal of Geophysical Research, Vol.101, No.A5, Pages 11,095-11,105, 1996 May 1.

[9] Giacalone, J. and Jokipii, J.R., 1999, Astrophysical Journal, 520: 204-214, 1999 July 20.

[10] Goldstein, M.L., Roverts, D.A. and Matthaeus, W.H., 1995, Annual Review of Astronomy and Astrophysics, 33:283-325.

[11] Honda, M., 1987, Astrophysical Journal, 319: 836-841, 1987 August 15.

[12] Jokipii, J.R., 1967, Astrophysical Journal, 149: 405-415, 1967 August.

[13] Jokipii, J.R., 1973, Annual Review of Astronomy and Astrophysics, 11:1-28.

[14] Kirk, J.G. and Dendy, O., astro-ph/0101175.

[15] Kolmogorov, A.N., 1941, Dokl. Akad. Nauk SSSR, 30, 9-13.

[16] Kolmogorov, A.N., 1941, Dokl. Akad. Nauk SSSR, 32, 16-18.

[17] Kolmogorov, A.N., 1962, Journal of Fluid Mechanics, 13, 82.

[18] Lee, L.C. and Jokipii, J.R., 1976, Astrophysical Journal, 206: 735-743, 1976 June 15.

[19] Longair, M.S., 2000,"High Energy Astrophysics Vol. 2", Cambridge University Press.

[20] Parizot, E. and Drury, L.O'C., 1999, Astronomy and Astrophysics, 349, 673-684.

[21] Protheroe, R.J., 2003, "Diffusion and Shock Acceleration", Honors Astrophysics Lecture Note.

[22] Sari, J.W. and Ness, N.F., 1969, Solar Physics, 8, 155-165.

[23] Schlickeiser, R., Sievers, A. and Thiemann, H., 1987, Astronomy and Astrophysics, 182, 21-35.

[24] Stanev, T., Muecke, A., Protheroe,R.J. and Rachen, J.P., 2000, Physical Review D62, 093005(2000); e-print astro-ph/0003484.

[25] Vogt, C. and Ensslin, T.A., Astronomy and Astrophysics, 412: 373-385, 2003